ULTRASOUND-MODULATED OPTICAL TOMOGRAPHY IN SOFT BIOLOGICAL TISSUES

A Dissertation

by

SAVA SAKADŽIĆ

Submitted to the Office of Graduate Studies of
Texas A&M University
in partial fulfillment of the requirements for the degree of

DOCTOR OF PHILOSOPHY

May 2006

Major Subject: Biomedical Engineering

ULTRASOUND-MODULATED OPTICAL TOMOGRAPHY IN SOFT BIOLOGICAL TISSUES

A Dissertation

by

SAVA SAKADŽIĆ

Submitted to the Office of Graduate Studies of
Texas A&M University
in partial fulfillment of the requirements for the degree of

DOCTOR OF PHILOSOPHY

Approved by:

Chair of Committee,	Lihong V. Wang
Committee Members,	Gerard L. Coté
	Hsin-I Wu
	Edward S. Fry
Head of Department,	Gerard L. Coté

May 2006

Major Subject: Biomedical Engineering

ABSTRACT

Ultrasound-modulated Optical Tomography in Soft Biological Tissues. (May 2006)

Sava Sakadžić, B.S., University of Belgrade, Serbia and Montenegro;

M.S., University of Belgrade, Serbia and Montenegro

Chair of Advisory Committee: Dr. Lihong V. Wang

Optical imaging of soft biological tissues is highly desirable since it is nonionizing and provides sensitive contrast information which enables detection of physiological functions and abnormalities, including potentially early cancer detection. However, due to the diffusion of light, it is difficult to achieve simultaneously both good spatial resolution and good imaging depth with the pure optical imaging modalities.

This work focuses on the ultrasound-modulated optical tomography — a hybrid technique which combines advantages of ultrasonic resolution and optical contrast. In this technique, focused ultrasound and optical radiation of high temporal coherence are simultaneously applied to soft biological tissue, and the intensity of the ultrasound-modulated light is measured. This provides information about the optical properties of the tissue, spatially localized at the interaction region of the ultrasonic and electromagnetic waves.

In experimental part of this work we present a novel implementation of high-resolution ultrasound-modulated optical tomography that, based on optical contrast, can image several millimeters deep into soft biological tissues. A long-cavity confocal Fabry-Perot interferometer was used to detect the ultrasound-modulated coherent light that traversed the scattering biological tissue. Using 15-MHz ultrasound, we imaged with high contrast light absorbing structures placed 3 mm below the surface of chicken breast tissue. The resolution along the axial and the lateral directions

with respect to the ultrasound propagation direction was better than 70 and 120 μm, respectively. This technology is complementary to other imaging technologies, such as confocal microscopy and optical-coherence tomography, and has potential for broad biomedical applications.

In the theoretical part we present various methods to model interaction between the ultrasonic and electromagnetic waves in optically scattering media. We first extend the existing theoretical model based on the diffusing-wave spectroscopy approach to account for anisotropic optical scattering, Brownian motion, pulsed ultrasound, and strong correlations between the ultrasound-induced optical phase increments. Based on the Bethe-Salpeter equation, we further develop a more general correlation transfer equation, and subsequently a correlation diffusion equation, for ultrasound-modulated multiply scattered light. We expect these equations to be applicable to a wide spectrum of conditions in the ultrasound-modulated optical tomography of soft biological tissues.

DEDICATION

To my parents, Ljiljana and Toša, and to my wife Slavica, for their love

ACKNOWLEDGMENTS

I would like to express my sincere gratitude and appreciation to my major adviser, Dr. Lihong Wang, for his continuous guidance and support. I thank him for always being available for me, for providing an intellectually stimulating and friendly environment for research, and for all the time he spent on discussing and correcting the manuscripts with me. In every sense, none of this work would have been possible without him.

I thank my committee members, Dr. Gerard Coté, Dr. Hsin-I Wu, and Dr. Edward Fry for taking the time serving on my committee, and for always being supportive and making time for me. I would like to specifically acknowledge Dr. Vikram Kinra for generously providing the laboratory space and equipment for this project. A special thanks to Dr. George Stoica for medical expertise and good times at conferences.

I am grateful to my present and former colleagues in the laboratory, Dr. Konstantin Maslov, Dr. Geng Ku, Dr. Jun Li, Dr. Shuliang Jiao, Dr. Roger Zemp, Dr. Minghua Xu, and Dr. Yuan Xu for interest in my research, many scientific discussions, technical assistance, support and friendship. Appreciation is also extended to Sri-Rajasekhar Kothapalli, Xiao Xu, Chul-Hong Kim, Huiliang Zhang, Xueding Wang, Hao Zhang, and other members of the Optical Imaging Laboratory.

Many thanks to the faculty and staff of Biomedical and Industrial Engineering Departments, Dr. Jay Humphrey, Dr. Fidel Fernandez, Katherine Jakubik, Barry Jackson, and Dennis Allen for great teaching, and for administrative and technical help. I gratefully acknowledge Steve Smith for all the good time I had talking with him during the long hours in the machine-shop.

I thank my loving family in Belgrade for their love and support, and for teaching

me everything that I am today. They deserve far more credit than I can ever give them.

Finally, warmest thanks goes to my one true love — Slavica Djonović. Her presence in my life makes my every step meaningful, including this work.

TABLE OF CONTENTS

CHAPTER Page

LIST OF FIGURES

CHAPTER I
INTRODUCTION

Optical imaging of soft biological tissue is highly desirable since it is nonionizing, and it provides sensitive contrast information which enables potential early cancer detection.[1] Current techniques for cancer detection (ultrasound, x-ray computerized tomography, and magnetic resonance imaging) are not very efficient in detecting the lesions smaller than $\sim$ 1 cm. As a result, most of the cancers detected by these methods are in advanced stages, and development of new techniques for early cancer detection is an imperative.

The optical properties of soft biological tissues in the visible and near-infrared regions are related to the molecular structure, offering potential for the detection of tissue functions and abnormalities. Cancer-related tissue abnormalities, such as for example angiogenesis, hyper-metabolism, and invasion into adjacent normal tissue, posses optical signatures (both scattering and absorption), that offer the potential for early cancer detection. The optical scattering properties of tissue are strongly related to the tissue structure (cell nuclei size and density for example). On the other hand, optical absorption properties can reveal metabolic processes (hemoglobin concentration and oxygen saturation) and angiogenesis. However, due to the strong scattering of light in biological tissue, optical imaging at imaging depths greater than one optical transport mean free path ($\sim$ 1 mm in soft biological tissues at visible and near-infrared wavelengths) presents a challenge.

Ultrasound-modulated optical tomography (UOT)[2,3] is a hybrid technique, pro-

---

This thesis follows the style of *Journal of Biomedical Optics*.

posed to provide better resolution for the optical imaging of soft biological tissue by combining ultrasonic resolution and optical contrast. It combines the strengths of both methods – high contrast inherent in optical properties, and high ultrasound resolution. Because of the strong scattering, in order to have a good resolution pure optical imaging is limited to a small imaging depth. On the other hand, scattering of ultrasound waves in soft biological tissues is several orders of magnitude lower than scattering of light, which enables very good focusing of ultrasound and consequently excellent resolution in pure ultrasound imaging. However, ultrasound imaging provides weak contrast for early stage tumors because their mechanical properties are not very different from the normal tissue. In addition, pure ultrasound imaging cannot image oxygen saturation or concentration of hemoglobin.

In UOT, an ultrasonic wave is focused into biological tissue which is irradiated by the laser light of a high temporal coherence. Collective motions of the optical scatterers and periodic changes in the optical index of refraction are generated by ultrasound to produce fluctuations in the intensity of the speckles that are formed by the multiple-scattered light. The ultrasound-modulated component of light carries information about the optical properties of tissue from the region of interaction between the optical and ultrasonic waves. Any light that is modulated by the ultrasound, including both singly and multiply scattered partial waves, contributes to the imaging signal. Lateral resolution is typically obtained by focusing the ultrasonic wave. To obtain axial resolution different techniques are applied, including ultrasound frequency sweep, computer tomography, and tracking of ultrasound pulses or short bursts. Therefore, resolution in UOT is generally determined by ultrasound properties, and it is not limited by optical diffusion or multiple scattering of light. At the same time, contrast in UOT is based on optical tissue properties. Finally, the imaging resolution, as well as the maximum imaging depth, is scalable with the

ultrasonic frequency.

The first investigation of possibility to use UOT was done by Marks et al.[2] Subsequently, Wang et al.[3] developed UOT and obtained images in tissue phantoms using a single square-law detector. The ultrasound modulation of light in highly scattering medium was analyzed first by Leutz and Maret[4] both theoretically based on the diffusing-wave spectroscopy approach[5,6] and experimentally by using the plane-parallel Fabry-Perot interferometer. Kemple et al.[7] investigated the scale dependence of the ultrasound modulated optical signal on the optical thickness of the scattering medium, and discussed the imaging possibilities based on the signal-to-noise (SNR) analysis. Leveque et al.[8] developed a parallel speckle detection scheme that uses a CCD camera as a detector array, which was subsequently extended by Li et al.[9,10] with additional methods of analysis. It is found that by averaging the signal from all the CCD pixels, SNR can be greatly improved compared with the single square-law detector. In these experiments, one-dimensional (1D) and two-dimensional (2D) images of optically absorptive objects buried in a chicken breast tissue samples are obtained. In order to obtain resolution along the ultrasound axis, several different approaches are applied. Wang and Ku[11] developed a technique called frequency-swept UOT to achieve controllable spatial resolution along the ultrasonic axis, where axial positions are encoded by linearly swept ultrasound frequency. The technique is further combined by Yao et al.[12] with the parallel speckle detection scheme, and 2D images of biological tissue with buried objects were obtained. The reflection configuration for UOT is developed by Lev et al.,[13] and computed tomography is applied by Li and Wang[14] to reconstruct the image of the blood vessel buried in the chicken breast tissue sample. Recently, photorefractive crystals have been used in UOT experiment by Murray et al.[15] to detect the ultrasound-modulated optical intensity produced by ultrasound pulses traversing tissue phantoms.

The current optical technologies for *in vivo* high resolution imaging of biological tissue include primarily confocal microscopy and optical–coherence tomography (OCT). Confocal microscopy can achieve ~ 1 μm resolution but can image up to only 0.5 mm into biological tissue. OCT can achieve ~ 10 μm resolution but can image only ~ 1 mm into scattering biological tissue. Although both technologies are useful in their areas of strength, many superficial lesions of interest are deep beyond reach. Both of the technologies depend primarily on singly backscattered photons for spatial resolution. Because biological tissues, with exception of the ocular tissue, are highly scattering for light transport, singly backscattered light attenuates rapidly with imaging depth. Therefore, both of the technologies have fundamentally limited maximum imaging depths that restrict their applications.

Since UOT does not depend on singly backscattered light but rather on diffuse light, it overcomes the limitation of confocal microscopy and OCT on maximum imaging depth. The lateral resolution can be achieved by focusing the high frequency ultrasound. At the same time, axial resolution may be obtained by any of previously mentioned techniques, but it is preferred to use pulsed ultrasound due to the simplicity and compatibility with pure ultrasound imaging. Image resolution and maximum imaging depth in UOT is scalable with ultrasonic frequency. Functional imaging of oxygen saturation of hemoglobin may be achieved by using dual wavelengths. The proposed technology is complementary to confocal microscopy and OCT and has the potential for broad application in biomedicine.

In Chapter II, we present an novel apparatus for high-resolution UOT imaging of soft biological tissue. As stated before, efficient detection of the UOT signal presents a challenge. After diffusing through soft biological tissue, light forms a well developed speckle pattern on the surface of the detection system. The phases of individual speckles are randomly distributed and uncorrelated, and modulation depth is usually

very small ($\sim$ 1%, or less). Therefore, it is shown that SNR provided by the single square-law detectors is mostly not satisfactory, since they are limited by antenna theorem and detection of the diffused light in that case is not efficient. A CCD camera or a photorefractive crystal provide parallel speckle detection. Therefore, they are usually much better choice in terms of SNR. However, the speed of CCD detectors at present does not allow a real time tracking of ultrasound pulses. For our high-resolution UOT, we choose a long-cavity confocal FabryPerot interferometer (CFPI) to be the central part of the detection system. Our CFPI has a greater etendue – defined as the product of the acceptance solid angle and the area – than most CCD cameras and provides parallel speckle processing. In addition, a CFPI can detect the propagation of high-frequency ultrasound pulses in real time and tolerate speckle decorrelation. A CFPI is especially efficient at high ultrasound frequencies, where the background signal that is due to the unmodulated light can be filtered out effectively while the ultrasound-modulated component is transmitted. With our setup, using 15-MHz ultrasound, we imaged with high contrast light absorbing structures placed 3 mm below the surface of chicken breast tissue. The resolution along the axial and the lateral directions with respect to the ultrasound propagation direction was better than 70 μm and 120 μm, respectively.

In spite of a variety of different experimental configurations that have been invented to efficiently measure the ultrasonically modulated component of the light emerging from biological tissue, the exact nature of the ultrasound modulation of light in an optically scattering medium is still not well understood due to the complicated light-ultrasound interaction that occurs in the presence of optical scatterers. Approximate theories in the optical diffusion regime under a weak scattering approximation have been developed that include one or both of the main mechanisms of modulation. Mechanism 1 is the optical phase variations that are due to the ul-

trasonically induced movement of the optical scatterers,[4,7] whereas mechanism 2 is the optical phase variations that are due to ultrasonically induced changes in the optical index of refraction. Mechanism 1 was first modeled by Leutz and Maret[4] in a case of isotropic optical scattering, where an homogeneous infinite scattering medium is traversed by a plane ultrasound wave. It was also modeled by Kempe et al.,[7] and together with Brownian motion by Lev et al.[16] Mechanism 2 was first modeled by Mahan et al.,[17] and it was subsequently combined together with the mechanism 1 by Wang.[18] In all cases, a weak scattering approximation is assumed and a method of diffusing-wave spectroscopy[5,6] is applied. All authors considered isotropic optical scattering and the case when the ultrasound wavelength is smaller or comparable than the optical mean free path, which simplifies the treatment of distant correlations. It was shown by Wang[18] that mechanism 2 is more important than mechanism 1 for generation of modulated signals at high ultrasound frequencies. Due to the limited number of physical configurations where the probability density function of the optical path length is analytically known and since the theoretical model requires plane (infinite) ultrasound waves, only transmission[18] and reflection[16] geometries have been analytically studied so far, under assumption that the scattering medium (slab) is completely occupied with ultrasound. Wang[19] also developed a Monte Carlo algorithm which is more flexible and it could be modified to account for a wide spectrum of geometries.

In Chapter III, we present extension of the existing theoretical model[18] for ultrasound modulation of multiply scattered light to include scattering anisotropy. We develop the analytical expression for the temporal autocorrelation function of the electrical field component of multiply scattered coherent light transmitted through an anisotropically scattering media irradiated with a plane ultrasonic wave. The accuracy of the analytical solution is verified with an independent Monte Carlo sim-

ulation for different values of the ultrasonic and optical parameters. The analytical model shows that an approximate similarity relation exists; if the reduced scattering coefficient is unchanged regardless of the mean cosine of the scattering angle, the autocorrelation function remains approximately the same.

In Chapter IV, we further extend the existing model to account for the interaction of multiply scattered light with pulsed ultrasound, and to account for strong correlations between ultrasound induced optical phase increments. We present an analytical solution for the ultrasound-modulation of multiply scattered light in a medium irradiated with a train of ultrasound pulses. Previous theory is extended to cases where the ultrasound-induced optical phase increments between the different scattering events are strongly correlated, and it is shown that the approximate similarity relation still holds. The relation between the ultrasound induced motions of the background fluid and the optical scatterers is generalized, and it is shown that correlation exists between the optical phase increments that are due to the scatterer movement and the optical phase increments that are due to the modulation of the optical index of refraction. Finally, it is shown that compared with the spectrum of ultrasound pulses, the power spectral density of ultrasound-modulated light is strongly attenuated at the higher ultrasound frequencies.

In Chapter V, we develop a general temporal correlation transfer equation for ultrasound-modulated multiply scattered light. The equation can be used to obtain the mutual coherence function of light produced by a nonuniform ultrasound field in optically scattering media that have a heterogeneous distribution of optical parameters. We also develop a Monte Carlo algorithm that can provide the spatial distribution of the optical power spectrum in optically scattering media with focused ultrasound fields, and heterogeneous distributions of optically scattering and absorbing objects. Derivation of the correlation transfer equation is based on the

ladder diagram approximation of the general Bethe-Salpeter equation that assumes moderate ultrasound pressures. We expect this equation to be applicable to a wide spectrum of conditions in the ultrasound-modulated optical tomography of soft biological tissues.

In Chapter VI, we formally develop a temporal correlation transfer equation and a temporal correlation diffusion equation for ultrasound-modulated multiply scattered light, which can be used to calculate the ultrasound-modulated optical intensity in an optically scattering medium with a nonuniform ultrasound field and a heterogeneous distribution of optical parameters. We present an analytical solution based on correlation diffusion equation and Monte Carlo simulation results for scattering of the temporal autocorrelation function from a cylinder of ultrasound in an optically scattering slab. We further validate with experimental measurements the numerical calculations for an actual ultrasound field based on a finite-difference model of the correlation diffusion equation. The correlation transfer equation and correlation diffusion equation in this model are valid for moderate ultrasound pressures on a scale comparable with the optical transport mean free path, which must be greater than the ultrasound wavelength and smaller than or comparable to the sizes of both ultrasonic and optical inhomogeneities. These equations should also be applicable to a wide spectrum of conditions for ultrasound-modulated optical tomography of soft biological tissues.

Finally, in Chapter VII, a summary of the work is presented.

CHAPTER II
HIGH-RESOLUTION ULTRASOUND-MODULATED OPTICAL TOMOGRAPHY*

1. Introduction

Great effort has been made in the recent past to develop new imaging modalities based on the optical properties of soft biological tissues in the visible and near-infrared regions. At these wavelengths, radiation is nonionizing and the optical properties of biological tissues are related to the molecular structure, offering potential for the detection of functions and abnormalities.

Ultrasound-modulated optical tomography[2,3] is a hybrid technique that was proposed to provide better resolution for the optical imaging of soft biological tissue by combining ultrasonic resolution and optical contrast. Collective motions of the optical scatterers and periodic changes in the optical index of refraction are generated by ultrasound to produce fluctuations in the intensity of the speckles that are formed by the multiple-scattered light.[4,18,20] The ultrasound-modulated component of light carries information about the optical properties of tissue from the region of interaction between the optical and ultrasonic waves. However, it is a challenge to detect this modulated component efficiently because of diffused light propagation and uncorrelated phases among individual speckles. Several schemes for detection[3,4,7,8,10–13,21–23] have been explored. A CCD camera that provides parallel

*Reprinted with permission from S. Sakadžić and L. V. Wang, "High-resolution Ultrasound-modulated Optical Tomography in Biological Tissues," *Opt. Lett.* **29**, 2770 − 2772 (2004). Copyright 2002 Optical Society of America.

speckle detection[8,12,23] was used to produce a better signal-to-noise ratio than a single square-law detector. To obtain resolution along the ultrasonic axis, several groups of scientists explored various techniques, including an ultrasound frequency sweep,[11] computer tomography,[14] and tracking of ultrasound pulses[21] or short bursts.[22] The pulsed ultrasound approaches provide direct resolution along the ultrasonic axis and are more compatible with conventional ultrasound imaging. Pulsed ultrasound can have a much higher instantaneous power than continuous-wave (CW) ultrasound, reducing the undesired effect of the increased noise owing to its wide bandwidth.

In this work, for the first time to our knowledge, we report high-resolution ultrasound-modulated optical imaging with a long-cavity confocal FabryPerot interferometer (CFPI).[24] Our CFPI has a greater etendue — defined as the product of the acceptance solid angle and the area — than most CCD cameras and provides parallel speckle processing. In addition, a CFPI can detect the propagation of high-frequency ultrasound pulses in real time and tolerate speckle decorrelation. A CFPI is especially efficient at high ultrasound frequencies, where the background light can be filtered out effectively while the ultrasound-modulated component is transmitted. With our setup, optical features of ~ 100 μm in size embedded more than 3 mm below the surface of chicken breast tissue were resolved with high contrast in both the axial and the lateral directions.

2. Experimental Setup

The experimental setup is shown in Fig. 2.1. Samples were gently pressed through a slit along the Z axis to create a semi-cylindrical bump. The orthogonal ultrasonic and optical beams [Fig. 2.1(b)] were focused to the same spot below the sample

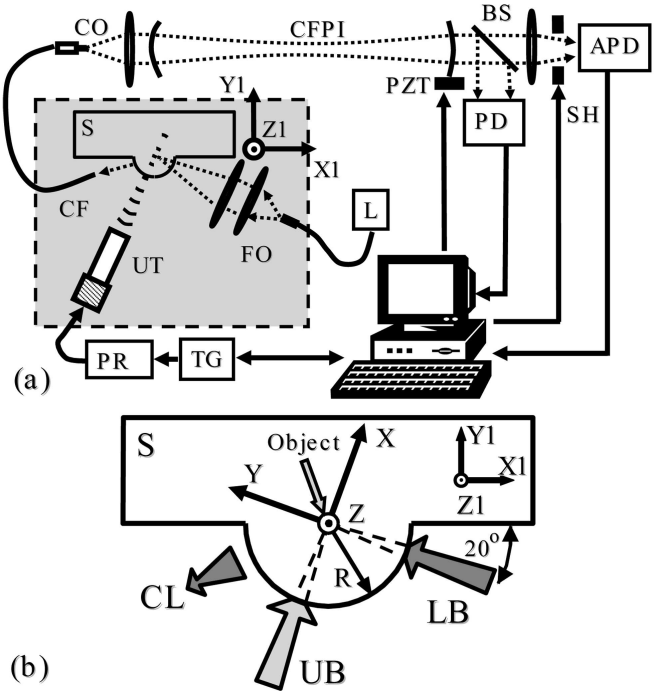

Fig. 2.1. Experimental setup. (a) Schematic of the experimental setup: L, laser; TG, trigger generator; PR, pulserreceiver; UT, ultrasonic transducer; FO, focusing optics; CF, collecting fiber; S, sample; CO, coupling optics; PZT, piezoelectric transducer; BS, beam splitter; SH, shutter; PD, photodetector. (b) Top view of the sample (S): UB, ultrasound beam; LB, incident light beam; CL, collected light; R, radius of curvature. Other abbreviations defined in text.

surface. Diffusely transmitted light was collected by an optical fiber with a 600 μm core diameter. This configuration minimized the contribution of unmodulated light from the shallow regions to the background and in addition enhanced the interaction between the ultrasound and some quasi-ballistic light that still existed at small imaging depths (up to one optical transport mean free path).

A focused ultrasound transducer (Ultran; 15-MHz central frequency, 4.7-mm lens diameter, 4.7-mm focal length, 15-MHz estimated bandwidth) was driven by a pulser (GE Panametrics, 5072PR). The ultrasound focal peak pressure was 3.9 MPa, within the ultrasound safety limit at this frequency for tissues without well-defined gas bodies.[25] The laser light (Coherent, Verdi; 532-nm wavelength) was focused onto a spot of $\sim$ 100-μm diameter below the surface of an otherwise scatter-free sample. The optical power delivered to the sample was 100 mW. Although the CW power in this proof-of-principle experiment exceeded the safety limit for average power, the duration of the samples exposure to light can be reduced to only a few microseconds for each ultrasound pulse propagation through the region of interest, and therefore the safety limit will not be exceeded in practice even if the focus is maintained in a scattering medium. The sample was mounted on a three-axis ($X1$, $Y1$, and $Z1$) translational stage. The ultrasound transducer and the sample were immersed in water for acoustic coupling. The light-focusing optics and the collecting fiber were immersed in the same water tank. The collected light was coupled into the CFPI, which was operated in a transmission mode (50-cm cavity length, 0.1-mm^2 sr etendue, $\sim$ 20 finesse). The light sampled by the beam splitter was used in a cavity tuning procedure. First we swept the cavity through one free spectral range to find the position of the central frequency of the unmodulated light. Then one CFPI mirror was displaced by a calibrated amount such that the cavity was tuned to the frequency of one sideband of the ultrasound-modulated light (15 MHz greater than

the laser light frequency). An avalanche photodiode (APD; Advanced Photonix) acquired the light filtered by the interferometer, and the signal was sampled at 100 Msamples/s with a data acquisition board (Gage, CS14100). A computer program written with LabView software controlled the movement of the CFPI mirror and the other sequences of the control signals.

A trigger generator (Stanford Research, DG535) triggered both ultrasound-pulse generation and data acquisition from the APD. As the resonant frequency of the CFPI cavity coincided with one sideband of the ultrasound-modulated light, the signal acquired by the APD during the ultrasound propagation through the sample represented the distribution of the ultrasound-modulated optical intensity along the ultrasonic axis and, therefore, yielded a one-dimensional (1D) image. In each operational cycle, first the resonant frequency of the CFPI was tuned and then data from 4000 ultrasound pulses were acquired in 1 s. Averaging over ten cycles was usually necessary to produce a satisfactory signal-to-noise ratio for each 1D image. We obtained two-dimensional images by scanning the sample along the Z direction and acquiring each corresponding 1D image.

3. Results and Discussion

Figure 2.2 presents a typical profile of the temporal dependence of the ultrasound-modulated light intensity during ultrasound-pulse propagation through the sample. The time of propagation was multiplied by 1500 ms^{-1}, the approximate speed of sound in the sample, to be converted into distance along the X axis, where the origin corresponded to the trigger for the signal acquisition from the APD. The sample, made from chicken breast tissue, was pressed through the 4-mm-wide slit. A long rod

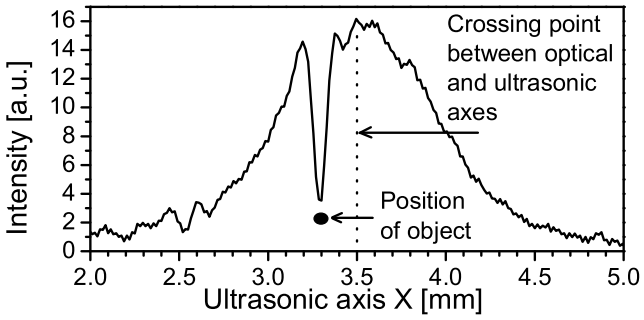

Fig. 2.2. Temporal dependence of the ultrasound-modulated light intensity during the propagation of an ultrasound pulse through the sample.

of 60-mm diameter, made from black latex, which was transparent for ultrasound but absorptive for light, was placed below the sample surface along the Z axis of the cylindrical tissue bump of a 2-mm radius. Because the profiles of the optical radiance and the ultrasound intensity within the sample determined the distribution of the ultrasound-modulated optical intensity, the maximum corresponded to the crossing point between the optical and the ultrasonic axes, as indicated in Fig. 2.2. The differences between the optical properties of the object and the tissue created a deep dip in the ultrasound-modulated light intensity when the ultrasound pulse passed through the object.

To investigate the axial and lateral resolutions, we imaged two chicken breast tissue samples (Fig. 2.3). The samples were prepared with 3.2- and 3-mm radii of curvature, respectively, in the cylindrical bumps. Two objects, shown in Figs. 2.3(b) and 2.3(d), were made from 100-mm-thick black latex and placed in the centers of curvature of the prepared samples, i.e., 3.2 and 3 mm below their respective surfaces. Their wide sides were parallel to the ultrasound beam and perpendicular to the light beam. We took the difference between the profiles of the modulated intensity along the X axis and the typical profile without objects present and, subsequently, divided

the difference by the latter profile point by point to obtain the relative profiles, which are shown as gray-scale images with five equally spaced gray levels from 0 to 1 [Figs. 2.3(a) and 2.3(c)]. Figure 2.3(e) presents the 1D axial intensity profiles along the X axis taken from the image in Fig. 2.3(a) at positions $Z = 15.11$ mm and $Z = 14.86$ mm, with an arbitrary origin. At position $Z = 15.11$ mm, the gap had an actual width of only 70 mm along the X axis and was resolved with 55% contrast. When the gap size was reduced to 50 mm at $Z = 14.86$ mm, the contrast decreased to 40%. Similarly, Fig. 2.3(f) presents the 1D lateral intensity profile along the Z axis taken from the image in Fig. 2.3(c) at $X = 3.17$ mm. The gap had an actual width of 120 μm along the Z axis and was resolved with a 50% contrast. If we use the minimal sizes of the resolvable gaps at 50% contrast as the resolutions, the estimated axial and lateral resolutions are 70 and 120 μm, respectively. However, the ultimate resolvable gap sizes at minimal contrast should be much smaller.

4. Conclusion

In summary, this study has demonstrated the feasibility of high-resolution ultrasound-modulated optical tomography in biological tissue with an imaging depth of several millimeters. A CFPI was shown to be able to isolate ultrasonically modulated light from the background efficiently in real time. The resolution can be further improved by use of higher ultrasound frequencies. This technology can easily be integrated with conventional ultrasound imaging to provide complementary information.

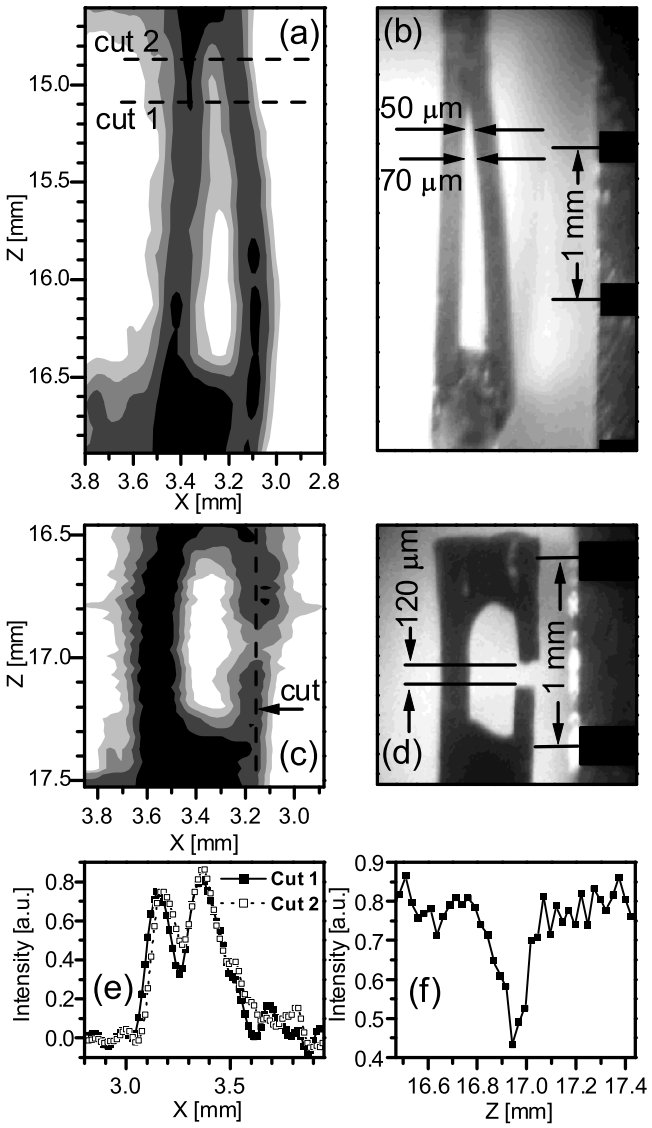

Fig. 2.3. Measurement of the axial and lateral resolutions. (a) Measurement and (b) image of an object, showing the axial resolution. (c) Measurement and (d) image of an object, showing the lateral resolution. (e) 1D axial profiles of intensity from the data in (a). (f) 1D lateral profile of intensity from the data in (c).

CHAPTER III
ULTRASONIC MODULATION OF MULTIPLY SCATTERED LIGHT: AN ANALYTICAL MODEL FOR ANISOTROPICALLY SCATTERING MEDIA*

1. Introduction

In spite of a variety of different experimental configurations that have been invented to efficiently measure the ultrasonically modulated component of the light emerging from biological tissue, the exact nature of the acousto-optical effect in a highly optically scattering medium is still not well understood due to the complicated light-ultrasound interaction that occurs in the presence of optical scatterers. Approximate theories in the optical diffusion regime under a weak scattering approximation have been developed that include one or both of the main mechanisms of modulation. Mechanism 1 is the optical phase variations that are due to the ultrasonically induced movement of the optical scatterers,[4,7] whereas mechanism 2 is the optical phase variations that are due to ultrasonically induced changes in the optical index of refraction. Mechanism 1 was first modeled by Leutz and Maret[4] in a case of isotropic optical scattering, where an homogeneous infinite scattering medium is traversed by a plane ultrasound wave. It was also modeled by Kempe et al.[7] Mechanism 2 was first modeled by Mahan et al.,[17] and it was subsequently combined together with the mechanism 1 by Wang.[18] In all cases, a weak scattering approximation

---

*Reprinted with permission from S. Sakadžić and L. V. Wang, "Ultrasonic Modulation of Multiply Scattered Coherent Light: An Analytical Model for Anisotropically Scattering Media", *Phys. Rev. E* **66**, 026603 (2002). Copyright 2002 by the American Physical Society.

is assumed and a method of diffusing-wave spectroscopy[5,6] is applied. In addition, the current models are based on nonabsorbing and isotropic scattering media rather than the more realistic absorbing and anisotropic scattering media.

In this paper we extend the solution for the temporal autocorrelation function of the electrical field component obtained in Ref.,[18] incorporating into the model a general scattering phase function. The organization of the paper is as follows. Section 2 describes the derivation of the autocorrelation function of the ultrasound-modulated electric field along paths of length s while the detailed derivations are deferred to the Appendix A. In Sec. 3 we incorporate the expressions obtained in Sec. 2 into the solution for the total electric field autocorrelation function transmitted through a scattering slab in the case of a plane source of coherent light and a point detector. We examine the accuracy of our analytical solution with an independent Monte Carlo simulation in Sec. 4. In Sec. 5 we use both the Monte Carlo simulation as well as the analytical solution for the autocorrelation function to explore the validity of the similarity relation. In Sec. 6, we present the dependence of the total electric field autocorrelation function on the ultrasonic and optical parameters including the ultrasonic frequency and amplitude as well as the scattering and absorption coefficient. Finally, a brief summary of our conclusions is presented.

2. Autocorrelation of a Single Pathlength

Consider the propagation of coherent light through a homogeneous scattering medium irradiated by a plane ultrasonic wave. If we neglect all the polarization effects, the temporal autocorrelation function of the electric field component of the scattered

light at the point detector position can be written as follows:

$$G_1(\tau) = \langle E(t)E^*(t+\tau)\rangle \,. \tag{3.1}$$

We assume that the photon mean free path is much longer than the optical wavelength (weak scattering) and the acoustic amplitude is much less than the optical wavelength. In this weak scattering approximation, the correlation between different random paths vanishes and only the photons traveling along the same path of length s produce a nonzero effect. Consequently, the autocorrelation function becomes[4,18]

$$G_1(\tau) = \int_0^{+\infty} p(s)\, \langle E_s(t)E_s^*(t+\tau)\rangle_U \, \langle E_s(t)E_s^*(t+\tau)\rangle_B \, ds, \tag{3.2}$$

where $p(s)$ is the probability density function of path length s. In Eq. (3.2) we assume that the contributions from Brownian motion (B) and ultrasound (U) are independent and that we can separate them.

The remaining task in this section is to consider the ultrasound component of Eq. (3.2) when photon scattering is anisotropic. Following the derivations in Refs.,[4,18] the autocorrelation for paths of length s can be written as

$$\langle E_s(t)E_s^*(t+\tau)\rangle_U = \left\langle \exp\left\{-i\left[\sum_{j=1}^{N}\Delta\phi_{n,j}(t,\tau) + \sum_{j=1}^{N-1}\Delta\phi_{d,j}(t,\tau)\right]\right\}\right\rangle \,. \tag{3.3}$$

In Eq. (3.3), $\Delta\phi_{n,j}(t,\tau) = \phi_{n,j}(t+\tau) - \phi_{n,j}(t)$, where $\phi_{n,j}(t)$ is the phase variation induced by the modulated index of refraction along the jth free path and $\Delta\phi_{d,j}(t,\tau) = \phi_{d,j}(t+\tau) - \phi_{d,j}(t)$, where $\phi_{d,j}(t)$ is the phase variation induced by the modulated displacement of the jth scatterer following the jth free path. Summation is going over all N free paths and $N-1$ scattering events along the photon path. Averaging is over time and over all the photon paths of length s. When the phase

variation is small (much less than unity), we can approximate Eq. (3.3) with

$$\left\langle E_s(t)E_s^*(t+\tau)\right\rangle_U = \exp\left[-F(\tau)/2\right] \ , \tag{3.4}$$

where the function $F(\tau)$ is

$$F(\tau) = \left\langle \left[\sum_{j=1}^{N} \Delta\phi_{n,j}(t,\tau) + \sum_{j=1}^{N-1} \Delta\phi_{d,j}(t,\tau)\right]^2 \right\rangle \ . \tag{3.5}$$

Let us assume that the plane ultrasound waves propagate along the Z direction with wave vector $\mathbf{k}_a = k_a\hat{\mathbf{e}}_a$, where $\hat{}$ indicates a unity vector, and $k_a = 2\pi/\lambda_a$, where λ_a is the ultrasonic wavelength. Along the photon path with N free paths, the positions of the $N-1$ scatterers are $\mathbf{r}_1,\ \mathbf{r}_2,\ ...,\ \mathbf{r}_{N-1}$. We will associate each free path between two consecutive scattering events with a vector $\mathbf{l}_j = \mathbf{r}_j - \mathbf{r}_{j-1}$, $(\mathbf{l}_j = l_j\hat{\mathbf{e}}_j)$. The expressions for $\Delta\phi_{n,j}(t,\tau)$ and $\Delta\phi_{d,j}(t,\tau)$ in terms of the ultrasound amplitude A, background index of refraction n_0, and the amplitude of the optical wave vector k_0 are[18]

$$\Delta\phi_{n,j}(t,\tau) = (4n_0k_0A\eta)\sin\left(\frac{1}{2}\omega_a\tau\right)\sin\left(\frac{1}{2}k_al_j\cos\theta_j\right)\frac{1}{\cos\theta_j} \times\cos\left[\omega_a\left(t+\frac{\tau}{2}\right) - \mathbf{k}_a\cdot\frac{\mathbf{r}_{j-1}+\mathbf{r}_j}{2}\right], \tag{3.6a}$$

$$\Delta\phi_{d,j}(t,\tau) = (2n_0k_0A)\sin\left(\frac{1}{2}\omega_a\tau\right)[(\hat{\mathbf{e}}_{j+1}-\hat{\mathbf{e}}_j)\cdot\hat{\mathbf{e}}_a]\cos\left[\mathbf{k}_a\cdot\mathbf{r}_j - \omega_a\left(t+\frac{\tau}{2}\right)\right], \tag{3.6b}$$

where coefficient η depends on the acoustic velocity of the material v_a, the density of the medium ρ, and the adiabatic piezo-optical coefficient $\partial n/\partial p$: $\eta = (\partial n/\partial p)\rho v_a^2$. In Eqs. (3.6), θ_j is the angle between the propagation directions of the light and ultrasound $(\cos\theta_j = \hat{\mathbf{e}}_a\cdot\hat{\mathbf{e}}_j)$, and $\omega_a = 2\pi f_a$, where f_a is the ultrasonic frequency. As in Ref.,[18] we assume that optical scatterers are oscillating due to the ultrasound with the same amplitude as the surrounding fluid, and that the phase of their oscillation is following the ultrasound pressure changes.

Now we can express the function $F(\tau)$ from Eq. (3.5) as

$$\begin{aligned} F(\tau) &= \left\langle \sum_{j=1}^{N} \Delta\phi_{n,j}^2(t,\tau) \right\rangle_{t,\,\Pi(s)} + \left\langle 2\sum_{j=2}^{N}\sum_{k=1}^{j-1} \Delta\phi_{n,j}(t,\tau)\Delta\phi_{n,k}(t,\tau) \right\rangle_{t,\,\Pi(s)} \\ &+ \left\langle \sum_{j=1}^{N-1} \Delta\phi_{d,j}^2(t,\tau) \right\rangle_{t,\,\Pi(s)} + \left\langle 2\sum_{j=2}^{N-1}\sum_{k=1}^{j-1} \Delta\phi_{d,j}(t,\tau)\Delta\phi_{d,k}(t,\tau) \right\rangle_{t,\,\Pi(s)} \\ &+ \left\langle 2\sum_{j=1}^{N}\sum_{k=1}^{N-1} \Delta\phi_{n,j}(t,\tau)\Delta\phi_{d,k}(t,\tau) \right\rangle_{t,\,\Pi(s)} . \end{aligned} \tag{3.7}$$

The averaging over time t of each term on the right side of Eq. (3.7) is an easy task, while the averaging over all the allowed paths $\Pi(s)$ of length s with N free paths is more difficult. In order to simplify the probability density function of a particular photon path $p(\mathbf{l}_1, ..., \mathbf{l}_N)$, we will first make some assumptions. The number of steps N in each photon path in the diffusion regime is much larger than unity. Consequently, even if the total path length s is fixed, the correlation between the lengths of free paths l_j is still weak. As a result, we have

$$p(\mathbf{l}_1, ..., \mathbf{l}_N) = p(l_1)p(l_2)...p(l_N)g(\hat{\mathbf{e}}_1, ..., \hat{\mathbf{e}}_N) , \tag{3.8}$$

where $p(l_j) = l^{-1}\exp(-l_j/l)$ is the probability density for a photon to travel a distance l_j between two scattering events, and $g(\hat{\mathbf{e}}_1, ..., \hat{\mathbf{e}}_N)$ is the probability density for the photon to travel along the directions $\hat{\mathbf{e}}_1, ..., \hat{\mathbf{e}}_N$. Because the probability of scattering a photon traveling in direction $\hat{\mathbf{e}}_j$ into direction $\hat{\mathbf{e}}_{j+1}$ is described with phase function $f(\hat{\mathbf{e}}_j \cdot \hat{\mathbf{e}}_{j+1})$, we can write Eq. (3.8) as

$$p(\mathbf{l}_1, ..., \mathbf{l}_N) = p_s(\hat{\mathbf{e}}_1)\prod_{j=1}^{N} p(l_j)\prod_{j=1}^{N-1} f(\hat{\mathbf{e}}_j \cdot \hat{\mathbf{e}}_{j+1}) , \tag{3.9}$$

where $p_s(\hat{\mathbf{e}}_1)$ is the probability density function of the starting photon direction $\hat{\mathbf{e}}_1$ in the scattering medium. Note that we assumed the phase function does not depend

on the azimuth angle or the incident direction.

Using Eq. (3.9) as the probability density function and going through some algebra (see the Appendix), Eq. (3.7) becomes

$$F(\tau) \simeq \frac{s}{l}(2n_0k_0A)^2 \sin^2\!\left(\frac{1}{2}\omega_a\tau\right)\left\{\eta^2\,(k_al)^2\,\mathrm{Re}\left[\hat{J}(\hat{I}-\hat{J})^{-1}\right]_{0,0} + \frac{1}{3}(1-g_1)\right\}\ , \quad (3.10)$$

where $\mathrm{Re}\left[\hat{J}(\hat{I}-\hat{J})^{-1}\right]_{0,\,0}$ represents the real part of the $(0,0)$ element of the matrix $\hat{J}(\hat{I}-\hat{J})^{-1}$ and the elements of the matrix $\hat{J}$ are defined as

$$\begin{aligned} J_{m,\,n} &= g_m^{1/2} g_n^{1/2} \sqrt{\frac{2m+1}{2}} \sqrt{\frac{2n+1}{2}} \int_{-1}^{1} T(x) P_m(x) P_n(x) dx, \qquad (3.11) \\ T(x) &= \frac{1}{1-ik_alx}\ , \end{aligned}$$

where $P_j(x)$ is a Legendre polynomial of order j, and g_j is the jth Legendre polynomial expansion coefficient of the scattering phase function [Eq. (A.2)]. Thus, g_1 is equal to the scattering anisotropy factor g, i.e., the average cosine of the scattering angle. The value $\mathrm{Re}\left[\hat{J}(\hat{I}-\hat{J})^{-1}\right]_{0,\,0}$ is the limit of the $\mathrm{Re}\left[\hat{J}_Q(\hat{I}_Q-\hat{J}_Q)^{-1}\right]_{0,\,0}$ when Q approaches infinity, where $\hat{J}_Q$ is the $Q \times Q$ matrix whose elements are defined by Eq. (3.11).

We will rearrange the expression for $F(\tau)$ to

$$F(\tau) = s(2n_0k_0A)^2 \sin^2\left(\omega_a\tau/2\right)\left(\delta_n + \delta_d\right)\ , \qquad (3.12)$$

where

$$\delta_n = \eta^2 k_a^2 l\ \mathrm{Re}\left[\hat{J}(\hat{I}-\hat{J})^{-1}\right]_{0,\,0}\ , \qquad \delta_d = \frac{1-g}{3l}.$$

3. Autocorrelation for a Slab: Analytical Solution

In this section, we will test the accuracy of our analytical expression for $F(\tau)$ from the preceding section with an independent Monte Carlo simulation in the case of an infinitely wide scattering slab. Slab geometry has been considered previously for various particular problems.[4–6,18,19,26,27] We will solve Eq. (3.2) for anisotropically scattering and absorbing media based on the expression for function $F(\tau)$ obtained in the preceding section.

The Z axis of the coordinate system is perpendicular to the infinitely wide slab of thickness L. The index of refraction of both the surrounding and scattering media is n_0. A plane ultrasonic wave propagates along the slab (in the $X-Y$ plane) and is assumed to fill the whole slab. At the same time, one side of the slab is irradiated by a plane electromagnetic wave, and a point detector measures the temporal autocorrelation function of the electric field component on the other side of the slab. By solving the diffusion equation for such geometry, it is possible to find a reasonably good expression[18,26,27] for the photon path length probability density function $p(s)$. We follow the derivation of $p(s)$ from Refs.[18,26] by applying an infinite number of image sources and introducing extrapolated-boundary conditions[26,27] to obtain the following expression:

$$\begin{aligned} p(s) &= K(s)\sum_{i=0}^{\infty}\left\{\left[(2i+1)\,L_0 - z_0\right]\exp\left(-\frac{\left[(2i+1)\,L_0 - z_0\right]^2}{4Ds}\right)\right. \\ &\quad \left. -\left[(2i+1)\,L_0 + z_0\right]\exp\left(-\frac{\left[(2i+1)\,L_0 + z_0\right]^2}{4Ds}\right)\right\}\ , \end{aligned} \tag{3.13}$$

$$K(s) = \frac{1}{2\sqrt{\pi D}}\,\frac{\sinh\left(L_0\sqrt{\mu_a D^{-1}}\right)}{\sinh\left(z_0\sqrt{\mu_a D^{-1}}\right)}\,s^{-3/2}\exp\left(-\mu_a s\right)\ ,$$

where $D = l^*/3$ is the diffusion constant; L_0 is the distance between the two ex-

trapolated boundaries of the slab; z_0 is the location of the converted isotropic source from the extrapolated incident boundary of the slab; and l^* is the isotropic scattering mean free path defined as $l^* = l/(1-g)$. The distance between the extrapolated boundary and the corresponding real boundary of the slab is $l^*\gamma$ ($\gamma = 0.7104$). The converted isotropic source is one isotropic scattering mean free path into the slab. Therefore, $L_0 = L + 2l^*\gamma$, and $z_0 = l^*(1+\gamma)$.

Incorporating the influence of Brownian motion of scatterers[4–6] and the expression for $F(\tau)$, we can solve the integration in Eq. (3.2) over s for the temporal autocorrelation function:

$$\begin{aligned} G_1(\tau) &= C\,\frac{\sinh\left(z_0\sqrt{(S_U+S_B+\mu_a)D^{-1}}\right)}{\sinh\left(L_0\sqrt{(S_U+S_B+\mu_a)D^{-1}}\right)}\,, \\ C &= \sinh\left(L_0\sqrt{\mu_a D^{-1}}\right)/\sinh\left(z_0\sqrt{\mu_a D^{-1}}\right)\,, \end{aligned} \tag{3.14}$$

where $S_B = 2\tau/(\tau_0 l^*)$ is the term due to Brownian motion (τ_0 is the single-particle relaxation time), and S_U is the term due to the ultrasonic influence:

$$S_U = \frac{1}{2}(2n_0k_0A)^2\sin^2(\omega_a\tau/2)\,(\delta_n+\delta_d)\ . \tag{3.15}$$

4. Monte Carlo Simulation

To provide an independent numerical approach, we modified the existing public-domain Monte Carlo package[28] for the transport of light in scattering media to sample the autocorrelation function according to Eqs. (3.2) and (3.3). Because it would be very time-consuming to physically simulate a point detector using the Monte Carlo code, we applied the principle of reciprocity in our simulation: the slab is illuminated by a point source and the transmitted light is collected by a

plane detector. The scattering angle of a photon in our Monte Carlo simulation is determined by the Henyey-Greenstein phase function,[29] but it would be trivial to extend it to any analytically or numerically defined phase function. For details of the Monte Carlo implementation, refer to Ref.[19]

As a first comparison between our analytical solution and the Monte Carlo simulation, we neglect both the optical absorption by setting μ_a to zero and the Brownian motion effect by setting $\tau_0 \to \infty$. In Eqs. (3.14) and (3.15) we see that the value of $G_1(\tau)$ oscillates between 1 at $\tau = 0$ and the minimum value at $\tau = \pi/\omega_a$. The maximum variation of $G_1(\tau)$ is compared for different values of $k_a l$ while k_a and the ratio L/l (the number of mean free paths in a slab of thickness L) are kept constant. We repeat the test for several different values of the scattering anisotropy factor g and the acoustic amplitude A.

The results are shown in Fig. 3.1. The analytical predictions (solid lines in Fig. 3.1) fit the Monte Carlo calculations (empty scatterers) very well. In general, increasing the value of g leads to a decreased maximum variation of $G_1(\tau)$ due to a decreased number of equivalent isotropic scattering events inside the slab. Further, a larger ultrasonic amplitude increases the maximum variation of the temporal autocorrelation function due to the larger movement of scattering centers and greater modulation of the index of refraction. Finally, the maximum variation grows in a slab geometry with $k_a l$ due to the larger value of the product $l\delta_n$, while the product $l\delta_d$ remains unchanged. From Fig. 3.1 we see that our analytical model works well for a wide range of $k_a l$ even when the anisotropy factor is non-zero. However, for $k_a l < 1$ the results should be taken with a caution, since our analytical model is valid for higher values of the $k_a l$ product (see the Appendix).

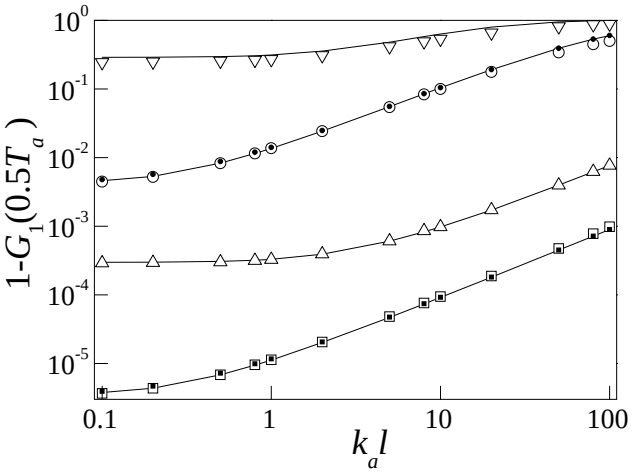

Fig. 3.1. The $k_a l$ dependence of the maximum variation of the temporal autocorrelation function. Different lines are for different values of the scattering anisotropy factor g and the acoustic amplitude A. Empty symbols indicate the Monte Carlo results: $\square$ ($g = 0.9$, $A = 0.1$ Å), $\triangle$ ($g = 0$, $A = 0.1$ Å), $\bigcirc$ ($g = 0.9$, $A = 3.5$ Å), $\bigtriangledown$ ($g = 0$, $A = 3.5$ Å). Solid lines indicate the analytical results. Filed symbols indicate the analytical results as well but by using the similarity relation. The following parameters are used in the calculations: $L/l = 127.35$, the wavelength of light *in vacuo* is $\lambda_0 = 500$ nm, $n_0 = 1.33$, $f_a = 1$ MHz, $v_a = 1480$ m/s, and $\eta = 0.3211$.

5. Similarity Relation

In this section, we will explore a similarity relation using the verified analytical solution, rather than the numerical solution shown previously.[19] In intensity-based photon transport theory, there is a similarity relation:[30] if the transport scattering coefficient $\mu_s^*[= \mu_s(1-g)]$ remains constant when the scattering coefficient μ_s and the scattering anisotropy factor g vary, the spatial distribution of light intensity will be approximately the same. The similarity relation $[\mu_s^* = \mu_s(1-g)]$ can be rewritten as $l^* = l/(1-g)$, where l^* is the isotropic scattering mean free path. Here, we will examine the counterpart of this conventional similarity relation in the ultrasonic modulation of coherent light. In other words, we will compare two cases: (1) the scattering coefficient is μ_s and the scattering anisotropy factor is g and (2) the scattering coefficient is $\mu_s^*[= \mu_s(1-g)]$ and the scattering anisotropy factor is zero. In the following text, the symbols with * indicate case (2).

In Eq. (3.12) we see that the values of δ_d for both the cases are exactly the same ($\delta_d = \delta_d^*$). On the other hand, the matrix $\hat{J}$ for the isotropic case (2) reduces to only one number: $\chi = \arctan(k_a l^*)/(k_a l^*)$ and we have $\delta_n^* = \eta^2 k_a^2 l^* \chi/(1-\chi)$.[18] However, the matrix $\hat{J}$ for the general case (1) is quite complicated, and a direct analytical comparison with case (2) is difficult. Instead, we will plot the relative error between the two cases.

From Fig. 3.2(a), we see that the discrepancy between δ_n^* and δ_n is not very large (less than 13 percent), even when the scattering anisotropy factor g is 0.9. The error grows with g and has a maximum around $k_a l^* = 2$. Because the δ_d part of the sum $\delta = \delta_n + \delta_d$ is unchanged by the similarity transformation, the relative difference between δ^* and δ is even smaller. From Fig. 3.2(b) we see that the relative error of

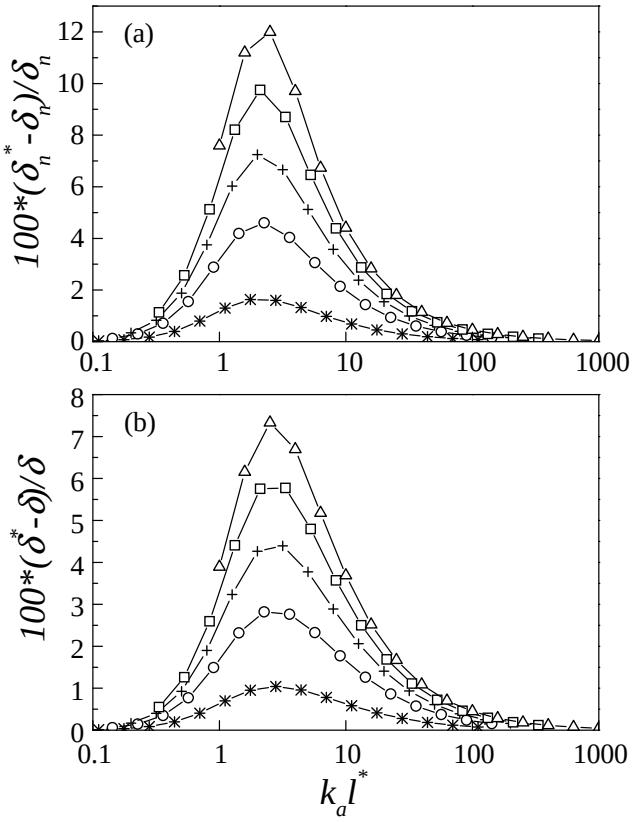

Fig. 3.2. Relative error due to the similarity relation for different $k_a l^*$ and g values. (a) Relative error of δ_n^*. (b) Relative error of δ^*. Lines ($*$, ◯, $+$, □, △) represent respectively (0.1, 0.3, 0.5, 0.7, 0.9) values of the scattering anisotropy factor g.

δ^* is less than 8% M/u. The validity of the similarity relation can also been seen in Fig. 3.1 (Sec. 4).

In conclusion, with a relatively small error, we can apply the similarity relation in the calculation of the temporal autocorrelation function under the conditions we considered during the derivation of $F(\tau)$ and $G_1(\tau)$.

6. Dependence on Ultrasonic and Optical Parameters

In this section we will explore the dependence of the autocorrelation function on the ultrasonic and optical parameters in a slab geometry [Figure 3.3]. Since it has been shown that the similarity relation can be applied successfully when scattering is anisotropic, we consider only isotropic scattering. In all of the cases we neglect Brownian motion and calculate the value of $1 - G_1(\tau)$ at one half of an ultrasonic period (solid lines in Fig. 3.3) according to the analytical solution [Eq. (3.14)]. The symbols represent the Monte Carlo results.

Figure 3.3(a) shows that the maximum variation decays when the absorption coefficient increases. This is because a higher absorption coefficient reduces the fraction of photons of long path length reaching the detector. Because these long-path-length photons contribute most to modulation, the maximum variation decreases.

Figure 3.3(b) shows that the maximum variation increases with acoustic frequency, when the amplitude of oscillation A is kept constant. If the ultrasonic power is constant, values on Fig. 3.3(b) should be divided by f_a^2, and the maximum variation will decay with acoustic frequency. This is because a higher acoustic frequency leads to a higher ratio between the scattering mean free path and the ultrasonic wavelength, which decreases the contribution from the index of refraction (δ_n) but

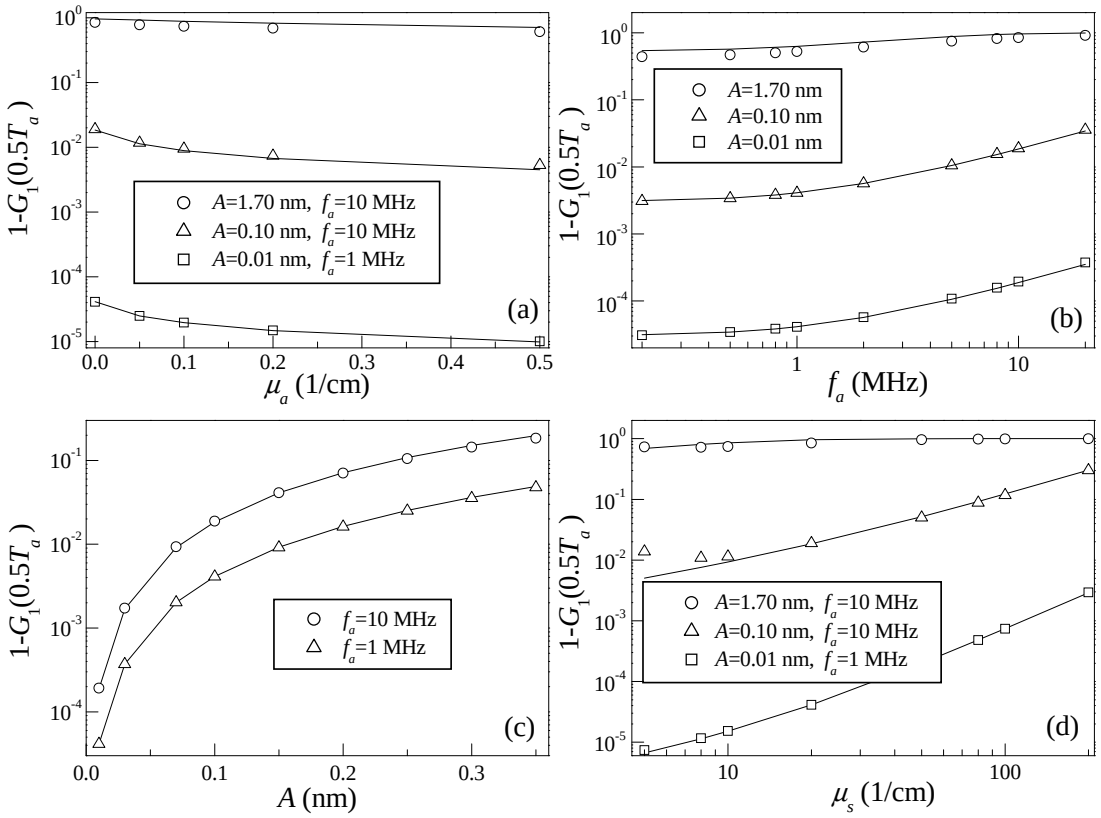

Fig. 3.3. Dependence of the maximum variation of the temporal autocorrelation function on different ultrasonic and scattering parameters. Solid lines represent the analytical predictions and symbols represent the Monte Carlo results. (a) Dependence on the absorption coefficient at different values of ultrasonic frequency and amplitude. (b) Dependence on the ultrasonic frequency at different values of ultrasonic amplitude. (c) Dependence on the ultrasonic amplitude at different values of ultrasonic frequency. (d) Dependence on the scattering coefficient at different values of ultrasonic frequency and amplitude. The following parameters are used in the calculation: $v_a = 1480$ m/s, $\eta = 0.3211$, $n_0 = 1.33$, $L = 2$ cm, $\mu_s = 20$ cm^{-1} [except in (d)], $\mu_a = 0$ [except in (a)], and $g = 0$.

has no effect on the contribution from displacement (δ_d) at the high values of the product $k_a l$.

Figure 3.3(c) shows that the maximum variation increases with the acoustic amplitude. A greater ultrasonic amplitude increases the maximum variation by increasing both the scatterer displacement (δ_d) and the index of refraction change (δ_n).

Figure 3.3(d) shows that the maximum variation increases with the scattering coefficient. This is because an increase in the scattering coefficient μ_s leads to a smaller value of the photon mean free path and a higher number of photon scatterings along the paths. A higher number of photon scatterings along the paths produces a higher maximum variation in the autocorrelation function.

In all the cases, we tried to present situations with a small maximum variation (choosing small amplitude and frequency of ultrasound) as well as situations when the maximum variation is near unity (usually when the ultrasound amplitude or frequency is high). In all of these cases, the analytical predictions fit the Monte Carlo results well. However, the error of the analytical prediction grows when the maximum variation is large and when the average number of photon steps along the paths is small. The data is in agreement with our assumptions made during the derivation of $F(\tau)$, i.e., the accumulated phase change along the photon paths is small enough to apply the approximation between Eqs. (3.2) and (3.4), and that we are in the diffusion regime, which was necessary for the derivation of $F(\tau)$ in the Appendix, as well as for the derivation of the photon path-length probability density [Eq. (3.13)].

7. Conclusion

In conclusion, we have presented an analytical solution for the autocorrelation function of an ultrasound-modulated electric field along a path with N scatterers when scattering is anisotropic. A further analytical solution was found for the light transmitted through a scattering slab using a plane source and a point detector. Using a Monte Carlo simulation, we verified the accuracy of the analytical solution. We also tested the similarity relation and showed that it can be used as a good approximation in the calculation of the autocorrelation function. Finally, we presented the dependence of the maximum variation of the autocorrelation function on different ultrasonic and optical parameters. In general, increasing ultrasonic amplitude and increasing the scattering coefficient leads us to a larger maximum variation while increasing the absorption coefficient or ultrasonic frequency leads us to a smaller maximum variation. Our analytical solution is valid under the following conditions: diffusion regime transport, a small ultrasonic modulation, and when the value of $k_a l$ is not too small.

CHAPTER IV
MODULATION OF MULTIPLY SCATTERED LIGHT BY ULTRASONIC PULSES: AN ANALYTICAL MODEL*

1. Introduction

The existing theoretical model[18,20] was developed for the interaction of a plane, monochromatic (CW) ultrasound wave with diffused light in an infinite scattering medium, neglecting the polarization effects. It is assumed that the ratio of the optical transport mean free path l_{tr} to the ultrasonic wavelength λ_a is large enough that the ultrasound induced optical phase increments associated with different scattering events are weakly correlated.[7,20] However, this assumption may not be valid in cases where broadband pulsed ultrasound is applied, which is a promising option for the development of soft tissue imaging technology based on the ultrasound modulation of light.[22,31,32]

In this work, we extend present theory to cases where broadband ultrasound pulses interact with diffused light. In Sec. 2, we generalize the relation between the ultrasound induced optical scatterer movement and the fluid displacement in accordance with the analytical solution for a small rigid sphere oscillation in a viscous fluid. In Sec. 3, we develop an expression for the time averaged temporal autocorrelation function of the electrical field component associated with the optical paths of length s in turbid media, when an infinite train of ultrasonic pulses traverse the

---

*Reprinted with permission from S. Sakadžić and L. V. Wang, "Modulation of Multiply Scattered Coherent Light by Ultrasonic Pulses: An Analytical Model", *Phys. Rev. E* **72**, 036620 (2005). Copyright 2005 by the American Physical Society.

media. The approximate similarity relation is valid for a broad range of l_{tr}/λ_a values. We show that, in general, a correlation exists between the phase increments due to scatterer displacement and phase increments due to index of refraction changes even when the value of l_{tr}/λ_a is large. In Sec. 4, we explore the influence of ultrasound frequencies on the behavior of ultrasound-modulated optical intensity. We also compare a simple heuristic Raman-Nath solution for the acousto-optical effect in a clear medium with our solution for the behavior of the modulated intensity. In Sec. 5, we present a complete solution for ultrasound modulation for a few distinct profiles of ultrasound pulses in slab transmission and reflection geometry. Finally, a summary of the results is presented.

2. Ultrasound Induced Movement of the Optical Scatterers

In general, the equations governing the ultrasound induced motion of a particle in a fluid are complex. In this work, we consider the oscillations of a small rigid spherical particle in a viscous flow, with no-slip conditions applied on the surface of the particle. It is assumed that the Reynolds number is much smaller than unity, and that the particle radius a_0 is smaller than the smallest scale in the flow. The Reynolds number is given by $a_0 W/\eta_k$, where η_k is the kinematic viscosity of the fluid, and W represents the amplitude of the relative sphere velocity in respect to the velocity of the surrounding fluid. These conditions are likely to be satisfied by optical scatterers in biological soft tissues, if we assume the ultrasound fields commonly generated in practice.

The equations derived for the general case of nonuniform flow[33,34] can be simplified significantly if we consider the plane ultrasonic wave and neglect the effect

of gravity. In the latter case, the relation between the Fourier transform of fluid velocity $\tilde{u}(f)$ and the Fourier transform of particle velocity $\tilde{v}(f)$ is given by[35,36]

$$\tilde{v}(f) = \tilde{u}(f)Y(f_r, \gamma), \tag{4.1}$$

where

$$Y(f_r, \gamma) = \frac{1 - if_r - (i-1)(3f_r/2)^{1/2}}{1 - i(2\gamma+1)f_r/3 - (i-1)(3f_r/2)^{1/2}}. \tag{4.2}$$

In Eq. (4.2), the relative ultrasonic frequency, $f_r = f/\nu_0$, is calculated in respect to $\nu_0 = 3\eta_k/(2\pi a_0^2)$; $i = \sqrt{-1}$ is the imaginary unit; and $\gamma = \hat{\rho}/\rho$ is the relative sphere density where $\hat{\rho}$ and ρ are densities of the sphere and the fluid, respectively. The Fourier transform of the function $c(t)$ is given by

$$\tilde{c}(f) = \int_{-\infty}^{+\infty} c(t) \exp(i2\pi f t) dt. \tag{4.3}$$

As shown in Ref.,[36] when the relative density of a particle such as an exogenous microbubble ultrasound contrast agent is low ($\gamma < 1$), the amplitude of the particle oscillation is greater than the amplitude of the fluid oscillation, and the phase of the particle oscillation precedes the phase of the fluid oscillation. However, in soft biological tissue, an endogenous optical scatterer has a density just slightly greater than the density of the surrounding medium. Also, the kinematic viscosity should be greater than, or equal to, the kinematic viscosity of water, which is approximately $10^{-6}\mathrm{m}^2\mathrm{s}^{-1}$ at room temperature. In that case, the amplitude of the scatterer oscillation is slightly smaller than the amplitude of the medium oscillation, and the phase of the scatterer movement is slightly retarded in respect to the fluid movement. Therefore, the movement of the optical scatterer is expected to follow closely the movement of the surrounding fluid, although this model might be too simple to fully account for the complexities of real biological tissue.

3. Temporal Autocorrelation Function for the Train of Ultrasound Pulses

In this model, we consider the independent multiple scattering of temporarily coherent diffused light in a scattering medium homogeneously filled with discrete optical scatterers in a general case of anisotropic optical scattering. We neglect the polarization effects and assume that the optical wavelength λ_0 is much smaller than the scattering mean free path l. We also assume that an ultrasonic plane wave is propagating unperturbed along the x axis without attenuation. The acoustical pressure in the medium is given by $P(\mathbf{r}, t) = P_0 f(x, t)$, where P_0 is the pressure amplitude, and the pressure propagation is represented by the function $f(x, t)$. Analogous to previous work[37,38] where the acousto-optical effect caused by pulsed ultrasound is analyzed in a clear medium, we assume that the pressure propagation function $f(x, t)$ represents an infinite train of ultrasound pulses

$$f(x,t) = \sum_{n=-\infty}^{+\infty} f_0(x - v_a t - n v_a T), \tag{4.4}$$

where v_a is the ultrasonic speed, and T is the time period between ultrasound pulses. The shape of the single ultrasonic pulse is given by function $f_0(x - v_a t)$.

The power spectral density (PSD) of the scattered light at the position of a point detector can be represented as

$$\mathcal{P}(\nu) = \int_{-\infty}^{+\infty} \Gamma(\tau) e^{i2\pi\nu\tau} d\tau, \tag{4.5}$$

where $\Gamma(\tau)$ is the time averaged autocorrelation function of the electrical field.[39]

We assume in this simple model that due to the weak scattering approximation ($l/\lambda_0 \gg 1$), the fields belonging to different random paths add incoherently to the

average and that only photons traveling along the same path of length s contribute to the autocorrelation function.[4,5,40–42] Consequently, the time averaged autocorrelation function of the electrical field can be written as

$$\Gamma(\tau) = \int_0^\infty p(s)\Gamma_s(\tau)ds, \tag{4.6}$$

where $p(s)$ is the probability density function that the optical paths have length s, and $\Gamma_s(\tau)$ is the time averaged autocorrelation function of the electrical field associated with the paths of length s. We further assume the independence of the optical phase increments induced by the Brownian motion of the scatterers and those induced by ultrasound through mechanisms 1 and 2. Then, $\Gamma_s(\tau)$ can be represented as $\Gamma_{s,U}(\tau)\Gamma_{s,B}(\tau)$, where the indices B and U are associated with the Brownian motion and the ultrasonic effects, respectively. The influence of Brownian motion has been considered previously in the literature,[5,20,40,43] and it can be expressed as $\Gamma_{s,B}(\tau) = \exp[-2s\tau/(l_{tr}\tau_0)]$, where l_{tr} is the optical transport mean free path, and τ_0 is the single particle relaxation time.

To obtain the value of $\Gamma_{s,U}(\tau)$, we first consider phase φ_s of the electrical field component accumulated along the optical path of length s in optically diffusive media. The value of the electrical field component in the analytic signal representation is then proportional to $\exp[-i(\omega_0 t - \varphi_s)]$, where $\omega_0 = 2\pi f_0$, and f_0 is the optical frequency of the incident monochromatic light.

We assume that the perturbation of the dielectric permittivity of the medium due to the ultrasound is small and proportional to the ultrasound pressure. Consequently, perturbation of the optical index of refraction $n(x,t)$ due to ultrasound is also small and we have

$$n(x,t) \approx n_0 \left[1 + \frac{1}{2}Mf(x,t)\right]. \tag{4.7}$$

In Eq. (4.7), modulation coefficient M is equal to $2\eta P_0/\rho v_a^2$, and $\eta = \rho\partial n/\partial\rho$ is the elasto-optic coefficient (we assume for water $\eta \approx 0.32$). For soft biological tissues and for commonly applied ultrasonic pressures, the value of the modulation coefficient M is always much less than unity, which is in good agreement with the approximation we arrived at in Eq. (4.7).

For an optical path of length s, which begins at $\mathbf{r}_0$ and ends at $\mathbf{r}_{N+1}$ and has N scatterers at positions $\mathbf{r}_1$,...,$\mathbf{r}_N$, the value of the accumulated optical phase calculated by integrating the index of refraction along the path is approximately equal to[18,20]

$$\begin{aligned}\varphi_{s,N} &\approx k_0 n_0 \sum_{i=0}^{N} |\mathbf{r}_{i+1} - \mathbf{r}_i| + k_0 n_0 \sum_{i=1}^{N} (\chi_i - \chi_{i+1}) e_i(t) \\ &\quad + k_0 n_0 \sum_{i=0}^{N} \frac{1}{2} M \int_{\mathbf{r}_i}^{\mathbf{r}_{i+1}} f(x,t)dr. \end{aligned} \tag{4.8}$$

In Eq. (4.8), integrations in the last term are performed along the straight lines which connect consecutive scatterers; $k_0 = 2\pi/\lambda_0$ is the magnitude of the optical wave vector; $\chi_{i+1} = \cos(\theta_{i+1})$, where θ_{i+1} is the angle between ultrasound wave-vector $\mathbf{k}_a$ and the vector $\mathbf{l}_{i+1} = \mathbf{r}_{i+1} - \mathbf{r}_i$ which connects two consecutive scatterers; and $e_j(t)$ is the projection of the ultrasound induced displacement of the jth particle $\mathbf{e}_j(t)$ at time t in the ultrasound propagation direction. Comparing Eq. (4.8) with the previous derivations,[20] one more scatterer is included along the optical path for the convenience of the later averaging.

Several additional assumptions are included in Eq. (4.8). The ultrasound induced displacements of the scatterers are neglected in the limits of the integrals in the last term on the right-hand side of Eq. (4.8), which is a reasonable approximation when $k_0 n_0 M|\mathbf{e}_j(t)| \ll 2$ and at the same time $|\mathbf{e}_j(t)| \ll l$. In that way, the phase error due to the approximation is much smaller than one radian for each integral between two scatterers, and the total value of the error in each integration is much

smaller than the integral itself, except in some cases where the value of the integral approaches zero due to increased phase cancelation when integrating occurs along the direction close to the ultrasound propagation direction. However, these cases contribute little to the total phase value. We also assume that the distance between consecutive scatterers can be approximated with $l_{i+1} + \chi_{i+1}[e_{i+1}(t) - e_i(t)]$, which is the case when $k_0 n_0 e_i^2(t) \ll 2l$, and $|e_i(t)| \ll l$. Finally, the accumulated phase $\varphi_{s,N}$ is calculated by integrating the optical phase increments along the straight lines which connect the scatterers along the optical path. Therefore, it is assumed that the distortion of the optical waves along the path between two consecutive scatterers due to ultrasound induced change in the optical index of refraction is negligible. Analogous to the Raman-Nath case of acousto-optical diffraction in clear media,[44] we write this condition as $Q\nu_{\mathrm{RN}} \ll 1$, where $Q = lk_a^2/k_0$ and $\nu_{\mathrm{RN}} = k_0 l n_0 M/2$ are the Klein-Cook parameter and the Raman-Nath parameter, respectively. For the optical wavelengths in the visible and near-infrared regions in soft biological tissues and for common ultrasound pressures, the applied approximations limit the range of the ultrasound frequency values between ≈ 1 kHz and several tens of MHz. This can also be considered as a lower limit for the $k_a l$ product between 10^{-2} and 10^{-3}, and an upper limit for the $k_a l$ product around 100, depending on the precise values of the parameters.

We also assume in Eq. (4.8) that $e_0(t) = e_{N+1}(t) = 0$, i.e., the displacements of the first and last scatterer (source and detector) are zero. It will be shown that this assumption is valid when the number of the scattering events along the path is very large, regardless of the value of the $k_a l$ product. However, when the $k_a l$ product is small, and N is as small as 10, ultrasound induced movement of the source and detector leads to a significant difference in effect due to mechanism 1.

Since the time invariant part associated with $|\mathbf{r}_{i+1} - \mathbf{r}_i|$ in Eq. (4.8) has no

influence on the spectral properties of light, we consider only the other two terms, and write the ultrasound induced optical phase increment along the path as

$$\varphi_s(H,t) = k_0 n_0 \sum_{i=1}^{N} (\chi_i - \chi_{i+1}) e_i(t) + \frac{1}{2} k_0 n_0 M \sum_{i=0}^{N} \int_{\mathbf{r}_i}^{\mathbf{r}_{i+1}} f(\mathbf{r},t)\, dr, \tag{4.9}$$

In Eq. (4.9), term H represents the set of random variables $\{\mathbf{r_0}, \chi_1, l_1, ..., \chi_{N+1}, l_{N+1}\}$ associated with the paths of length s with N scatterers. The probability density functions (PDF) of the first scatterer position and the cosines of the starting angle χ_1 are uniform. Also the PDF of the optical pathlength between two scattering events is given by $p(l_j) = l^{-1} \exp(-l_j/l)$, where l is the mean optical free path. Finally, the probability density of scattering a photon traveling in direction $\mathbf{e}_i = \mathbf{l}_i/l_i$ into direction $\mathbf{e}_{i+1} = \mathbf{l}_{i+1}/l_{i+1}$ is described with the phase function $g(\mathbf{e}_j \cdot \mathbf{e}_{j+1})$ which does not depend on the azimuth angle or the incident direction. The development of the phase function $g(\mathbf{e}_j \cdot \mathbf{e}_{j+1})$ over the Legendre polynomials $P_m(\mathbf{e}_j \cdot \mathbf{e}_{j+1})$ is given by

$$g(\mathbf{e}_j \cdot \mathbf{e}_{j+1}) = \sum_{m=0}^{\infty} \frac{2m+1}{2} g_m P_m(\mathbf{e}_j \cdot \mathbf{e}_{j+1}), \tag{4.10}$$

where $g_0 = 1$, and g_1 is the scattering anisotropy factor.

Now, we calculate the power spectral density of the optical intensity as a Fourier transform of the time averaged autocorrelation function.[39] It is interesting to note at this point that the random process associated with the sample functions $\varphi_s(H,t)$ is not wide sense stationary unless the diameter of the whole scattering volume is much larger than the ultrasound wavelength. In that case, averaging over $\mathbf{r}_0$ cancels the time dependence of the autocorrelation function.

We adopt the notation $\Delta\varphi_s = \varphi_s(H, t+\tau) - \varphi_s(H,t)$, such that the time averaged autocorrelation function $\Gamma_{s,U}(\tau)$ is expressed as

$$\Gamma_{s,U}(\tau) = \exp(-i\omega_0\tau) \left\langle \exp(i\Delta\varphi_s) \right\rangle_{t,H}. \tag{4.11}$$

In Eq. (4.11), $\langle\ \rangle_{t,H}$ represents averaging over time, and averaging over all of the random variables in H.

We proceed by representing the $\Delta\varphi_s$ with the help of Eq. (4.9), as

$$\Delta\varphi_s = \Delta\varphi_{s,n} + \Delta\varphi_{s,d}. \tag{4.12}$$

In Eq. (4.12), $\Delta\varphi_{s,n}$ is associated with index of refraction changes along the optical path

$$\Delta\varphi_{s,n} = \frac{1}{2}k_0 n_0 M \sum_{i=0}^{N} \int_{\mathbf{r}_i}^{\mathbf{r}_{i+1}} \Delta f(\mathbf{r}, t, \tau) dr, \tag{4.13}$$

where $\Delta f(\mathbf{r}, t, \tau) = f(\mathbf{r}, t+\tau) - f(\mathbf{r}, t)$. Similarly, term $\Delta\varphi_{s,d}$ on the right-hand side of Eq. (4.12) is associated with the ultrasound induced movement of the scatterers

$$\Delta\varphi_{s,d} = k_0 n_0 \sum_{j=1}^{N} (\chi_j - \chi_{j+1}) \Delta e_j(t, \tau), \tag{4.14}$$

where $\Delta e_j(t, \tau) = e_j(t+\tau) - e_j(t)$.

Function $f(\mathbf{r}, t)$ represents the acoustical pressure propagation [Eq. (4.4)]. Its representation using the Fourier spectral components is given by

$$f(x, t) = \frac{1}{v_a T} \sum_{n=-\infty}^{+\infty} \tilde{f}_0 \left(\frac{n}{v_a T} \right) \exp[-in(k_a x - \omega_a t)], \tag{4.15}$$

where $k_a = 2\pi/(v_a T)$ and $\omega_a = 2\pi/T$ are, respectively, the ultrasonic wave vector magnitude and the angular frequency associated with the period between ultrasonic pulses T. In Eq. (4.15), the Fourier transform $\tilde{f}_0(\nu)$ of the ultrasonic pulse shape function $f_0(x - v_a t)$ is

$$\tilde{f}_0(\nu) = \int_{-\infty}^{+\infty} f_0(u) \exp(i2\pi\nu u) du. \tag{4.16}$$

To obtain the expression for the displacement of the scatterers, we assume that at each ultrasonic frequency f in a spectrum of the infinite train of ultrasonic pulses,

the relation given by Eq. (4.1) is satisfied. For simplicity, we represent the variable $Y(f_r, \gamma)$ as a product $Y(f_r, \gamma) = S(f_r) \exp[i\phi(f_r)]$, where $S(f_r)$ is the amplitude and $\phi(f_r)$ is the phase of the scatterer velocity deviation from the fluid velocity. Then, the relation between the Fourier transforms of the scatterer velocity and the fluid velocity becomes

$$\tilde{v}(f) = \tilde{u}(f) S(f_r) \exp[i\phi(f_r)]. \tag{4.17}$$

In further derivations, we will denote with S_n and ϕ_n the values of $S(f_r)$ and $\phi(f_r)$ at ultrasound frequencies equal to $f_n = n/T$.

Using Eqs. (4.17) and (4.16), and assuming that the velocity of the fluid is given by $P(x,t)/(\rho v_a)$, we express the displacement of the jth scatterer as

$$e_j(t) = -\frac{iP_0}{2\pi\rho v_a^2} \sum_{\substack{n=-\infty \\ n\neq 0}}^{+\infty} \tilde{f}_0 \left(\frac{n}{v_a T} \right) \frac{S_n \exp(-i\phi_n)}{n} \exp[-in(k_a x_j - \omega_a t)]. \tag{4.18}$$

In Eq. (4.18), we assumed that no streaming is present in the fluid, so the spectral component associated with $n = 0$ (dc component) is excluded from the spectrum. Since the dc component is not playing any role in mechanism 2, it is also excluded from the solution for the phase term $\Delta\varphi_{s,n}$.

By combining Equations (4.13), (4.14), (4.15), and (4.18), we obtain expressions

for the values of the phase terms $\Delta\varphi_{s,n}$ and $\Delta\varphi_{s,d}$ for the train of ultrasound pulses

$$\Delta\varphi_{s,n} = i\frac{\Lambda}{4\pi}\sum_{\substack{n=-\infty\\ n\neq 0}}^{+\infty}\frac{\eta}{n}\tilde{f}_0\left(\frac{n}{v_aT}\right)\exp(in\omega_a t)[\exp(in\omega_a\tau)-1] \times\sum_{j=0}^{N}\frac{1}{\chi_{j+1}}[\exp(-ink_ax_{j+1})-\exp(-ink_ax_j)], \tag{4.19a}$$

$$\Delta\varphi_{s,d} = -i\frac{\Lambda}{4\pi}\sum_{\substack{n=-\infty\\ n\neq 0}}^{+\infty}\frac{S_n\exp(-i\phi_n)}{n}\tilde{f}_0\left(\frac{n}{v_aT}\right)\exp(in\omega_a t)[\exp(in\omega_a\tau)-1] \times\sum_{j=1}^{N}(\chi_j-\chi_{j+1})\exp(-ink_ax_j), \tag{4.19b}$$

where $\Lambda = 2n_0k_0P_0/(\rho v_a^2)$.

Since the phase increments associated with the different components of the optical path are correlated in general, it is not appropriate to use the approach of a Gaussian random variable for calculation of $\langle\exp(i\Delta\varphi_s)\rangle_{t,H}$. To simplify the task of averaging the autocorrelation function, we assume, like in the previous work,[18] that the total phase perturbation $\Delta\varphi_s$ due to the ultrasound is much less than one radian. In that case, it is sufficient to consider only the first two terms in the development of the exponential function from Eq. (4.11). The linear term $\langle\Delta\varphi_s\rangle_{t,H}$ in the development is zero for any pulse shape function $f_0(u)$, so, finally, we have

$$\langle\exp(i\Delta\varphi_s)\rangle_{t,H}\approx 1-\frac{1}{2}\left\langle\Delta\varphi_s^2\right\rangle_{t,H}. \tag{4.20}$$

Note that in the approximation of the small values of $\Delta\varphi_s$, we can approximate $\langle\exp(i\Delta\varphi_s)\rangle_{t,H}$ with $\exp(-\langle\Delta\varphi_s^2\rangle_{t,H}/2)$, but this expression cannot be used for estimation of the higher harmonics unless the phase increments are uncorrelated. This task could be accomplished, for example, by taking into account more terms in Eq. (4.20).

To obtain the expression for $\langle \Delta\varphi_s^2 \rangle_{t,H}$, we first split the whole term into three parts associated with the ultrasound induced optical index of refraction changes, with the displacements of the scatterers, and with the correlations between these two mechanisms:

$$\left\langle \Delta\varphi_s^2 \right\rangle_{t,H} = \left\langle \Delta\varphi_{s,n}^2 \right\rangle_{t,H} + \left\langle \Delta\varphi_{s,d}^2 \right\rangle_{t,H} + \left\langle 2\Delta\varphi_{s,n}\Delta\varphi_{s,d} \right\rangle_{t,H}. \tag{4.21}$$

Among the terms $\Delta\varphi_{s,d}^2$, $\Delta\varphi_{s,n}^2$, and $2\Delta\varphi_{s,d}\Delta\varphi_{s,n}$, after averaging over time, only those which contain products $\tilde{f}_0[n/(v_aT)]\tilde{f}_0[m/(v_aT)]$ where $n+m=0$ survive. As a result, we have

$$\begin{aligned}\langle \Delta\varphi_{s,n}^2 \rangle_t = & \left(\frac{\Lambda}{2\pi}\right)^2 \sum_{\substack{n=-\infty \\ n\neq 0}}^{+\infty} \sin^2\left(\frac{1}{2}n\omega_a\tau\right) \frac{\eta^2}{n^2} \left|\tilde{f}_0\left(\frac{n}{v_aT}\right)\right|^2 \\ & \times \sum_{j=0}^{N}\sum_{k=0}^{N} \frac{\exp(ink_ax_{k+1}) - \exp(ink_ax_k)}{\chi_{j+1}\chi_{k+1}} \\ & \times [\exp(-ink_ax_{j+1}) - \exp(-ink_ax_j)],\end{aligned} \tag{4.22a}$$

$$\begin{aligned}\langle \Delta\varphi_{s,d}^2 \rangle_t = & \left(\frac{\Lambda}{2\pi}\right)^2 \sum_{\substack{n=-\infty \\ n\neq 0}}^{+\infty} \sin^2\left(\frac{1}{2}n\omega_a\tau\right) \frac{S_n^2}{n^2} \left|\tilde{f}_0\left(\frac{n}{v_aT}\right)\right|^2 \\ & \times \sum_{j=1}^{N}\sum_{k=1}^{N} (\chi_j - \chi_{j+1})(\chi_k - \chi_{k+1}) \exp[ink_a(x_k - x_j)],\end{aligned} \tag{4.22b}$$

$$\begin{aligned}\langle 2\Delta\varphi_{s,d}\Delta\varphi_{N,n} \rangle_t = & -\left(\frac{\Lambda}{2\pi}\right)^2 \sum_{\substack{n=-\infty \\ n\neq 0}}^{+\infty} \sin^2\left(\frac{1}{2}n\omega_a\tau\right) \frac{\eta S_n \exp(i\phi_n)}{n^2} \left|\tilde{f}_0\left(\frac{n}{v_aT}\right)\right|^2 \\ & \times \sum_{j=0}^{N}\sum_{k=1}^{N} \frac{\chi_k - \chi_{k+1}}{\chi_{j+1}} \exp(ink_ax_k) \\ & \times [\exp(-ink_ax_{j+1}) - \exp(-ink_ax_j)].\end{aligned} \tag{4.22c}$$

For each frequency n/T, averaging over all free path lengths l_j between consec-

utive scatterers and averaging over all scattering angles χ_j can be done in the same way as in Ref.,[20] to obtain

$$\langle \Delta\varphi^2_{s,n}\rangle_{t,H} = \frac{\Lambda^2}{\pi^2}\sum_{n=1}^{+\infty}\sin^2\left(\frac{1}{2}n\omega_a\tau\right)\frac{\eta^2}{n^2}\left|\tilde{f}_0\left(\frac{n}{v_aT}\right)\right|^2 \times (k_anl)^2\mathrm{Re}\Big[(N+1)\hat{J}_n(\hat{I}-\hat{J}_n)^{-1}-(\hat{J}_n^2-\hat{J}_n^{N+3})(\hat{I}-\hat{J}_n)^{-2}\Big]_{0,0}, \tag{4.23a}$$

$$\langle \Delta\varphi^2_{s,d}\rangle_{t,H} = \frac{\Lambda^2}{\pi^2}\sum_{n=1}^{+\infty}\sin^2\left(\frac{1}{2}n\omega_a\tau\right)\frac{S_n^2}{n^2}\left|\tilde{f}_0\left(\frac{n}{v_aT}\right)\right|^2 \times\left[N\frac{1-g_1}{3}-\frac{(1-g_1)^2}{(k_anl)^2}[1-\mathrm{Re}(\hat{J}_n^{N-1})_{0,0}]\right], \tag{4.23b}$$

$$\langle 2\Delta\varphi_{s,d}\Delta\varphi_{N,n}\rangle_{t,H} = \frac{\Lambda^2}{\pi^2}\sum_{n=1}^{+\infty}\sin^2\left(\frac{1}{2}n\omega_a\tau\right)\frac{2\eta S_n\cos(\phi_n)}{n^2}\left|\tilde{f}_0\left(\frac{n}{v_aT}\right)\right|^2 \times(1-g_1)\left\{-N+\mathrm{Re}[\hat{J}_n(\hat{I}-\hat{J}_n^N)(\hat{I}-\hat{J}_n)^{-1}]_{0,0}\right\}. \tag{4.23c}$$

In Eq. (4.23), $\hat{I}$ is the identity matrix; the (i,j) element of the matrix $\hat{J}_n$ is defined as

$$[\hat{J}_n]_{(i,\,j)} = g_i^{1/2}g_j^{1/2}\sqrt{\frac{2i+1}{2}}\sqrt{\frac{2j+1}{2}}\int_{-1}^{1}T_n(x)P_i(x)P_j(x)dx, \tag{4.24}$$

where $T_n(x)=(1-ik_anlx)^{-1}$; $P_j(x)$ is the jth Legendre polynomial; $\mathrm{Re}[\,]_{0,\,0}$ represents the real part of the $(0,0)$ element of the matrix; and the g_m's are the coefficients in the phase function development from Eq. (4.10).

For a large number of scattering events N along the path of length s in diffusion regime, we can approximate Eq. (4.23) by replacing the N with its average value s/l.

We finally have

$$\left\langle \Delta\varphi_{s,n}^2 \right\rangle_{t,H} = \sum_{n=1}^{+\infty} \sin^2\left(\frac{n\pi\tau}{T}\right) C_n(n), \tag{4.25a}$$

$$\left\langle \Delta\varphi_{s,d}^2 \right\rangle_{t,H} = \sum_{n=1}^{+\infty} \sin^2\left(\frac{n\pi\tau}{T}\right) C_d(n), \tag{4.25b}$$

$$\langle 2\Delta\varphi_{s,n}\Delta\varphi_{s,d} \rangle_{t,H} = \sum_{n=1}^{+\infty} \sin^2\left(\frac{n\pi\tau}{T}\right) C_{n,d}(n), \tag{4.25c}$$

where the C terms, [$C_n(n)$, $C_d(n)$, and $C_{n,d}(n)$], represent the amplitudes of the average of the squares of the phase terms at each ultrasound frequency,

$$C_n(n) = \frac{\Lambda^2}{\pi^2}\left|\tilde{f}_0\left(\frac{n}{v_a T}\right)\right|^2 \frac{\eta^2}{n^2}(k_a n l)^2 \times \mathrm{Re}\left[\left(\frac{s}{l}+1\right)\hat{J}_n(\hat{I}-\hat{J}_n)^{-1} - \hat{J}_n{}^2(\hat{I}-\hat{J}_n{}^{s/l+1})(\hat{I}-\hat{J}_n)^{-2}\right]_{0,0}, \tag{4.26a}$$

$$C_d(n) = \frac{\Lambda^2}{\pi^2}\left|\tilde{f}_0\left(\frac{n}{v_a T}\right)\right|^2 \frac{S_n^2}{n^2}\left(\frac{s}{l}\frac{1-g_1}{3} - \frac{(1-g_1)^2}{(k_a n l)^2}\mathrm{Re}(\hat{I}-\hat{J}_n{}^{s/l-1})_{0,0}\right), \tag{4.26b}$$

$$C_{n,d}(n) = \frac{\Lambda^2}{\pi^2}\left|\tilde{f}_0\left(\frac{n}{v_a T}\right)\right|^2 \frac{2\eta S_n \cos(\phi_n)}{n^2} \times (1-g_1)\left(-\frac{s}{l} + \mathrm{Re}[\hat{J}_n(\hat{I}-\hat{J}_n{}^{s/l})(\hat{I}-\hat{J}_n)^{-1}]_{0,0}\right). \tag{4.26c}$$

It can be shown by numerical calculation that for a given path length s, the value of each C term in Eq. (4.26) is approximately independent from particular values of the optical mean free path l and anisotropy factor g_1, as long as the transport mean free path $l/(1-g_1)$ remains constant. This extends the conclusion about the similarity relation made in the case of large $k_a l$ values[20] to the case of small $k_a l$ values, too. For simplicity, in future analysis we will consider only isotropic scattering, noting that the anisotropic case can be approximately reduced to isotropic by replacing the l in the isotropic equations with the value of $l_{tr} = l/(1-g_1)$. Also, we will frequently refer to the transport mean free path when making observations about the $k_a l$ dependence of the C terms, although the mean free path will be used in

isotropic equations for simplicity. In the isotropic case, matrix $\hat{J}_n$ reduces to its $(0,0)$ element, $G_n = (nk_a l)^{-1}\arctan(nk_a l)$, and the values of the C terms become

$$C_n(n) = \frac{\Lambda^2}{\pi^2}\left|\tilde{f}_0\left(\frac{n}{v_a T}\right)\right|^2 \frac{\eta^2}{n^2}(k_a n l)^2\left[\left(\frac{s}{l}+1\right)\frac{G_n}{1-G_n} - \frac{G_n^2(1-G_n^{s/l+1})}{(1-G_n)^2}\right], \quad (4.27a)$$

$$C_d(n) = \frac{\Lambda^2}{\pi^2}\left|\tilde{f}_0\left(\frac{n}{v_a T}\right)\right|^2 \frac{S_n^2}{n^2}\left(\frac{s}{3l} - \frac{1-G_n^{s/l-1}}{(k_a n l)^2}\right), \quad (4.27b)$$

$$C_{n,d}(n) = \frac{\Lambda^2}{\pi^2}\left|\tilde{f}_0\left(\frac{n}{v_a T}\right)\right|^2 \frac{2\eta S_n \cos(\phi_n)}{n^2}\left(-\frac{s}{l} + \frac{G_n(1-G_n^{s/l})}{(1-G_n)}\right). \quad (4.27c)$$

4. Autocorrelation Function Dependence on Ultrasound Frequency

A broadband ultrasound pulse has energy spread over a wide range of ultrasonic frequencies. In this section, we present a more detailed analysis of the ultrasound frequency dependence of the ultrasound-modulated optical intensity in optically diffusive media.

We focus here on the single frequency component in a general solution obtained in Sec. 3. For conciseness, we look at the special case of the train of ultrasonic pulses when it represents an actual monochromatic plane ultrasound wave (CW). The CW case solution can be obtained from Eq. (4.27) if we first select the pulse shape function $f_0(u)$ to be equal to zero everywhere except in the interval $(-\pi/\hat{k}_a, \pi/\hat{k}_a)$, where it is equal to one sinusoidal cycle

$$f_0(u) = \begin{cases} \sin(\hat{k}_a u), & u \in (-\pi/\hat{k}_a, \pi/\hat{k}_a) \\ 0, & \text{elsewhere.} \end{cases} \quad (4.28)$$

Then, we take the limit $\hat{k}_a \to k_a$, where k_a is the magnitude of the ultrasonic wave vector associated with the period between ultrasonic pulses. In the limiting case,

the pressure propagation function, $f(x,t)$ defined in Eq. (4.4), is reduced to a pure sinusoidal function. The Fourier transform of $f_0(u)$ for discreet frequencies $\nu = n/(v_a T)$ and in a limiting case $\hat{k}_a \to k_a$, is zero for all n except when $n = 1$. For $n = 1$, we have $\tilde{f}_0[1/(v_a T)] = iv_a T/2$, and the set of Eqs. (4.27) simplifies to the solution for the CW case

$$\left\langle \Delta\varphi_{s,n}^2 \right\rangle_{t,H} = \sin^2\left(\frac{1}{2}\omega_a \tau\right) C_n, \tag{4.29a}$$

$$\left\langle \Delta\varphi_{s,d}^2 \right\rangle_{t,H} = \sin^2\left(\frac{1}{2}\omega_a \tau\right) C_d, \tag{4.29b}$$

$$\left\langle 2\Delta\varphi_{s,n}\Delta\varphi_{s,d} \right\rangle_{t,H} = \sin^2\left(\frac{1}{2}\omega_a \tau\right) C_{n,d}, \tag{4.29c}$$

where

$$C_n = \Lambda^2 \frac{\eta^2}{k_a^2}(k_a l)^2 \left[\left(\frac{s}{l}+1\right)\frac{G}{1-G} - \frac{G^2(1-G^{s/l+1})}{(1-G)^2}\right], \tag{4.30a}$$

$$C_d = \Lambda^2 \frac{S^2}{k_a^2}\left(\frac{s}{3l} - \frac{1-G^{s/l-1}}{(k_a l)^2}\right), \tag{4.30b}$$

$$C_{n,d} = \Lambda^2 \frac{2\eta S\cos(\phi)}{k_a^2}\left(-\frac{s}{l} + \frac{G(1-G^{s/l})}{1-G}\right). \tag{4.30c}$$

In Eq. (4.30), the subscript n is removed from G_n, S_n, and ϕ_n, since all of them are calculated at the same ultrasound frequency, i.e., when $n = 1$. These expressions are generalizations of the previously derived theory[18,20] to cases where the optical transport mean free path is smaller than the ultrasonic wavelength. Therefore, in Eq. (4.30), not only the parts that are linear with s/l are presented, but, also, the terms that are a result of strong correlation among the optical phase increments due to the different scattering events and among the optical phase increments due to the different optical free paths between consecutive scatterers. Another important difference is that we have significant correlation between the phase increments due to mechanism 1 and mechanism 2, unless the cosines of the phase lag between the

ultrasound induced movement of the scatterers and the fluid is exactly zero. This correlation is represented in the mixed term given by Eq. (4.29c), and it is not zero even for large values of the $k_a l$ product when the correlations vanish between phase increments due to only mechanism 1 or only mechanism 2. This result can be explained in the following way: at each scatterer position, the phase increment that is due to displacement can be approximated as a sum of the two terms associated with the incoming and outgoing scattering directions. Each free path between two consecutive scatterers is associated with two such displacement terms. The phase of the sum of these two displacement terms differs from the phase of the index of refraction term associated with the corresponding free path by exactly $\pi + \phi$, where ϕ is the phase lag between the fluid and the scatterer movement. Therefore, the product of these terms is negative, and its average is not zero unless $\cos(\phi) = 0$. The strength of the correlation is proportional to the $\cos(\phi)$, as can be seen from Eq. (4.30c). For smaller $k_a l$ values, when the length of the ultrasound wave increases in respect to the optical transport mean free path, correlations also appear between the optical phase increments associated with several consecutive displacement and index of refraction terms.

Figure 4.1 presents the ultrasound frequency dependence of C terms in Eq. (4.30) for several values of the average number of scattering events s/l along the optical path. The values of the C terms at $s/l = 10$ are presented for completeness, although the applied approximations may not be valid for such a small average number of scattering events along the optical path. The parameters used in the calculation are optical mean free path $l = 1$ mm; elasto-optic coefficient of water at room temperature $\eta = 0.32$; $\Lambda = 1$ m^{-1}; and it is assumed that the scatterers are exactly following the fluid displacement ($S = 1$, $\phi = 0$). The term $C_{n,d}$ is multiplied by -1 to be presented on the same graph with the other two terms, although its value is

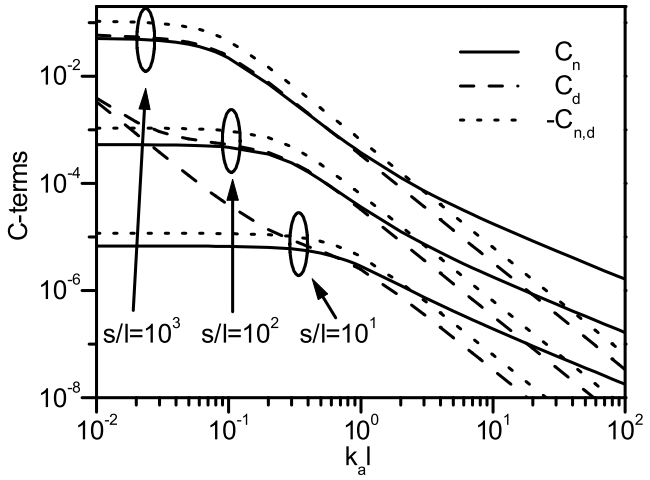

Fig. 4.1. Dependence of the C terms on the ultrasound frequency. Index of refraction term C_n, displacement of the scatterers term C_d, and mixed term $C_{n,d}$ multiplied by -1, are presented for three different s/l values. The values of the parameters used are $l = 1$ mm, $\Lambda = 1$ m^{-1}, $\eta = 0.32$, $S = 1$, and $\phi = 0$.

negative and it actually cancels out, to some extent, the phase accumulations due to the individual contributions of the two mechanisms of modulation. It is important to notice that each C term in Eq. (4.30) is not an explicit function of only the $k_a l$ product, regardless of the specific values of k_a and l. However, the ratio between each two C terms in Eq. (4.30) for a given s/l ratio depends only on the $k_a l$ product, up to a multiplication constant which depends on η, S, and $\cos(\phi)$.

The index of refraction term C_n, and the displacement term C_d have quite different behaviors at the opposite ends of the $k_a l$ range, as can be seen from Fig. 4.1. When the ultrasound pressure amplitude is constant, except for some intermediate interval of the $k_a l$ values, C_d is proportional to the square of the scatterer displacement amplitude (i.e. inversely proportional to the square of the ultrasound frequency). When the $k_a l$ product is small, scatterers along the optical path occupy a space volume where the ultrasound phase is nearly the same, unless the value of s/l

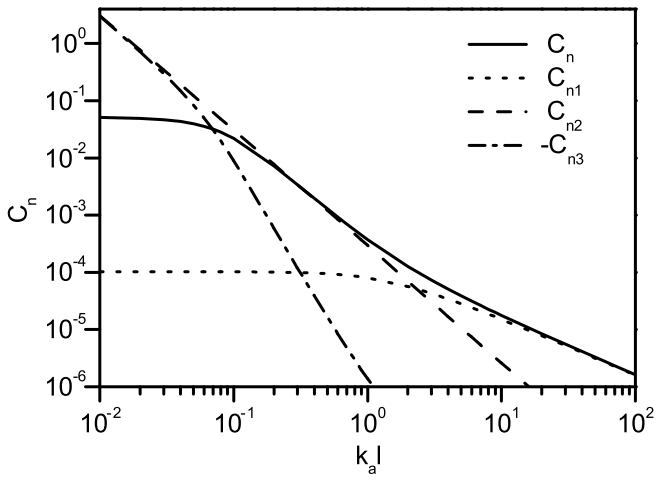

Fig. 4.2. Dependence of the components of the C_n term on the ultrasound frequency, for $s/l = 10^3$. The values of the parameters used are: $l = 1$ mm, $\Lambda = 1$ m^{-1}, $\eta = 0.32$, $S = 1$, and $\phi = 0$.

is very large. The C_d term in that region depends very little on l and s. When the scatterers are within the same ultrasound phase, we have a cancelation of the optical phase increments due to mechanism 1 which share the same free path between consecutive scatterers. Then, only increments from the first incoming direction χ_1, and the last outgoing direction χ_{N+1} contribute to C_d, and it behaves as if it was caused by only one scatterer. In contrary, if we choose the source and detector positions to move with the ultrasound, then, we essentially have cancelation between all of the displacement contributions in the limit of low $k_a l$ values. On the other side of the $k_a l$ range, when the optical transport mean free path is greater than the ultrasound wavelength, the phase increments between different scattering events are uncorrelated. In that region, the C_d term is equal to the sum of the individual scattering contributions, which are all proportional to k_a^{-2}.

The behavior of the C_n term is particularly interesting since the correlations between the phase increments from different free paths are present for much higher

ultrasound frequencies than in the case of the C_d term. Figure 4.2 presents the C_n dependence on the ultrasound frequency for $(s/l) = 10^3$. We present the C_n as a sum of three terms, $C_{n1} + C_{n2} + C_{n3}$, which are given by

$$C_{n1} = \Lambda^2 \frac{\eta^2}{k_a^2} (k_a l)^2 \left[\left(\frac{s}{l} + 1 \right) G \right], \tag{4.31a}$$

$$C_{n2} = \Lambda^2 \frac{\eta^2}{k_a^2} (k_a l)^2 \left[\left(\frac{s}{l} + 1 \right) \frac{G^2}{1-G} \right], \tag{4.31b}$$

$$C_{n3} = \Lambda^2 \frac{\eta^2}{k_a^2} (k_a l)^2 \left[-\frac{G^2(1-G^{s/l+1})}{(1-G)^2} \right]. \tag{4.31c}$$

The first two terms C_{n1} and C_{n2} were derived previously[18,20] for the case where the $k_a l$ values were large enough that we could neglect the terms which were not linearly proportional to s/l. The term C_{n1} (dotted line in Fig. 4.2) is the result of averaging the individual squares of the phase accumulations along the free paths. It is proportional to the average number of free paths $s/l + 1$, and it has a transition from a weak dependence on $k_a l$ (in a low $k_a l$ region) to $(k_a l)^{-1}$ dependence for large $k_a l$. The term C_{n2} (dashed line in Fig. 4.2) is proportional to $s/l + 1$, and it is a part of the result of averaging the products between the phase accumulations along the different free paths. This term has approximately $(k_a l)^{-2}$ dependence. Finally, term C_{n3} is nonlinear with the s/l part of the result of averaging the products between the phase accumulations along the different free paths. It is a result of strong correlation between the phase accumulations along the different free paths for low $k_a l$ values. It has a negative value, so the dashed-dotted line in Fig. 4.2 presents the $k_a l$ dependence of $-C_{n3}$. The term C_{n1} eventually dominates all of the other contributions to C_n when $k_a l$ is sufficiently large, suggesting that the optical phase increments from the different free paths that are due to mechanism 2 are completely uncorrelated. For the lower $k_a l$ values, the correlations between the phase accumulations along the different free paths begin to dominate in the C_n term – first through term C_{n2} which

is proportional to s/l , and then combined with the C_{n3}. When $k_a l$ is low enough that all of the scatterers occupy space with the similar ultrasound phase, then the increments from the different free paths add constructively. The C_n term in that limit becomes less dependent on k_a and l and more dependent on the square of the total path length s^2.

Finally, in a case of $C_{n,d}$, when $k_a l$ is sufficiently large, we also have an absence of correlation between the phase increments due to mechanisms 1 and 2 for the components of the optical path that do not share the same free path. However, as described earlier, the correlation between the phase increments due to mechanisms 1 and 2 for the same free path between two consecutive scatterers is always present, unless the cosines of the phase lag between the ultrasound induced movement of the scatterers and the fluid is exactly zero.

It is interesting to compare the intensities of the first sidebands of the acousto-optically modulated light when it propagates the same length L in optically clear and optically turbid media. In particular, with the optically clear media, we assume that the light and the ultrasound are traveling along the x and z directions, respectively, and that conditions for the Raman-Nath diffraction are satisfied. In a formal Raman-Nath approach,[44] the phase of the electrical field accumulated along the interaction length L is equal to

$$\varphi(t) = k_0 n_0 L \left[1 + \frac{1}{2} M \cos(\omega_a t - k_a z)\right]. \tag{4.32}$$

In Eq. (4.32), $\omega_a = 2\pi f_a$, where f_a is the ultrasound frequency, and $M = 2\eta P_0/(\rho v_a^2)$ is, like in Eq. (4.7), related to the optical index of refraction change that is due to the ultrasound. We proceed with developing the electrical field in analytic signal representation, using Bessel functions and calculating the autocorrelation function $< E(t+\tau)E^*(t) >_t$. It is assumed that the amplitude of the electrical field is unity

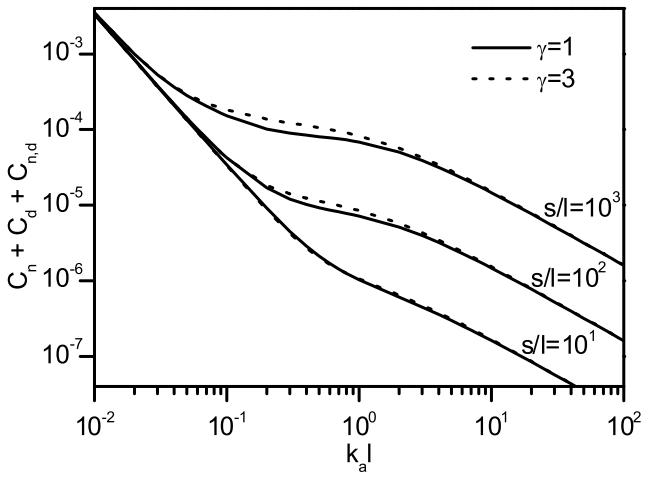

Fig. 4.3. Ultrasound frequency dependence of the sum of the C terms, for two different values of the mass density ratio γ. Values of the parameters are: scatterer radius $a_0 = 1$ μm, optical mean free path $l = 1$ mm, kinematic viscosity of water $\eta_k = 10^{-6}$ m^{2}s^{-1}, elasto-optic coefficient of water $\eta = 0.32$, and $\Lambda = 1$ m^{-1}.

and that the phase disturbance is small enough that the Bessel functions can be approximated with the linear and quadratic terms. If we limit the solution to only the first harmonics, the expression for the power spectral density $\mathcal{P}(\nu)$ is

$$\mathcal{P}(f) = \left(1 - \frac{C_{\mathrm{RN}}}{4}\right)\delta(f - f_0) + \frac{C_{\mathrm{RN}}}{8}\,\delta(f - f_0 + f_a) + \frac{C_{\mathrm{RN}}}{8}\,\delta(f - f_0 - f_a). \quad (4.33)$$

In Eq. (4.33), f_0 is the frequency of unmodulated light; $\delta(\,)$ is the Dirac delta function; and the parameter C_{RN} is equal to $\Lambda^2 L^2 \eta^2/2$.

In the optically multiple scattering regime described in Eq. (4.29), based on Eqs. (4.11) and (4.20), the power spectral density for the path of length L is given by the same type of equation as Eq. (4.33), where parameter C_{RN} is replaced with the sum $C = C_n + C_d + C_{n,d}$ and pathlength L is substituted for s. For low $k_a l$ values, C_d is the dominant term in the sum. In that range of $k_a l$ values, $G \approx 1 - (k_a l)^2/3$, and, consequently, $C_d \approx \Lambda^2 S^2/(3k_a^2)$. This result implies that the C_d term behaves like a

displacement contribution from a single scatterer. It is, therefore, dependent on k_a^{-2}, and only slightly dependent on path length L. In the same regime of low $k_a l$ values, $C_n \approx C_{\mathrm{RN}}$. This is in agreement with the fact that in the limit of low $k_a l$ values, all of the scatterers are within a space with almost the same phase of the ultrasound field, and the contributions from mechanism 2 add constructively, regardless of different scattering directions. On the contrary, when $k_a l$ is large, the values of the C terms are significantly lower than C_{RN} due to the increased cancelation of the phase increments. In that regime, $G \approx \pi/(2k_a l)$ and all of the C terms are well described with their parts linearly proportional to s/l. The C_n term is then proportional to k_a^{-1}, and it is lower than C_{RN} by a ratio of s/λ_a, where λ_a is the ultrasound wavelength. Compared to the C_n term, the C_d and $C_{n,d}$ terms are lower by another l/λ_a ratio, discarding the parameters η, S, and $\cos(\phi)$ involved in their expressions. Both parameters depend on k_a^{-2}, and their contribution to the sum C is not important compared to C_n.

Finally, we plot in Fig. 4.3 the ultrasonic frequency dependence of the sum C of the optical phase accumulation terms, C_n, C_d, and $C_{n,d}$, for two different relative mass densities of the optical scatterers ($\gamma = 1$ and $\gamma = 3$) and three different values of s/l. We choose the mean optical scattering free path to be $l = 1$ mm and the radius of the optical scatterers as $a_0 = 1$ μm. For this set of chosen parameters, in the range of the small $k_a l$ values, the particles are following the fluid displacement in amplitude and phase ($S \approx 1$ and $\phi \approx 0$), and there is no noticeable difference between the values of the C term for the different γ values. With a large $k_a l$, the C term follows the behavior of the index of refraction term C_n, and the influence of the C_d term is small. Therefore, only in the range of intermediate $k_a l$ values, where both a phase and an amplitude difference between the scatterers and fluid motion exist (for $\gamma = 3$), and where the C_d term contributes significantly to the value of C, does a discrepancy appear between the values of the C term for different γ values. We

expect that γ is just slightly different from unity in most situations in real biological soft tissues, in which case the observed discrepancy is not significant.

We mentioned earlier that when $k_a l$ is large, the C term is dominated by the value of the index of refraction term C_n, and it is dependent on the k_a^{-1}. Interestingly, when $k_a l$ is small, the value of the elasto-optic coefficient η in water is such that a large cancelation occurs when summing the C terms, due to the negative value of $C_{n,d}$. As a result, in a low $k_a l$ limit, the C term behaves like the C_d term at low values of s/l, i.e., as if it is caused by the displacement contribution of only one scatterer.

Note that the value of the Λ parameter is proportional to the acoustic pressure amplitude P_0, and, consequently, the modulated intensity has a P_0^2 dependence. From Fig. 4.3, in the CW regime, when $k_a l$ is small, pressure amplitude values as low as $P_0 = 1$ kPa are sufficient to produce values of the C term that are close to unity, which is at the edge of acceptance for our theory based on the small phase approximation. When propagating ultrasound pulses, we can apply significantly higher peak ultrasound pressures without violating the assumption of small phase increments.

5. Transmission and Reflection of the Ultrasound-modulated Light Intensity in a Slab Geometry

In this section, we present the analytical expression for an acousto-optical signal produced by a train of ultrasound pulses in the case of an infinitely wide optically scattering slab. Since it is possible to find a reasonably good analytical expression for the pathlength probability density function for both transmission and reflection slab

geometry, a slab has been considered previously for various problems.[4–6,18,19,26,27] We choose the Z axis of the coordinate system to be perpendicular to the infinitely wide slab of thickness d. The indices of refraction of both the surrounding and scattering media are n_0. A plane ultrasonic wave propagates within the slab (in the $X-Y$ plane) and is assumed to fill the whole slab. We consider two cases. In the first case, which we will refer to as the transmission case, one side of the slab is irradiated by a plane electromagnetic wave, and a point detector measures the optical intensity on the side of the slab opposite to the light source. By solving the diffusion equation for this geometry, it is possible to find an expression[18,26,27] for the photon pathlength probability density function $p(s)$. For the transmission case, we follow the derivation of $p(s)$ from[18,26] by applying an infinite number of image sources and introducing extrapolated-boundary conditions.[26,27] We assume isotropic scattering, in which case, $\mu_s^{'} = \mu_s$. By virtue of the similarity relation described in Sec. 3, we can extend the conclusions obtained from the isotropic case to anisotropic scattering also. The final expression for the probability density function $p_T(s)$ for the path of length s in the transmission geometry is

$$\begin{aligned} p_T(s) &= K_T(s)\sum_{n=1}^{+\infty}\left[[(2n-1)d_0 - z_0]\exp\left(-\frac{[(2n-1)d_0 - z_0]^2}{4Ds}\right)\right. \\ &\quad \left. -[(2n-1)d_0 + z_0]\exp\left(-\frac{[(2n-1)d_0 + z_0]^2}{4Ds}\right)\right], \end{aligned} \tag{4.34}$$

where

$$K_T(s) = \frac{\sinh(d_0\sqrt{\mu_a/D})}{\sinh(z_0\sqrt{\mu_a/D})}s^{-3/2}\exp(-\mu_a s)(4\pi D)^{-1/2}. \tag{4.35}$$

In Eq. (4.34), the diffusion constant is given by $D = [3(\mu_a + \mu_s)]^{-1}$; d_0 is the distance between the two extrapolated boundaries of the slab; and z_0 is the location of the converted isotropic source from the extrapolated incident boundary of the slab. The distance between the extrapolated boundary and the corresponding real boundary of

the slab is $l\gamma^*$, where $\gamma^* = 0.7104$ and l is the scattering mean free path ($l = 1/\mu_s$). The converted isotropic source is one isotropic scattering mean free path into the slab. Therefore, $d_0 = d + 2l\gamma^*$, and $z_0 = l(1 + \gamma^*)$.

In the second (reflection) case, the point detector and the point source of light are positioned on the same side of the slab, and separated from each other by a distance ρ in the $X - Y$ plane. We also assume in this case that the slab is infinitely thick. Similarly to the transmission case, we obtain the solution for the pathlength probability density function $p_R(s)$ in the reflection geometry,

$$\begin{aligned} p_R(s) &= \frac{2\pi^{-1/2}\left[(z_0^2+\rho^2)/(4D)\right]^{3/2}}{\left[1+2\sqrt{\mu_a(z_0^2+\rho^2)/(4D)}\right]} \exp\left(2\sqrt{\frac{\mu_a(z_0^2+\rho^2)}{4D}}\right) \\ &\quad \times s^{-5/2}\exp(-\mu_a s)\exp\left(-\frac{\rho^2+z_0^2}{4Ds}\right). \end{aligned} \tag{4.36}$$

The following expressions are needed in order to perform averaging of the terms in Eq. (4.26) over the pathlength probabilities:

$$\begin{aligned} T_s &= \int_0^{+\infty} p_T(s)\ s\ ds, \\ R_s &= \int_0^{+\infty} p_R(s)\ s\ ds, \\ T_{\exp,n} &= \int_0^{+\infty} p_T(s)\exp(-Q_n s)ds, \\ R_{\exp,n} &= \int_0^{+\infty} p_R(s)\exp(-Q_n s)ds, \end{aligned} \tag{4.37}$$

where $Q_n = -\ln(G_n)/l$. After calculating the integrals in Eq. (4.37), we have

$$\begin{aligned} T_s &= \frac{d_0 \coth(d_0\sqrt{\mu_a/D}) - z_0 \coth(z_0\sqrt{\mu_a/D})}{2\sqrt{\mu_a D}}, \\ R_s &= \frac{\rho^2 + z_0^2}{2D[1+\sqrt{\mu_a(\rho^2+z_0^2)/D}]}, \\ T_{\mathrm{exp},n} &= \frac{\sinh(d_0\sqrt{\mu_a/D})}{\sinh(z_0\sqrt{\mu_a/D})} \times \frac{\sinh[z_0\sqrt{(\mu_a+Q_n)/D}]}{\sinh[d_0\sqrt{(\mu_a+Q_n)/D}]}, \\ R_{\mathrm{exp},n} &= \frac{1+\sqrt{(\mu_a+Q_n)(\rho^2+z_0^2)/D}}{1+\sqrt{\mu_a(\rho^2+z_0^2)/D}} \times \frac{\exp[-\sqrt{(\mu_a+Q_n)(\rho^2+z_0^2)/D}]}{\exp[-\sqrt{\mu_a(\rho^2+z_0^2)/D}]}. \end{aligned} \tag{4.38}$$

If we denote with $\langle C_n(n)\rangle_{s,T}$, $\langle C_d(n)\rangle_{s,T}$, and $\langle C_{n,d}(n)\rangle_{s,T}$ the averages of the appropriate C terms in Eq. (4.26) over all of the pathlengths in the transmission geometry, we have, with the help of Eq. (4.38),

$$\langle C_n(n)\rangle_{s,T} = \frac{\Lambda^2}{\pi^2}\left|\tilde{f}_0\left(\frac{n}{v_a T}\right)\right|^2 \frac{(k_a n l \eta)^2}{n^2}\left[\frac{G_n(1+T_s/l)}{1-G_n} - \frac{G_n^2(1-G_n T_{\mathrm{exp},n})}{(1-G_n)^2}\right], \tag{4.39a}$$

$$\langle C_d(n)\rangle_{s,T} = \frac{\Lambda^2}{\pi^2}\left|\tilde{f}_0\left(\frac{n}{v_a T}\right)\right|^2 \frac{S_n^2}{n^2}\left(\frac{T_s}{3l} - \frac{1-G_n^{-1}T_{\mathrm{exp},n}}{(k_a n l)^2}\right), \tag{4.39b}$$

$$\langle C_{n,d}(n)\rangle_{s,T} = \frac{\Lambda^2}{\pi^2}\left|\tilde{f}_0\left(\frac{n}{v_a T}\right)\right|^2 \frac{2\eta S_n \cos(\phi_n)}{n^2}\left(-\frac{T_s}{l} + \frac{G_n(1-T_{\mathrm{exp},n})}{1-G_n}\right). \tag{4.39c}$$

The expressions for the terms $\langle C_n(n)\rangle_{s,R}$, $\langle C_d(n)\rangle_{s,R}$, and $\langle C_{n,d}(n)\rangle_{s,R}$ averaged in the reflection configuration are identical with the expressions in Eq. (4.39), with T_s and $T_{\mathrm{exp},n}$ replaced with R_s and $R_{\mathrm{exp},n}$, respectively.

6. Various Pulse Shapes

We present the effects of acousto-optical modulation for two distinct types of the ultrasound pulse shapes. The Gaussian pulse shape (pulse 1) is used as a representative of a pulse with the spectrum centered at the zero frequency. Although just an idealization of the ultrasonic pulse generated in realistic conditions, this is a useful

example of acousto-optically modulated light dependence on ultrasound frequency. The second pulse shape function (pulse 2) is produced by modulating the Pulse 1 profile with the cosines function, and it is a more realistic example of commonly generated ultrasound pulses. Figure 4.4(a) presents the time profiles of the pulse shape functions, whose expressions are

$$f_{0,P1}(u) = \exp\left(-\frac{u^2}{2(\sigma v_a T)^2}\right), \tag{4.40a}$$

$$f_{0,P2}(u) = \exp\left(-\frac{u^2}{2(\sigma v_a T)^2}\right)\cos(k_u u). \tag{4.40b}$$

In Eqs. (4.40), $v_a = 1480$ ms^{-1} is the ultrasound velocity in water; $T = 20$ μs is the time period between pulses; and $\sigma = 2.5\times10^{-3}$ is the constant which controls the relative width of each pulse compared to the distance between consecutive pulses, such that both pulses have similar bandwidths ≈ 5.3 MHz. In Pulse 2, k_u is the magnitude of the ultrasound wave vector associated with the 8 MHz central frequency.

Figures 4.4(c) and 4.4(d) present the squares of the Fourier transforms of the ultrasound pulse profiles $f_{0,P1}(u)$ and $f_{0,P2}(u)$, for different ultrasound frequencies n/T, respectively,

$$\tilde{f}_{0,P1}\left(\frac{n}{v_a T}\right) = \sigma v_a T\sqrt{2\pi}\exp[-2n^2(\sigma\pi)^2], \tag{4.41a}$$

$$\tilde{f}_{0,P2}\left(\frac{n}{v_a T}\right) = \sigma v_a T\sqrt{2\pi}\exp[-2n^2(\sigma\pi)^2] \times \exp\left[-2\left(\sigma\pi\frac{T}{T_u}\right)^2\right]\cosh\left(4n(\sigma\pi)^2\frac{T}{T_u}\right). \tag{4.41b}$$

In calculating the acousto-optical effect, we use the optical wavelength $\lambda_0 = 0.5$ μm, the optical index of refraction $n_0 = 1.33$, and the elasto-optic coefficient in water $\eta = 0.32$. We also use the scattering mean free path $l = 1$ mm, and the optical absorption coefficient $\mu_a = 1$ cm^{-1}, which are in agreement with the typical

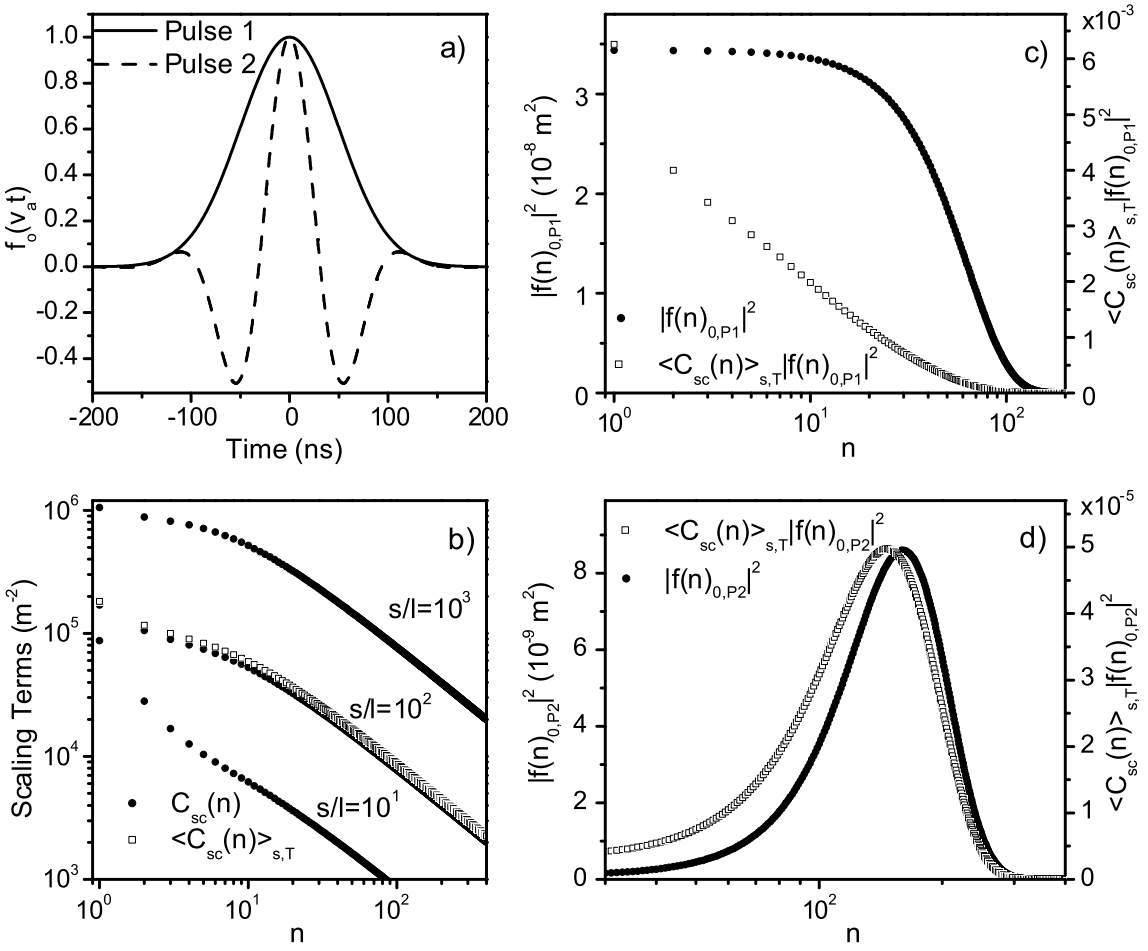

Fig. 4.4. Power spectrum of the light modulated by the ultrasound pulses 1 and 2. (a) Pulse time dependence; (b) ultrasound frequency dependence of the scaling terms; (c) power spectrum of the pulse 1 before and after multiplication with the scaling term; (d) power spectrum of the pulse 1 before and after multiplication with the scaling term; parameters used in calculation are index of refraction in water $n_0 = 1.33$; optical wavelength $\lambda_0 = 0.5$ μm; ultrasonic pressure amplitude $P_0 = 10^5$ Pa; speed of sound in water $v_a = 1480$ ms^{-1}; scattering mean free path $l = 1$ mm; elasto-optic coefficient $\eta = 0.32$; relative scatterer density $\gamma = 1$; period between consecutive pulses $T = 20$ μs; pulse 2 central ultrasound frequency $T_u^{-1} = 8$ MHz; $\sigma = 2.5 \times 10^{-3}$.

optical transport mean free path and absorption coefficient in soft tissue. Since it is expected that in reality scatterers closely follow the ultrasound induced fluid motion, we use a relative scatterer density γ equal to one. For equal values of the scattering slab thickness in transmission geometry $d = 4$ cm, and the distance between the source and the detector in reflection geometry $\rho = 4$ cm, and for the particular values of the other parameters used, the probability of the path length is almost equal for both the transmission and reflection configurations. Therefore, we present only the transmission case results. We use an ultrasonic pressure amplitude P_0 equal to 10^5 Pa, which is much higher than the allowed CW ultrasound pressure amplitude used in the approximation of small ultrasound modulation. The parameters are also chosen such that the larger ultrasound wavelength in a spectrum is comparable with the slab thickness (or the source-detector distance), and the approximations involved in Eq. (4.8) are satisfied.

We define in transmission geometry the scaling coefficient $C_{sc}(n)$, and the total scaling coefficient $\langle C_{sc}(n)\rangle_{s,T}$, at each ultrasound frequency n/T as

$$C_{sc}(n)\left|\tilde{f}\left(\frac{n}{v_a T}\right)\right|^2 = C_n(n) + C_d(n) + C_{n,d}(n), \tag{4.42a}$$

$$\langle C_{sc}(n)\rangle_{s,T}\left|\tilde{f}\left(\frac{n}{v_a T}\right)\right|^2 = \langle C_n(n)\rangle_{s,T} + \langle C_d(n)\rangle_{s,T} + \langle C_{n,d}(n)\rangle_{s,T}. \tag{4.42b}$$

Based on Eq. (4.27), the scaling coefficient $C_{sc}(n)$ scales the power spectral density of the ultrasound pulse train for each particular value of the optical pathlength s. The black squares on Fig. 4.4(b) present the value of $C_{sc}(n)$ for the different ultrasound frequencies and for three different values of s. The scaling coefficient $C_{sc}(n)$ behaves similarly to the sum of the C terms in the CW case (Sec. 4). The open squares in Fig. 4.4(b) present the frequency dependence of the total scaling coefficient $\langle C_{sc}(n)\rangle_{s,T}$, which is the result of path length averaging of the scaling co-

efficient $C_{sc}(n)$. At each ultrasound frequency, the power spectrum of the ultrasound-modulated intensity is obtained by scaling the power spectrum of the train of pulses with this coefficient. The $\langle C_{sc}(n)\rangle_{s,T}$ behaves similarly to some $C_{sc}(n)$ term at the average value of the pathlength s. In a high frequency range, it is inversely proportional to the ultrasonic frequency, and in a low frequency range, depending on the average pathlength value, it might become inversely proportional to the ultrasound frequency squared.

The open squares in Figs. 4.4(c) and 4.4(d) present the ultrasound frequency dependence of the power spectrum of the modulated light, given by $|\tilde{f}[n/(v_a T)]|^2 \times\langle C_{sc}(n)\rangle_{s,T}$, in transmission geometry for the pulse 1 and pulse 2 cases, respectively. Compared with the power spectra of the pulse shape functions (black circles), both pulses are more attenuated at the higher ultrasound frequencies due to the decay of the total scaling coefficient $\langle C_{sc}(n)\rangle_{s,T}$. Pulse 1 is attenuated strongly at higher frequencies, and it suffers a large reduction in bandwidth. The present theoretical model is not valid for very low values of the $k_a l$ product, and the concept of infinite train of pulses allows us to avoid this part of the spectrum even in a case where the single pulse shape function has very low frequency components, as in the pulse 1 case. Consequently, based on this model, it is difficult to predict the spectrum of the optical intensity after interaction with only one pulse with a similar shape. However, based on the presented theoretical derivations, it looks reasonable to us to expect a large bandwidth reduction for a pulse with a spectrum centered at zero frequency. In the case of pulse 2, due to the frequency dependence of the total scaling coefficient, the frequency spectrum of the ultrasound-modulated light is slightly broadened for ≈ 0.3 MHz, and the central frequency is left-shifted by 0.7 MHz. Note, also, that the value of the total scaling coefficient $\langle C_{sc}(n)\rangle_{s,T}$ at the central frequency of pulse 2 is several times smaller than its value at the lowest frequency in the spectrum.

7. Conclusion

In conclusion, we have presented an extension of the theory of ultrasound modulation of multiply scattered diffused light toward the small $k_a l$ values, where a strong correlation exists between the ultrasound induced optical phase increments associated with different components of the optical path. It is shown that an approximate similarity relation is valid for this extended range of $k_a l$ values. For large $k_a l$ values, an inverse linear dependence of the modulated signal on the ultrasound frequency is a consequence of the dominating effect of mechanism 2, while in the low $k_a l$ range, depending on the particular values of the average number of scattering events along the pathlength, the signal has a tendency to be even inversely proportional to the square of the ultrasound frequency. The theory is also extended to account for complex scatterer movement in respect to surrounding fluid displacement. It is expected that in cases involving the commonly used ultrasound pressures in medicine, the movement of the optical scatterers in soft biological tissues should not differ significantly from the movement of the surrounding tissue. In this situation, even for large values of the $k_a l$ product, a significant correlation between the contributions of mechanism 1 and 2 exists. Finally, we derived an analytical solution for ultrasound modulation of light when the train of the ultrasound pulses traverses the scattering media. Examples of two characteristic pulse shapes with zero and nonzero central frequencies are presented in the transmission and reflection geometries. It is shown that the ultrasound frequency dependence of the optical phase variations due to mechanisms 1 and 2 produces a nonuniform deviation of the pulse spectra, as well as decay of the modulated light power in the higher ultrasound frequency ranges.

CHAPTER V
CORRELATION TRANSFER EQUATION FOR ULTRASOUND-MODULATED MULTIPLY SCATTERED LIGHT

1. Introduction

Since the existing theoretical model[18,20,45] is based on the diffusing-wave spectroscopy (DWS) approach,[5,6] applications are limited to simple geometries where it is possible to approximate the ultrasound field with a plane ultrasound wave and where the probability density function of the optical path length between the source and detector is analytically known. As a result, only transmission through,[18,20,45] and reflection from,[43,45] an infinite scattering slab filled with ultrasound, have been analytically studied. In most experiments, however, the optical parameters are heterogeneously distributed and a focused ultrasound beam is used. Therefore, a more general theoretical model, which can locally treat interactions between ultrasound and light in an optically scattering medium, is needed.

In this chapter, based on the ladder diagram approximation of the Bethe-Salpeter equation,[46] we have derived a temporal correlation transfer equation (CTE) for ultrasound-modulated multiply scattered light. The work of the many authors who established the link between multiple scattering theory and the radiative transfer equation in the last sixty years is reviewed in several excellent articles.[27,47–51] Also, several authors have considered the development of the CTE for scatterers moving with a given velocity distribution or undergoing Brownian motion.[52–55] In our case, both the ultrasound-induced movement of the scatterers and the ultrasound-induced change in the optical index of refraction have led to a new form of CTE.

The derivation of the CTE was performed in several steps. In Section 2, we first develop an expression for the electric field Green's function in the presence of an ultrasound field in a medium free of optical scatterers. Next, we solve the Dyson equation[46] and obtain the value of a mean Green's function in the presence of optical scatterers, which can be used to obtain the ensemble averaged field for a given distribution of optical sources. Finally, in Sec. 3, based on the Bethe-Salpeter equation, we write the expression for a mutual coherence function of the electric field and transform it into an integral form of the CTE. Consequently, we derive a differential form of the CTE. In Section 4, based on the CTE, we develop a Monte Carlo algorithm. We further calculate the three dimensional distribution of the power spectrum of the ultrasound-modulated light, produced by 1-MHz focused ultrasound in an optically scattering slab with optical parameters representative of those in soft biological tissues at visible and near infrared wavelengths.

2. Development of the Mean Green's Function

We start by presenting an approximate expression for the Green's function of the electric field component in a medium free from optical scatterers in the presence of an ultrasound field. We assume that the dielectric constant of the medium (ϵ) experiences small perturbations due to the ultrasound field and that it is well approximated with $\epsilon = \epsilon_0[1+2\eta P(\mathbf{r},t)/(\rho v_a^2)]$, where ϵ_0 is the dielectric constant of the unperturbed medium; $P(\mathbf{r},t)$ is the ultrasound pressure; ρ is the mass density of the medium; v_a is the ultrasound speed; and η is the elasto-optical coefficient (in water at standard conditions $v_a \approx 1480$ ms^{-1}; and $\eta \approx 0.32$). Consequently, we locally approximate the optical index of refraction with $n(\mathbf{r},t) = n_0[1 + \eta P(\mathbf{r},t)/(\rho v_a^2)]$, where $n_0 = \sqrt{\epsilon_0}$.

Let $F(\mathbf{r})$ be the spatial distribution of a monochromatic light source having angular frequency ω_0 and wave-vector magnitude $k_0 = \omega_0/c_0$, where c_0 is the speed of light in vacuum. To simplify the derivations, we neglect the optical polarization effects and consider only one component $\tilde{E}(\mathbf{r}, t)$ of the electric field. The time retardation is also neglected, since the time during which the light propagates through the sample is a small fraction of the ultrasound period. Due to the large ratio between the optical and ultrasound temporal frequencies, we approximate the quasi-monochromatic electric field in the medium as $\tilde{E}(\mathbf{r}, t) = E(\mathbf{r}, t)\exp(-i\omega_0 t)$, where $E(\mathbf{r}, t)$ is a slowly changing function of time that satisfies the following equation

$$\left[\nabla^2 + k_0^2 n_0^2 \left(1 + 2\frac{\eta P(\mathbf{r}, t)}{\rho v_a^2}\right)\right] E(\mathbf{r}, t) = F(\mathbf{r}), \tag{5.1}$$

where $2\eta P(\mathbf{r}, t)/(\rho v_a^2) \ll 1$.

For a point source at position $\mathbf{r}_0$, $F(\mathbf{r}) = \delta(\mathbf{r} - \mathbf{r}_0)$, where $\delta(\,)$ is the Dirac delta function, and the solution of Eq. (5.1) is the Green's function $G_a(\mathbf{r}, \mathbf{r}_0, t)$. We present $G_a(\mathbf{r}, \mathbf{r}_0, t)$ as

$$G_a(\mathbf{r}, \mathbf{r}_0, t) \;=\; \frac{\exp(ik_0 n_0 |\mathbf{r} - \mathbf{r}_0|[1 + \xi(\mathbf{r}, \mathbf{r}_0, t)])}{-4\pi|\mathbf{r} - \mathbf{r}_0|}, \tag{5.2}$$

where the small fractional phase perturbation $\xi(\mathbf{r}, \mathbf{r}_0, t)$ is the slowly varying function of $P(\mathbf{r}, t)$ and where $k_0 n_0 |\mathbf{r} - \mathbf{r}_0| \xi(\mathbf{r}, \mathbf{r}_0, t)$ vanishes whenever $\mathbf{r} \to \mathbf{r}_0$ or $2\eta P(\mathbf{r}, t)/(\rho v_a^2)$ $\to 0$. We consider moderate ultrasound pressures and distances $\mathbf{r}$ not far from the source position $\mathbf{r}_0$ such that $k_0 n_0 |\mathbf{r} - \mathbf{r}_0| \xi(\mathbf{r}, \mathbf{r}_0, t) \ll 1$, and we approximate $\xi(\mathbf{r}, \mathbf{r}_0, t)$ with an integral over the optical path increments along the line between $\mathbf{r}_0$ and $\mathbf{r}$ as

$$\xi(\mathbf{r}, \mathbf{r}_0, t) = \frac{\eta}{\rho v_a^2 |\mathbf{r} - \mathbf{r}_0|} \int_{\mathbf{r}_0}^{\mathbf{r}} P(\mathbf{r}', t) dr'. \tag{5.3}$$

By performing the integration in Eq. (5.3) along the straight line which connects $\mathbf{r}_0$ and $\mathbf{r}$, we assume that the ultrasound-induced refraction of the optical waves is

negligible for the interaction length $|\mathbf{r} - \mathbf{r}_0|$.

We then consider a medium with discrete and uncorrelated optical scatterers. We assume independent optical scattering and an optical wavelength λ_0 that is much smaller than l_s (weak scattering approximation). We also assume that a monochromatic ultrasound field, in an optically scattering medium representative of soft biological tissue, is uniform on scales that are comparable with l_{tr}, and we locally approximate the ultrasound pressure with $P(\mathbf{r}, t) = P_0 \cos(\omega_a t - \mathbf{k}_a \cdot \mathbf{r} + \phi)$, where $\mathbf{k}_a = k_a \hat{\mathbf{\Omega}}_a$ is the ultrasound wave vector and P_0, ω_a, ϕ, and $\hat{\mathbf{\Omega}}_a$ are the pressure amplitude, angular frequency, local initial phase, and propagation direction unit vector of the ultrasound, respectively ($|\hat{\mathbf{\Omega}}_a| = 1$). This allows us to write an explicit expression for the fractional phase perturbation $\xi(\mathbf{r}, \mathbf{r}_0, t)$ as

$$\xi(\mathbf{r}, \mathbf{r}_0, t) \;=\; \frac{1}{2} M \cos\left(\omega_a t - \mathbf{k}_a \cdot \frac{\mathbf{r} + \mathbf{r}_0}{2} + \phi\right) \mathrm{sinc}\left(\mathbf{k}_a \cdot \frac{\mathbf{r} - \mathbf{r}_0}{2}\right), \qquad (5.4)$$

where $\mathrm{sinc}(x) = \sin(x)/x$, and $M = 2\eta P_0/(\rho v_a^2)$.

The accuracy of Eq. (5.2) with $\xi(\mathbf{r}, \mathbf{r}_0, t)$ given by Eq. (5.4) is worse for large values of $|\mathbf{r} - \mathbf{r}_0|$. For further derivations, Eq. (5.2) is required to be approximately valid for $|\mathbf{r} - \mathbf{r}_0|$ on the order of a few l_{tr}. This requirement is satisfied in soft biological tissues at visible and near-infrared optical wavelengths ($l_{tr} \approx 1$ mm), for moderate ultrasound pressures ($P_0 \leq 10^5$ Pa) and in the medical ultrasound frequency range.[45]

The scattering cross section σ_s is related to the optical scattering amplitude $f(\hat{\mathbf{\Omega}}_{sc}, \hat{\mathbf{\Omega}}_{inc})$ as $\sigma_s = \int_{4\pi} |f(\hat{\mathbf{\Omega}}_{sc}, \hat{\mathbf{\Omega}}_{inc})|^2 d\Omega_{sc}$, where $\hat{\mathbf{\Omega}}_{inc}$ and $\hat{\mathbf{\Omega}}_{sc}$ are the directions of the incident and scattered waves, respectively, and we assume that the scattering potential is spherically symmetric such that $f(\hat{\mathbf{\Omega}}_{sc}, \hat{\mathbf{\Omega}}_{inc})$ is a function of $\hat{\mathbf{\Omega}}_{sc} \cdot \hat{\mathbf{\Omega}}_{inc}$ only. The scattering phase function $p(\hat{\mathbf{\Omega}}_{sc}, \hat{\mathbf{\Omega}}_{inc})$ is defined as $p(\hat{\mathbf{\Omega}}_{sc}, \hat{\mathbf{\Omega}}_{inc}) = \sigma_s^{-1} |f(\hat{\mathbf{\Omega}}_{sc}, \hat{\mathbf{\Omega}}_{inc})|^2$, and it satisfies $\int_{4\pi} p(\hat{\mathbf{\Omega}}_{sc}, \hat{\mathbf{\Omega}}_{inc}) d\Omega_{sc} = 1$. In addition, from the optical theorem, we have $\sigma_s + \sigma_a = 4\pi \mathrm{Im}[f(\hat{\mathbf{\Omega}}_{inc}, \hat{\mathbf{\Omega}}_{inc})]/(k_0 n_0)$, where σ_a is the optical

absorption cross section, and Im[ ] is an imaginary part. If ρ_s is the density of optical scatterers, then the optical extinction, scattering and absorption coefficients are defined as $\mu_t = \mu_s + \mu_a$, $\mu_s = \sigma_s \rho_s$, and $\mu_a = \sigma_a \rho_s$, respectively.

We assume sufficiently small optical scatterers and consider only the far field approximations of the scattered fields. The far filed approximation of field $E_s(\mathbf{r}, t)$ produced by the scattering of the plane wave $\exp(ik_0 n_0 \hat{\mathbf{\Omega}}_{inc} \cdot \mathbf{r})$ from the single optical scatterer at $\mathbf{r}_s$ is given by

$$\begin{aligned} E_s(\mathbf{r}, t) &= -4\pi G_a(\mathbf{r}, \mathbf{r}_s, t) f(\hat{\mathbf{\Omega}}_{sc}, \hat{\mathbf{\Omega}}_{inc}) \\ &\quad \times \exp[ik_0 n_0 \mathbf{e}_s(t) \cdot (\hat{\mathbf{\Omega}}_{inc} - \hat{\mathbf{\Omega}}_{sc})] \exp(ik_0 n_0 \hat{\mathbf{\Omega}}_{inc} \cdot \mathbf{r}_s), \end{aligned} \tag{5.5}$$

where $\hat{\mathbf{\Omega}}_{sc} = (\mathbf{r} - \mathbf{r}_s)/|\mathbf{r} - \mathbf{r}_s|$ and the refraction of the optical waves due to the ultrasound field is neglected. The first exponential term on the right hand side of Eq. (5.5) accounts for the Doppler shift caused by the ultrasound-induced movement of the scatterer. The position of the scatterer at moment t is $\mathbf{r}_s + \mathbf{e}_s(t)$, where $\mathbf{r}_s$ is the resting position and $\mathbf{e}_s(t)$ is the small ultrasound-induced displacement given by $\mathbf{e}_s(t) = \hat{\mathbf{\Omega}}_a P_0 S_a (k_a \rho v_a^2)^{-1} \sin(\omega_a t - \mathbf{k}_a \cdot \mathbf{r}_s - \phi_a + \phi)$. In general, S_a and ϕ_a represent the deviations of the amplitude and the phase of the scatterer displacement from the movement of the surrounding fluid.[45,56] However, we expect that an endogenous optical scatterer in soft biological tissue closely follows the ultrasound-induced "background" tissue vibrations, i.e., $S_a \approx 1$ and $\phi_a \approx 0$.

When multiple scattering is considered, the mean Green's function $G_s(\mathbf{r}_b, \mathbf{r}_a, t)$ provides the ensemble averaged value of the electric field (referred to also as a mean or coherent field) at $\mathbf{r}_b$ emitted from a point source at $\mathbf{r}_a$. We obtain $G_s(\mathbf{r}_b, \mathbf{r}_a, t)$ by solving the Dyson equation,[46,52,53] whose far-field expression in the Bourret approx-

imation is given by

$$G_s(\mathbf{r}_b, \mathbf{r}_a, t) = G_a(\mathbf{r}_b, \mathbf{r}_a, t) - 4\pi\rho_s \int G_a(\mathbf{r}_b, \mathbf{r}_s, t) f(\hat{\mathbf{\Omega}}_{sb}, \hat{\mathbf{\Omega}}_{as}) \times \exp[ik_0 n_0 \mathbf{e}_s(t) \cdot (\hat{\mathbf{\Omega}}_{as} - \hat{\mathbf{\Omega}}_{sb})]\ G_s(\mathbf{r}_s, \mathbf{r}_a, t)\ d\mathbf{r}_s. \tag{5.6}$$

In Eq. (5.6), $\hat{\mathbf{\Omega}}_{as}$ and $\hat{\mathbf{\Omega}}_{sb}$ are unity vectors in directions $\mathbf{r}_s - \mathbf{r}_a$ and $\mathbf{r}_b - \mathbf{r}_s$, respectively, and the refraction of the mean optical field that is due to the ultrasound is neglected.

By applying the method of stationary phase to Eq. (5.6), we obtain the following solution (see Appendix)

$$G_s(\mathbf{r}_b, \mathbf{r}_a, t) = \frac{\exp\left(iK(\mathbf{r}_b, \mathbf{r}_a, t)|\mathbf{r}_b - \mathbf{r}_a|\right)}{-4\pi|\mathbf{r}_b - \mathbf{r}_a|}, \tag{5.7}$$

where $K(\mathbf{r}_b, \mathbf{r}_a, t) = k_0 n_0[1 + \xi(\mathbf{r}_b, \mathbf{r}_a, t)] + 2\pi\rho_s f(\hat{\mathbf{\Omega}}, \hat{\mathbf{\Omega}})/(k_0 n_0)$. The difference between the mean Green's function $G_s(\mathbf{r}_b, \mathbf{r}_a, t)$ given by Eq. (5.7) and the free-space Green's function $G(\mathbf{r}_b, \mathbf{r}_a, t) = \exp(ik_0 n_0 |\mathbf{r}_b - \mathbf{r}_a|)/(-4\pi|\mathbf{r}_b - \mathbf{r}_a|)$ is in the form of the propagation constant $K(\mathbf{r}_b, \mathbf{r}_a, t)$. The term $\xi(\mathbf{r}_b, \mathbf{r}_a, t)$ is related to the accumulated optical phase from $\mathbf{r}_a$ to $\mathbf{r}_b$, due to ultrasound-induced changes in the optical index of refraction. The term $2\pi\rho_s f(\hat{\mathbf{\Omega}}, \hat{\mathbf{\Omega}})/(k_0 n_0)$ accounts for the multiple wave scattering from $\mathbf{r}_a$ to $\mathbf{r}_b$, and its real and imaginary parts are related to the reduction of the propagation speed and the attenuation of the mean field, respectively. Also, in the absence of optical scatterers, the term $2\pi\rho_s f(\hat{\mathbf{\Omega}}, \hat{\mathbf{\Omega}})/(k_0 n_0)$ vanishes, and $G_s(\mathbf{r}_b, \mathbf{r}_a, t)$ reduces to $G_a(\mathbf{r}_b, \mathbf{r}_a, t)$.

3. Development of the CTE

The mutual coherence function of the electrical field component is given by the following expression

$$\Gamma(\mathbf{r}_a, \mathbf{r}_b, t, \tau) = \langle E(\mathbf{r}_a, t) E^*(\mathbf{r}_b, t+\tau) \rangle, \tag{5.8}$$

where $\mathbf{r}_a$ and $\mathbf{r}_b$ are two closely spaced points relative to the mean free path l_t, and $\langle\ \rangle$ represents ensemble averaging. We assume a quasi-uniform $\Gamma(\mathbf{r}_a, \mathbf{r}_b, t, \tau)$, which varies more slowly in respect to the center of gravity coordinate $\mathbf{r}_c = (\mathbf{r}_a + \mathbf{r}_b)/2$ than in respect to the difference coordinate $\mathbf{r}_d = \mathbf{r}_a - \mathbf{r}_b$ ($|\partial_{\mathbf{r}_c}\Gamma| \ll |\partial_{\mathbf{r}_d}\Gamma|$). Under the weak-scattering approximation, $\Gamma(\mathbf{r}_a, \mathbf{r}_b, t, \tau)$ satisfies the ladder approximation of the Bethe-Salpeter equation[46,52,53,55] for moving scatterers

$$\begin{aligned} \Gamma(\mathbf{r}_a, \mathbf{r}_b, t, \tau) &= \Gamma_0(\mathbf{r}_a, \mathbf{r}_b, t, \tau) \\ &\quad + \iint v^a_{s'}(t) v^{b*}_{s''}(t+\tau) \Gamma(\mathbf{r}_{s'}, \mathbf{r}_{s''}, t, \tau) \rho(\mathbf{r}_{s'}, t; \mathbf{r}_{s''}, t+\tau) d\mathbf{r}_{s'} d\mathbf{r}_{s''}, \end{aligned} \tag{5.9}$$

where $\Gamma_0(\mathbf{r}_a, \mathbf{r}_b, t, \tau) = \langle E(\mathbf{r}_a, t) \rangle \langle E^*(\mathbf{r}_b, t+\tau) \rangle$ is the mutual coherence function of the coherent (unscattered) field, and $\mathbf{r}_{s'}$ and $\mathbf{r}_{s''}$ are the positions of the same scatterer at time moments t and $t+\tau$, respectively. The function $\rho(\mathbf{r}_{s'}, t; \mathbf{r}_{s''}, t+\tau)$ is the probability density of finding the same scatterer s at position $\mathbf{r}_{s'}$ and time t, and at position $\mathbf{r}_{s''}$ and time $t+\tau$. By assuming the far field approximation of the operators $v^a_{s'}(t)$ and $v^{b*}_{s''}(t+\tau)$, the term $v^a_{s'}(t) v^{b*}_{s''}(t+\tau) \Gamma(\mathbf{r}_{s'}, \mathbf{r}_{s''}, t, \tau)$ in Eq. (5.9) can be written as an integral over all the spectral components of $\Gamma(\mathbf{r}_{s'}, \mathbf{r}_{s''}, t, \tau)$. The spectral density $\tilde{\Gamma}(\mathbf{r}_{cs}, \mathbf{q}', t, \tau)$ of $\Gamma(\mathbf{r}_{s'}, \mathbf{r}_{s''}, t, \tau)$ is defined as the spatial Fourier transform in respect to the difference variable $\mathbf{r}_{ds} = \mathbf{r}_{s'} - \mathbf{r}_{s''}$

$$\tilde{\Gamma}(\mathbf{r}_{cs}, \mathbf{q}', t, \tau) = (2\pi)^{-3} \int \Gamma(\mathbf{r}_{cs}, \mathbf{r}_{ds}, t, \tau) \exp(-i\mathbf{q}' \cdot \mathbf{r}_{ds}) d\mathbf{r}_{ds}, \tag{5.10}$$

where $\mathbf{r}_{cs} = (\mathbf{r}_{s'} + \mathbf{r}_{s''})/2$. The formal expressions of the operators $v^a_{s'}(t)$ and $v^{b*}_{s''}(t+\tau)$ in the far-field approximation are given by $V^a_{s'}(t, \hat{\mathbf{\Omega}}') = -4\pi G_s(\mathbf{r}_a, \mathbf{r}_{s'}, t) f(\hat{\mathbf{\Omega}}_{s'a}, \hat{\mathbf{\Omega}}')$ and $V^{b*}_{s''}(t+\tau, \hat{\mathbf{\Omega}}') = -4\pi G^*_s(\mathbf{r}_b, \mathbf{r}_{s''}, t+\tau) f^*(\hat{\mathbf{\Omega}}_{s''b}, \hat{\mathbf{\Omega}}')$, respectively, where $\hat{\mathbf{\Omega}}' = \mathbf{q}'/|\mathbf{q}'|$. Finally, the term $v^a_{s'}(t) v^{b*}_{s''}(t+\tau)\Gamma(\mathbf{r}_{s'}, \mathbf{r}_{s''}, t, \tau)$ in the integral in Eq. (5.9) can be written as

$$v^a_{s'}(t) v^{b*}_{s''}(t+\tau)\Gamma(\mathbf{r}_{s'}, \mathbf{r}_{s''}, t, \tau) \equiv \int V^a_{s'}(t, \hat{\mathbf{\Omega}}') V^{b*}_{s''}(t+\tau, \hat{\mathbf{\Omega}}')\tilde{\Gamma}(\mathbf{r}_{cs}, \mathbf{q}', t, \tau) \times \exp(i\mathbf{q}' \cdot \mathbf{r}_{ds}) d\mathbf{q}', \tag{5.11}$$

where

$$V^a_{s'}(t, \hat{\mathbf{\Omega}}') V^{b*}_{s''}(t+\tau, \hat{\mathbf{\Omega}}') = \frac{f(\hat{\mathbf{\Omega}}_{s'a}, \hat{\mathbf{\Omega}}') f^*(\hat{\mathbf{\Omega}}_{s''b}, \hat{\mathbf{\Omega}}')}{|\mathbf{r}_a - \mathbf{r}_{s'}||\mathbf{r}_b - \mathbf{r}_{s''}|} \exp\left(iK(\mathbf{r}_a, \mathbf{r}_{s'}, t)|\mathbf{r}_a - \mathbf{r}_{s'}|\right) \times \exp\left(-iK^*(\mathbf{r}_b, \mathbf{r}_{s''}, t+\tau)|\mathbf{r}_b - \mathbf{r}_{s''}|\right). \tag{5.12}$$

To simplify the expression on the right-hand side of Eq. (5.12), we use previously defined vectors in the center-of-gravity coordinate systems $\mathbf{r}_c = (\mathbf{r}_a + \mathbf{r}_b)/2$, $\mathbf{r}_d = \mathbf{r}_a - \mathbf{r}_b$, $\mathbf{r}_{cs} = (\mathbf{r}_{s'} + \mathbf{r}_{s''})/2$, $\mathbf{r}_{ds} = \mathbf{r}_{s'} - \mathbf{r}_{s''}$, and we also define $\hat{\mathbf{\Omega}} = (\mathbf{r}_c - \mathbf{r}_{cs})/|\mathbf{r}_c - \mathbf{r}_{cs}|$. Since $|\mathbf{r}_d| \ll |\mathbf{r}_c - \mathbf{r}_{cs}|$ and $|\mathbf{r}_{ds}| \ll |\mathbf{r}_c - \mathbf{r}_{cs}|$, we assume $f(\hat{\mathbf{\Omega}}_{s'a}, \hat{\mathbf{\Omega}}') \approx f(\hat{\mathbf{\Omega}}, \hat{\mathbf{\Omega}}')$, $f(\hat{\mathbf{\Omega}}_{s''b}, \hat{\mathbf{\Omega}}') \approx f(\hat{\mathbf{\Omega}}, \hat{\mathbf{\Omega}}')$, and

$$\begin{aligned} |\mathbf{r}_a - \mathbf{r}_{s'}| &\approx |\mathbf{r}_c - \mathbf{r}_{cs}| + (\mathbf{r}_d - \mathbf{r}_{ds}) \cdot \hat{\mathbf{\Omega}}/2, \\ |\mathbf{r}_b - \mathbf{r}_{s''}| &\approx |\mathbf{r}_c - \mathbf{r}_{cs}| - (\mathbf{r}_d - \mathbf{r}_{ds}) \cdot \hat{\mathbf{\Omega}}/2, \\ (|\mathbf{r}_a - \mathbf{r}_{s'}||\mathbf{r}_b - \mathbf{r}_{s''}|)^{-1} &\approx |\mathbf{r}_c - \mathbf{r}_{cs}|^{-2}. \end{aligned} \tag{5.13}$$

Eq. (5.12) can be now presented as

$$V^a_{s'}(t, \hat{\mathbf{\Omega}}') V^{b*}_{s''}(t+\tau, \hat{\mathbf{\Omega}}') = \sigma_s p(\hat{\mathbf{\Omega}}, \hat{\mathbf{\Omega}}')|\mathbf{r}_c - \mathbf{r}_{cs}|^{-2} \exp\left(iK_r(\mathbf{r}_d - \mathbf{r}_{ds}) \cdot \hat{\mathbf{\Omega}} - \mu_t|\mathbf{r}_c - \mathbf{r}_{cs}|\right) \times \exp[i\Psi_n(\mathbf{r}_a, \mathbf{r}_b, \mathbf{r}_{s'}, \mathbf{r}_{s''}, t, \tau)], \tag{5.14}$$

where $K_r = n_0 k_0 + 4\pi \mathrm{Re}[f(\hat{\mathbf{\Omega}}, \hat{\mathbf{\Omega}})]\rho_s/(2k_0 n_0)$, and Re[ ] is the real part. The difference between the ultrasound-induced phase increments $\Psi_n(\mathbf{r}_a, \mathbf{r}_b, \mathbf{r}_{s'}, \mathbf{r}_{s''}, t, \tau)$ is given by

$$\begin{aligned} \Psi_n(\mathbf{r}_a, \mathbf{r}_b, \mathbf{r}_{s'}, \mathbf{r}_{s''}, t, \tau) &= k_0 n_0 |\mathbf{r}_a - \mathbf{r}_{s'}| \xi(\mathbf{r}_a, \mathbf{r}_{s'}, t) \\ &\quad - k_0 n_0 |\mathbf{r}_b - \mathbf{r}_{s''}| \xi(\mathbf{r}_b, \mathbf{r}_{s''}, t+\tau). \end{aligned} \tag{5.15}$$

By using the relations in Eq. (5.13), the expression in Eq. (5.15) is approximated as $\Psi_n(\mathbf{r}_a, \mathbf{r}_b, \mathbf{r}_{s'}, \mathbf{r}_{s''}, t, \tau) \approx \Psi_n(\mathbf{r}_c, \mathbf{r}_{cs}, \hat{\mathbf{\Omega}}, t, \tau)$ where

$$\begin{aligned} \Psi_n(\mathbf{r}_c, \mathbf{r}_{cs}, \hat{\mathbf{\Omega}}, t, \tau) &= \frac{2\Lambda_n k_a}{\mathbf{k}_a \cdot \hat{\mathbf{\Omega}}} \sin\left(\omega_a \frac{\tau}{2}\right) \\ &\quad \times \sin\left[\omega_a \left(t + \frac{\tau}{2}\right) - \mathbf{k}_a \cdot \frac{\mathbf{r}_c + \mathbf{r}_{cs}}{2} + \phi\right] \sin\left(\mathbf{k}_a \cdot \frac{\mathbf{r}_c - \mathbf{r}_{cs}}{2}\right). \end{aligned} \tag{5.16}$$

In Eq. (5.16), $\Lambda_n = 2k_0 n_0 \eta P_0/(k_a \rho_s v_a^2)$.

We express the positions $\mathbf{r}_{s'}$ and $\mathbf{r}_{s''}$ of the scatterer at the time moments t and $t+\tau$ as $\mathbf{r}_{s'} = \mathbf{r}_s + \mathbf{e}_s(t)$ and $\mathbf{r}_{s''} = \mathbf{r}_s + \mathbf{e}_s(t+\tau)$, respectively. The probability density function $\rho(\mathbf{r}_{s'}, t; \mathbf{r}_{s''}, t+\tau)$ in Eq. (5.9) is given by

$$\rho(\mathbf{r}_{s'}, t; \mathbf{r}_{s''}, t+\tau) = \rho_s \delta(\mathbf{r}_{ds} - \Delta\mathbf{e}(\mathbf{r}_s, t, \tau)), \tag{5.17}$$

where $\Delta\mathbf{e}(\mathbf{r}_s, t, \tau) = \mathbf{e}_s(t) - \mathbf{e}_s(t+\tau)$. By replacing the integration over positions $\mathbf{r}_{s'}$ and $\mathbf{r}_{s''}$ with an integration over $\mathbf{r}_{ds}$ and $\mathbf{r}_{cs}$, Eq. (5.9) becomes

$$\begin{aligned} \Gamma(\mathbf{r}_c, \mathbf{r}_d, t, \tau) &= \Gamma_0(\mathbf{r}_c, \mathbf{r}_d, t, \tau) \\ &\quad + \int \mu_s p(\hat{\mathbf{\Omega}}, \hat{\mathbf{\Omega}}') \exp[iK_r(\mathbf{r}_d - \mathbf{r}_{ds}) \cdot \hat{\mathbf{\Omega}}] \exp[i\Psi_n(\mathbf{r}_c, \mathbf{r}_{cs}, t, \tau)] \\ &\quad \times \exp(-\mu_t |\mathbf{r}_c - \mathbf{r}_{cs}|) \tilde{\Gamma}(\mathbf{r}_{cs}, \mathbf{q}', t, \tau) \exp(i\mathbf{q}' \cdot \mathbf{r}_{ds}) \\ &\quad \times \delta(\mathbf{r}_{ds} - \Delta\mathbf{e}(\mathbf{r}_s, t, \tau)) d\mathbf{r}_{ds} d|\mathbf{r}_c - \mathbf{r}_{cs}| d\Omega d\mathbf{q}', \end{aligned} \tag{5.18}$$

where we used $d\mathbf{r}_{cs} = |\mathbf{r}_c - \mathbf{r}_{cs}|^2 d|\mathbf{r}_c - \mathbf{r}_{cs}| d\Omega$. After performing an additional inte-

gration over $\mathbf{r}_{ds}$, we have

$$\begin{aligned}\Gamma(\mathbf{r}_c,\mathbf{r}_d,t,\tau) &= \Gamma_0(\mathbf{r}_c,\mathbf{r}_d,t,\tau) \\ &+\int \mu_s p(\hat{\mathbf{\Omega}},\hat{\mathbf{\Omega}}')\exp(iK_r\mathbf{r}_d\cdot\hat{\mathbf{\Omega}})\exp(-\mu_t|\mathbf{r}_c-\mathbf{r}_{cs}|) \\ &\times\exp[i(\mathbf{q}'-K_r\hat{\mathbf{\Omega}})\cdot\Delta\mathbf{e}(\mathbf{r}_s,t,\tau)]\exp[i\Psi_n(\mathbf{r}_c,\mathbf{r}_{cs},t,\tau)] \\ &\times\tilde{\Gamma}(\mathbf{r}_{cs},\mathbf{q}',t,\tau)d|\mathbf{r}_c-\mathbf{r}_{cs}|d\Omega d\mathbf{q}',\end{aligned} \tag{5.19}$$

where $\exp(-\mu_t|\mathbf{r}_c-\mathbf{r}_{cs}|)$ accounts for the attenuation of the field, and the exponential terms that contain $\Delta\mathbf{e}(\,)$ and $\Psi_n(\,)$ are due to the ultrasound-induced optical phase increments.

Eq. (5.19) can be further simplified[27,47,49,50,55,57,58] by realizing that for quasi-monochromatic light, the spectral density $\tilde{\Gamma}(\mathbf{r}_{cs},\mathbf{q}',t,\tau)$ of the quasi-uniform mutual coherence function is approximately concentrated on a spherical shell with radius $|\mathbf{q}'|=K_r$.[47,49,50,57,58] We relate then the time-varying specific intensity $I(\mathbf{r}_{cs},\hat{\mathbf{\Omega}}',t,\tau)$ to the spectral density $\tilde{\Gamma}(\mathbf{r}_{cs},\mathbf{q}',t,\tau)$ by the following approximation:

$$\tilde{\Gamma}(\mathbf{r}_{cs},\mathbf{q}',t,\tau)\approx\delta(|\mathbf{q}'|-K_r)I(\mathbf{r}_{cs},\hat{\mathbf{\Omega}}',t,\tau)/K_r^2. \tag{5.20}$$

For $\Gamma(\mathbf{r}_c,\mathbf{r}_d,t,\tau)$ and $\Gamma_0(\mathbf{r}_c,\mathbf{r}_d,t,\tau)$, we write the expressions similar to Eqs. (5.10) and (5.20) and combine them to obtain the following relations:

$$\Gamma(\mathbf{r}_c,\mathbf{r}_d,t,\tau)=\int I(\mathbf{r}_c,\hat{\mathbf{\Omega}},t,\tau)\exp(iK_r\hat{\mathbf{\Omega}}\cdot\mathbf{r}_d)d\Omega, \tag{5.21a}$$

$$\Gamma_0(\mathbf{r}_c,\mathbf{r}_d,t,\tau)=\int I_0(\mathbf{r}_c,\hat{\mathbf{\Omega}},t,\tau)\exp(iK_r\hat{\mathbf{\Omega}}\cdot\mathbf{r}_d)d\Omega, \tag{5.21b}$$

where the time-varying specific intensity is presented as an angular spectrum of the mutual coherence function. From Eq. (5.21a), we note that the temporal field correlation function $\Gamma(\mathbf{r}_c,0,t,\tau)$ is given by $\int I(\mathbf{r}_c,\hat{\mathbf{\Omega}},t,\tau)d\Omega$. Therefore, the optical power spectrum density of the ultrasound modulated light received in some solid angle Ω_0

can be obtained by the temporal Fourier transform of $I_{\Omega_0}(\mathbf{r}_c,\tau)=\int_{\Omega_0} I(\mathbf{r}_c,\hat{\mathbf{\Omega}},\tau)d\Omega$, where $I(\mathbf{r}_c,\hat{\mathbf{\Omega}},\tau)$ is obtained by averaging the time-varying specific intensity over an ultrasound period as[39]

$$I(\mathbf{r}_c,\hat{\mathbf{\Omega}},\tau)=\frac{\omega_a}{2\pi}\int_0^{2\pi/\omega_a} I(\mathbf{r}_c,\hat{\mathbf{\Omega}},t,\tau)dt. \tag{5.22}$$

Finally, the integral form of the CTE is obtained by substituting Eqs. (5.21a), (5.21b), and (5.20) into Eq. (5.19), performing the integration over $|\mathbf{q}'|$, and by subsequently removing the integrals over $\hat{\mathbf{\Omega}}$, together with exponents $\exp(iK_r\hat{\mathbf{\Omega}}\cdot\mathbf{r}_d)$ which are common for all terms. We write the final result as

$$\begin{aligned} I(\mathbf{r},\hat{\mathbf{\Omega}},t,\tau)=I_0(\mathbf{r},\hat{\mathbf{\Omega}},t,\tau)+ & \int \mu_s p(\hat{\mathbf{\Omega}},\hat{\mathbf{\Omega}}')\exp(-\mu_t|\mathbf{r}-\mathbf{r}_s|)I(\mathbf{r}_s,\hat{\mathbf{\Omega}}',t,\tau) \\ & \times\Phi(\mathbf{r},\mathbf{r}_s,\hat{\mathbf{\Omega}},\hat{\mathbf{\Omega}}',t,\tau)d|\mathbf{r}-\mathbf{r}_s|d\Omega', \end{aligned} \tag{5.23}$$

where it is assumed that $\mathbf{r}_{cs}\approx\mathbf{r}_s$, and we also removed now redundant subscript c from the center-of-gravity coordinate $\mathbf{r}_c$. In Eq. (5.23), the term $\Phi(\mathbf{r},\mathbf{r}_s,\hat{\mathbf{\Omega}},\hat{\mathbf{\Omega}}',t,\tau)=\exp[i\Psi_d(\mathbf{r}_s,\hat{\mathbf{\Omega}},\hat{\mathbf{\Omega}}',t,\tau)]\exp[i\Psi_n(\mathbf{r},\mathbf{r}_s,\hat{\mathbf{\Omega}},t,\tau)]$ accounts for the ultrasound-induced optical phase increments due to both mechanisms of modulation. The displacement term $\Psi_d(\mathbf{r}_s,\hat{\mathbf{\Omega}},\hat{\mathbf{\Omega}}',t,\tau)=-K_r(\hat{\mathbf{\Omega}}-\hat{\mathbf{\Omega}}')\cdot\Delta\mathbf{e}(\mathbf{r}_s,t,\tau)$ is given by

$$\begin{aligned} \Psi_d(\mathbf{r}_s,\hat{\mathbf{\Omega}},\hat{\mathbf{\Omega}}',t,\tau) &= \Lambda_d[(\hat{\mathbf{\Omega}}-\hat{\mathbf{\Omega}}')\cdot\hat{\mathbf{\Omega}}_a]\sin\left(\omega_a\frac{\tau}{2}\right) \\ &\quad\times\cos\left[\omega_a\left(t+\frac{\tau}{2}\right)-\mathbf{k}_a\cdot\mathbf{r}_s-\phi_a+\phi\right], \end{aligned} \tag{5.24}$$

where $\Lambda_d=2K_rS_aP_0/(k_a\rho_s v_a^2)$.

The differential form of the CTE is obtained by taking the gradient of the integral form of the CTE [Eq. (5.23)] in the $\hat{\mathbf{\Omega}}$ direction.[27] By applying $\hat{\mathbf{\Omega}}\cdot\partial/\partial\mathbf{r}$ to

Eq. (5.23), we have

$$\hat{\mathbf{\Omega}}\cdot\frac{\partial I(\mathbf{r},\hat{\mathbf{\Omega}},t,\tau)}{\partial\mathbf{r}} = \hat{\mathbf{\Omega}}\cdot\frac{\partial I_0(\mathbf{r},\hat{\mathbf{\Omega}},t,\tau)}{\partial\mathbf{r}} \tag{5.25}$$
$$+\int_{4\pi}\mu_s p(\hat{\mathbf{\Omega}},\hat{\mathbf{\Omega}}')\left\{\hat{\mathbf{\Omega}}\cdot\frac{\partial}{\partial\mathbf{r}}\int_{\mathbf{r}_0}^{\mathbf{r}}\Phi(\mathbf{r},\mathbf{r}_s,\hat{\mathbf{\Omega}},\hat{\mathbf{\Omega}}',t,\tau)\exp(-\mu_t|\mathbf{r}-\mathbf{r}_s|)I(\mathbf{r}_s,\hat{\mathbf{\Omega}}',t,\tau)d|\mathbf{r}-\mathbf{r}_s|\right\}d\Omega'.$$

We denote with $D_{\{\}}$ the derivative in the wavy brackets on the right hand side of Eq. (5.25) and express its value as

$$\begin{aligned} D_{\{\}} &= \Phi(\mathbf{r},\mathbf{r},\hat{\mathbf{\Omega}},\hat{\mathbf{\Omega}}',t,\tau)I(\mathbf{r},\hat{\mathbf{\Omega}}',t,\tau) \\ &\quad -\int_{\mathbf{r}_0}^{\mathbf{r}}\mu_t\Phi(\mathbf{r},\mathbf{r}_s,\hat{\mathbf{\Omega}},\hat{\mathbf{\Omega}}',t,\tau)\exp(-\mu_t|\mathbf{r}-\mathbf{r}_s|)I(\mathbf{r}_s,\hat{\mathbf{\Omega}}',t,\tau)d|\mathbf{r}-\mathbf{r}_s| \\ &\quad +\int_{\mathbf{r}_0}^{\mathbf{r}}\hat{\mathbf{\Omega}}\cdot\frac{\partial\Phi(\mathbf{r},\mathbf{r}_s,\hat{\mathbf{\Omega}},\hat{\mathbf{\Omega}}',t,\tau)}{\partial\mathbf{r}}\exp(-\mu_t|\mathbf{r}-\mathbf{r}_s|)I(\mathbf{r}_s,\hat{\mathbf{\Omega}}',t,\tau)d|\mathbf{r}-\mathbf{r}_s|. \end{aligned} \tag{5.26}$$

Next, we substitute the expressions from Eqs. (5.26) and (5.23) into Eq. (5.25) to obtain

$$\begin{aligned} \left\{\hat{\mathbf{\Omega}}\cdot\frac{\partial}{\partial\mathbf{r}}+\mu_t\right\}I(\mathbf{r},\hat{\mathbf{\Omega}},t,\tau) &= \left\{\hat{\mathbf{\Omega}}\cdot\frac{\partial}{\partial\mathbf{r}}+\mu_t\right\}I_0(\mathbf{r},\hat{\mathbf{\Omega}},t,\tau) \\ &\quad +\mu_s\int_{4\pi}p(\hat{\mathbf{\Omega}},\hat{\mathbf{\Omega}}')\exp[i\Psi_d(\mathbf{r},\hat{\mathbf{\Omega}},\hat{\mathbf{\Omega}}',t,\tau)]I(\mathbf{r},\hat{\mathbf{\Omega}}',t,\tau)d\Omega' \\ &\quad +\tilde{\Lambda}_n(\mathbf{r},t,\tau)\mu_s\int_{4\pi}p(\hat{\mathbf{\Omega}},\hat{\mathbf{\Omega}}')\int_{\mathbf{r}_0}^{\mathbf{r}}\Phi(\mathbf{r},\mathbf{r}_s,\hat{\mathbf{\Omega}},\hat{\mathbf{\Omega}}',t,\tau) \\ &\quad \times\exp(-\mu_t|\mathbf{r}-\mathbf{r}_s|)I(\mathbf{r}_s,\hat{\mathbf{\Omega}}',t,\tau)d|\mathbf{r}-\mathbf{r}_s|d\Omega', \end{aligned} \tag{5.27}$$

where $\hat{\mathbf{\Omega}}\cdot\partial\Phi(\mathbf{r},\mathbf{r}_s,\hat{\mathbf{\Omega}},\hat{\mathbf{\Omega}}',t,\tau)/\partial\mathbf{r}$ is represented as $\tilde{\Lambda}_n(\mathbf{r},t,\tau)\Phi(\mathbf{r},\mathbf{r}_s,\hat{\mathbf{\Omega}},\hat{\mathbf{\Omega}}',t,\tau)$, and

$$\tilde{\Lambda}_n(\mathbf{r},t,\tau) = ik_a\Lambda_n\sin\left(\omega_a\frac{\tau}{2}\right)\sin\left[\omega_a\left(t+\frac{\tau}{2}\right)-\mathbf{k}_a\cdot\mathbf{r}+\phi\right]. \tag{5.28}$$

After substitution of Eq. (5.23) into Eq. (5.27), we obtain the final expression

for the differential form of the CTE

$$\left\{\hat{\mathbf{\Omega}}\cdot\frac{\partial}{\partial\mathbf{r}}+\mu_t-\tilde{\Lambda}_n(\mathbf{r},t,\tau)\right\}I(\mathbf{r},\hat{\mathbf{\Omega}},t,\tau) \;=\; \mu_s\int_{4\pi}p(\hat{\mathbf{\Omega}},\hat{\mathbf{\Omega}}')\exp[i\Psi_d(\mathbf{r},\hat{\mathbf{\Omega}},\hat{\mathbf{\Omega}}',t,\tau)]I(\mathbf{r},\hat{\mathbf{\Omega}}',t,\tau)d\Omega', \tag{5.29}$$

where $\{\hat{\mathbf{\Omega}}\cdot\partial/\partial\mathbf{r}+\mu_t-\tilde{\Lambda}_n(\mathbf{r},t,\tau)\}\ I_0(\mathbf{r},\hat{\mathbf{\Omega}},t,\tau)\approx 0$ in the region where the Green's function given by Eq. (5.2) is valid. Also, after several extinction lengths from the source, the coherent time-varying specific intensity becomes negligible in respect to $I(\mathbf{r},\hat{\mathbf{\Omega}},t,\tau)$.

Compared to the CTE where the optical scatterers are undergoing Brownian motion,[27,55] in Eq. (5.29) we have a similar term $\Psi_d(\,)$ that is due to the ultrasound-induced movement of the optical scatterers, and a new term $\tilde{\Lambda}_n(\,)$.

The time-varying specific intensity $I(\mathbf{r},\hat{\mathbf{\Omega}},t,\tau)$ in the case of ultrasound modulation depends on both time t and time increment τ. Of most practical interest is to find the power spectral density of the ultrasound-modulated light, which implies the availability of an analytical solution for $I(\mathbf{r},\hat{\mathbf{\Omega}},\tau)$. Unfortunately, due to correlations among the ultrasound-induced optical phase increments, it is difficult to create a simple equation for $I(\mathbf{r},\hat{\mathbf{\Omega}},\tau)$ based on Eqs. (5.29) and (5.22). However, it should be possible to adapt the numerical codes developed for the Boltzmann equation to calculate the power spectral density of the ultrasound-modulated light based on Eq. (5.29). Also, in the diffusion regime, and for ultrasound wavelengths which satisfy $k_a l_{tr}\gg 1$, it is possible to significantly simplify the expression for $I(\mathbf{r},\hat{\mathbf{\Omega}},\tau)$ by pre-averaging[55] the ultrasound-induced optical phase increments in Eq. (5.23). A formal derivation of the temporal correlation diffusion equation for ultrasound-modulated light will be presented elsewhere.[59]

4. Monte Carlo Simulation

We developed a Monte Carlo (MC) algorithm which can, based on Eq. (5.23), calculate the power spectrum of ultrasound-modulated light when a focused ultrasound field is present in an optically scattering medium with a heterogeneous distribution of optical parameters. The optically scattering medium is divided along the Cartesian axes into cells, which are enumerated by vectors $\mathbf{n}$ with integer coordinates $\{n_x, n_y, n_z\}$ assigned to each cell. We also assign an individual value of the optical absorption and the scattering coefficient to each cell, as well as the scattering anisotropy factor (average cosine of the scattering angle), where a Henyey-Greenstein scattering phase function is assumed.[29] We further assign to each cell an average ultrasound propagation direction $\hat{\mathbf{\Omega}}_{a,\mathbf{n}}$, pressure amplitude $P_{0,\mathbf{n}}$, and phase $\phi_{\mathbf{n}}$, assuming that the dimensions of the cell are much smaller than the ultrasound wavelength so that within each cell, the ultrasound field can be well approximated with $P_{\mathbf{n}}(t) = P_{0,\mathbf{n}} \cos(\omega_a t + \phi_{\mathbf{n}})$. The procedure for propagation of the photon packets in the MC is analogous to the previously described algorithms,[19,28] with the only difference being that at each crossing of the cell boundaries, the remaining length of the photon free path is adjusted in accordance with the extinction coefficient within the cell that the photon packet is entering. This simulation approach should be sufficiently accurate for calculation of the power spectral density in thick scattering samples, when the light is completely diffused. In other cases, more rigorous approach could be used, which takes into account contributions from all the scattering orders.[60,61] The trajectory of each photon consists of many small steps, which are determined by all of the scattering events and cell boundaries along the way. For each small photon step of length l_i within cell $\mathbf{m}$, the optical phase incre-

ment that is due to ultrasound-induced index of refraction changes is calculated as $\Delta\varphi_{n,i} = k_0 n_0 l_i P_{\mathbf{m}}(t)\eta/(\rho v_a^2)$, and we express it as

$$\Delta\varphi_{n,i} = P_{n,cos,i}\cos(\omega_a t) + P_{n,sin,i}\sin(\omega_a t). \tag{5.30}$$

The terms $P_{n,cos,i}$ and $P_{n,sin,i}$ in Eq. (5.30) are calculated as

$$P_{n,cos,i} = k_0 n_0 l_i \eta(\rho v_a^2)^{-1} P_{0,\mathbf{m}}\cos(\phi_{\mathbf{m}}) \tag{5.31a}$$

$$P_{n,sin,i} = -k_0 n_0 l_i \eta(\rho v_a^2)^{-1} P_{0,\mathbf{m}}\sin(\phi_{\mathbf{m}}). \tag{5.31b}$$

Similarly, for each scattering event j within cell $\mathbf{n}$, the optical phase increment due to ultrasound-induced scatterer displacement is calculated as $\Delta\varphi_{d,j} = k_0 n_0 (k_a \rho v_a^2)^{-1}\hat{\mathbf{\Omega}}_{a,\mathbf{n}} \cdot (\hat{\mathbf{\Omega}}_{inc} - \hat{\mathbf{\Omega}}_{sc}) P_{0,\mathbf{n}}\sin(\omega_a t + \phi_{\mathbf{n}})$, and we express it as

$$\Delta\varphi_{d,j} = P_{d,cos,j}\cos(\omega_a t) + P_{d,sin,j}\sin(\omega_a t). \tag{5.32}$$

In Eq. (5.32), we use $P_{d,cos,j} = k_0 n_0 (k_a \rho v_a^2)^{-1}\hat{\mathbf{\Omega}}_{a,\mathbf{n}} \cdot (\hat{\mathbf{\Omega}}_{inc} - \hat{\mathbf{\Omega}}_{sc}) P_{0,\mathbf{n}}\sin(\phi_{\mathbf{n}})$, $P_{d,sin,j} = k_0 n_0 (k_a \rho v_a^2)^{-1}\hat{\mathbf{\Omega}}_{a,\mathbf{n}} \cdot (\hat{\mathbf{\Omega}}_{inc} - \hat{\mathbf{\Omega}}_{sc}) P_{0,\mathbf{n}}\cos(\phi_{\mathbf{n}})$. $\hat{\mathbf{\Omega}}_{inc}$ and $\hat{\mathbf{\Omega}}_{sc}$ are incident and scattered photon directions, respectively, and we assume for simplicity that the optical scatterers are following the ultrasound-induced movement of the surrounding medium in both amplitude and phase.

At each scattering event, the total ultrasound-induced phase of the photon packet accumulated up to this point is $\Delta\varphi = A\cos(\omega_a t + \phi)$, where $A\cos(\phi) = \sum_i P_{n,cos,i} + \sum_j P_{d,cos,j}$, $A\sin(\phi) = -\sum_i P_{n,sin,i} - \sum_j P_{d,sin,j}$, and i and j count all of the previous steps and scattering events of the photon. The expression for the temporal autocorrelation of the photon packet is given by

$$G(t,\tau) = \exp\{iA[\cos(\omega_a t + \phi) - \cos(\omega_a(t+\tau) + \phi)]\}. \tag{5.33}$$

We use $\exp[iA\cos(\phi)] = \sum_{m=-\infty}^{+\infty} i^m J_m(A)\exp[im\phi]$ to further develop Eq. (5.33), where $J_m(A)$ is the Bessel function of the first kind of order m. We arrive then at the expression

$$\frac{\omega_a}{2\pi}\int_0^{2\pi/\omega_a} G(t,\tau)dt = J_0^2(A) + \sum_{m=1}^{+\infty} 2J_m^2(A)\cos(m\omega_a\tau). \tag{5.34}$$

In the simulation, quantity A is calculated at each scattering event, and the values of $\Delta M_0(\mathbf{n}) = J_0^2(A)\Delta W$ and $\Delta M_1(\mathbf{n}) = 2J_1^2(A)\Delta W$ are obtained, where $\Delta W = W\mu_a/\mu_t$, and W is the current weight of a photon at the scattering event which happened in cell $\mathbf{n}$. At the end of the simulation of all of the photon packets, sums $M_0(\mathbf{n}) = \sum \Delta M_0(\mathbf{n})$ and $M_1(\mathbf{n}) = \sum \Delta M_1(\mathbf{n})$ of the increments for all of the scattering events that happened in cell $\mathbf{n}$ are proportional to the amplitudes of the zero and the first harmonics, respectively, of the power spectrum of the ultrasound-modulated light.

The sample in our simulation is an optically scattering slab infinitely wide in the Y and Z directions, with a thickness of $L = 20$ mm along the X axis. We use $\mu_a = 0.1$ cm^{-1} and $\mu_s = 10$ cm^{-1} in the entire slab, which are representative of soft biological tissue for visible and near-infrared light, and, for simplicity, assume isotropic scattering. A focused ultrasound beam with a monochromatic frequency of 1 MHz, focal length of 40 mm, and aperture diameter of 25.4 mm is positioned parallel to the Z axis within the slab and spaced at equal distances from the slab surfaces. The focal spot of the transducer is at $\{x, y, z\} = \{10$ mm, 0 mm, 0 mm$\}$, and the pressure amplitude at the focus is $P_0 = 10^5$ Pa. A pencil light source with a wavelength of 532 nm irradiates the scattering slab from the $x < 0$ half space, at position $\{x, y, z\} = \{0$ mm, 10 mm, 0 mm$\}$. We assume the same optical index of refraction $n_0 = 1.33$ in whole space, a mass density of the medium $\rho = 10^3$ kgm^{-3}, an ultrasound velocity $v_a = 1480$ ms^{-1}, and an elasto-optical coefficient of water at room

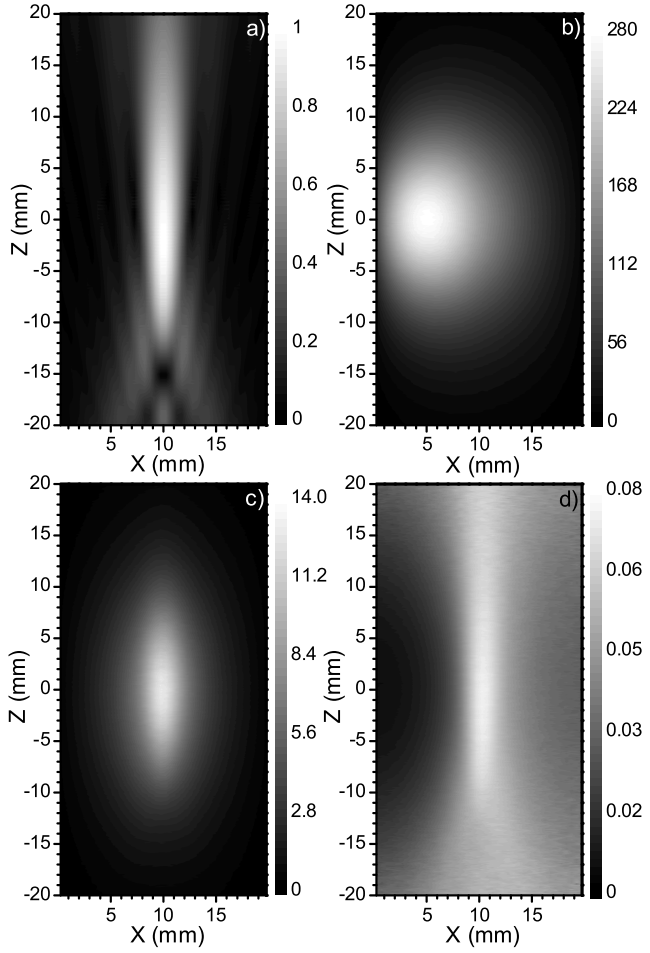

Fig. 5.1. Monte Carlo simulation of light modulated by a focused ultrasound beam. The results are presented for an optically scattering slab in a plane defined by $y = 0$ mm, which contains the axis of the ultrasound beam. (a) Distribution of the ultrasound pressure in 10^5 Pa. (b) Distribution of the amplitude of the zero harmonic $[M_0(\mathbf{n})]$ of the power spectrum of ultrasound-modulated light in arbitrary units. (c) Distribution of the amplitude of the first harmonic $[M_1(\mathbf{n})]$ of the power spectrum of ultrasound-modulated light in arbitrary units. (d) Distribution of the modulation depth calculated as $M_1(\mathbf{n})/M_0(\mathbf{n})$.

temperature $\eta = 0.32$. The distributions of the ultrasound pressure and phase are calculated with publicly available software Field II,[62] and the ultrasound propagation directions are subsequently obtained by taking the gradient of the ultrasound phase. The cell grid is centered around the focal spot of the transducer, and it is 10 cm wide in both the Y and Z directions in order to minimize the error of the simulation within the central region. The dimensions of the cells are $\Delta x = 0.5$ mm, $\Delta y = 0.5$ mm, and $\Delta z = 0.1$ mm, such that the change in the ultrasound phase within the cell is small.

Figure 5.1(a) presents the ultrasound pressure distribution within the slab in plane $y = 0$ mm, which contains the axis of the ultrasound beam. In Figs. 5.1(b) and 5.1(c), we plot the amplitudes of the zero $[M_0(\mathbf{n})]$ and the first $[M_1(\mathbf{n})]$ harmonics of the power spectrum of the ultrasound-modulated light in the same plane ($y = 0$ mm). Since the light source is at $y = 10$ mm, the maximum of the distribution $M_0(\mathbf{n})$ in plane $y = 0$ mm is not at the point of light incidence ($x = 0$ mm). Figure 5.1(c) shows that the distribution $M_1(\mathbf{n})$ follows the profile of the ultrasound focal zone, which confirms the assumption that we used to explain UOT experimental results. Finally, in Fig. 5.1(d) we plot the modulation depth in the $y = 0$ mm plane, calculated as $M_1(\mathbf{n})/M_0(\mathbf{n})$. The modulation depth peaks at 8 % at the ultrasound focus. The value of the modulation depth is significantly lower at places closer to the point of light incidence, due to the very high intensity of the unmodulated light. On both sides of the slab, the modulation depth in the $y = 0$ mm plane increases at points more distant from the light source, due to the increased probability of the light interacting with the ultrasound along the way. However, the total amount of available light at these points is low. In finding the optimal position for the highest signal-to-noise ratio of the measurement, we should consider both the modulation depth and the total available optical intensity.

5. Conclusion

In conclusion, based on the ladder approximation of the Bethe-Salpeter equation, we have developed integral and differential forms of the CTE for ultrasound-modulated light in optically turbid media. We have also developed a Monte Carlo algorithm which can be used to calculate the power spectrum of the ultrasound-modulated light in optically turbid media, with heterogeneous distributions of optical parameters and focused ultrasound fields. The derivations are valid within the weak-scattering approximation, the medical ultrasound frequency range and moderate ultrasound pressures. We expect that the CTE will help to better model UOT experiments for estimations of sensitivity, resolution, and signal-to-noise ratios. Further development of the theory is necessary to address tightly focused ultrasound fields with very high ultrasound pressures.

CHAPTER VI
CORRELATION TRANSFER AND DIFFUSION OF ULTRASOUND-MODULATED MULTIPLY SCATTERED LIGHT

1. Introduction

In this chapter, we formally derive a temporal correlation transfer equation (CTE) and a temporal correlation diffusion equation (CDE) for the ultrasound-modulated multiply scattered light for isotropic optical scattering and $k_a l_{tr} \gg 1$, where $k_a = 2\pi/\lambda_a$. These equations can be used to obtain both analytical and numerical solutions for the distribution of the modulated light intensity in scattering samples with heterogeneous optical parameters and a nonuniform ultrasound field. In addition, simple forms of CTE and CDE benefit from all of the mathematical tools available for the radiative transfer and diffusion equations. A derivation of a more complex CTE based on the ladder approximation of the Bethe-Salpeter equation is already presented in the preceding chapter.

We first confirm the agreement between the analytical solution for the scattering slab filled with ultrasound based on the previous DWS approach and the simple solution of CDE. We further provide both analytical and Monte Carlo solutions for the more practical configuration where a cylinder of ultrasound insonifies a scattering slab. Finally, the experimental results for a similar configuration are compared with the calculation based on the finite difference model of CDE.

2. Derivation of Correlation Diffusion Equation

We consider the interaction of ultrasound with monochromatic light that diffuses through the medium with discrete, uncorrelated optical scatterers. We further assume independent scattering and neglect the polarization for simplicity. Under the weak scattering approximation that the optical mean free path is much greater than the optical wavelength, transfer of light can be described by ladder diagrams.[46] In our case, this also involves calculation of the optical phase increments due to both mechanisms of ultrasound modulation along the optical paths. The phase increments are generally correlated if they originate at positions separated by less than l_{tr} or λ_a,[45] which creates difficulties in the derivation of a simple transfer-like equation for the temporal correlation of ultrasound-modulated light.[63]

However, a simple form of CTE can be obtained when $k_a l_{tr} \gg 1$. At scales larger than l_{tr}, the effect of ultrasound modulation can be calculated by assuming isotropic scattering, where l_{tr} is used instead of the mean-free path.[19,20,45] The condition $k_a l_{tr} \gg 1$ then ensures that the ultrasound-induced optical phase increments associated with the different scattering events are independent. The only correlation between phase increments which then exists is between (1) the phase increment due to index of refraction changes along the free path and (2) the phase increments due to displacements of these two scatterers along the free path.[45] This allows for a simple form of the CTE that is valid on the scale comparable with l_{tr}. In soft biological tissues, $l_{tr} \approx 1$ mm for visible and near infrared light, and $k_a l_{tr} > 10$ for ultrasound frequencies greater than 2.4 MHz.

Consider optical scatterers at resting positions $\mathbf{r}_a$ and $\mathbf{r}_b$, and assume that the ultrasound field in volumes of $\sim l_{tr}$ can be locally approximated as a plane wave

$P(\mathbf{r},t) = P_0\cos(\omega_a t - \mathbf{k}_a\cdot\mathbf{r}+\phi)$, where $\mathbf{k}_a = k_a\hat{\mathbf{\Omega}}_a$, and P_0, ω_a, $\hat{\mathbf{\Omega}}_a$, and ϕ are the pressure amplitude, angular frequency, propagation direction of the ultrasound ($|\hat{\mathbf{\Omega}}_a| = 1$), and local initial phase, respectively. For moderate ultrasound pressures, the optical index of refraction experiences a small perturbation approximated with $n(\mathbf{r},t) = n_0[1+\eta P(\mathbf{r},t)/(\rho v_a^2)]$, where ρ is the fluid density, v_a is the ultrasound speed, and η is the elasto-optical coefficient. We obtain the increment $\delta = k_0 n_0|\mathbf{r}_b - \mathbf{r}_a| + \varphi_{a,b}(t)$ of the optical phase along the free path between $\mathbf{r}_a$ and $\mathbf{r}_b$ by integrating the $k_0 n(\mathbf{r},t)$ along the path, where

$$\varphi_{a,b}(t) = k_0 n_0\left[\hat{\mathbf{\Omega}}\cdot[\mathbf{e}_b(t)-\mathbf{e}_a(t)] + \frac{\eta}{\rho v_a^2}\int_{\mathbf{r}_a}^{\mathbf{r}_b} P(\mathbf{r},t)dr\right], \tag{6.1}$$

and k_0 is the optical wave number in vacuum. In Eq. (6.1), we approximate the distance between scatterers with $|\mathbf{r}_b-\mathbf{r}_a| + \hat{\mathbf{\Omega}}\cdot[\mathbf{e}_b(t)-\mathbf{e}_a(t)]$, where $\hat{\mathbf{\Omega}}|\mathbf{r}_b-\mathbf{r}_a| = \mathbf{r}_b-\mathbf{r}_a$, $\mathbf{e}_s(t) = \hat{\mathbf{\Omega}}_a P_0 S_a/(k_a\rho v_a^2)\sin(\omega_a t - \mathbf{k}_a\cdot\mathbf{r}_s+\phi-\phi_a)$ is the ultrasound-induced displacement of the optical scatterer at $\mathbf{r}_s$ ($s = a, b$), and S_a and ϕ_a are, respectively, deviations of the amplitude and phase of the scatterer from the motion of the surrounding fluid.[45] The second term in Eq. (6.1) is the phase increment due to the ultrasound-induced index of refraction changes. The scatterer displacement in the integration limits is neglected since $|\mathbf{e}_s(t)| \ll l_{tr}$ at the relatively high ultrasound frequencies and moderate pressures which are assumed in this calculation. However, at ultrasound frequencies greater than several tens of MHz when $P_0 > 10^5$ Pa, integration along straight lines might be inappropriate due to optical wavefront distortion.[45]

We assume that the electrical field mutual coherence function $\Gamma(\mathbf{r}_{b'},t;\mathbf{r}_{b''},t+\tau) = \langle E(\mathbf{r}_{b'},t)E^*(\mathbf{r}_{b''},t+\tau)\rangle$ for two closely spaced points $\mathbf{r}_{b'}$ and $\mathbf{r}_{b''}$ is quasi-uniform, and we relate it to the time-varying specific intensity $I(\mathbf{r}_b,\hat{\mathbf{\Omega}},t,\tau)$ by a spatial Fourier transform over the difference variable $\mathbf{r}_{b'}-\mathbf{r}_{b''}$ in the center-of-gravity coordinate system,[27,47,55] where $\mathbf{r}_b = (\mathbf{r}_{b'}+\mathbf{r}_{b''})/2$, and $\langle\,\rangle$ denotes the ensemble averaging. Let

$E(\mathbf{r}_a, t)$ be the partial wave scattered at $\mathbf{r}_a$ toward $\mathbf{r}_b$. For isotropic scattering and $k_a l_{tr} \gg 1$, there is no correlation between $\varphi_{a,b}(t)$ and the other ultrasound-induced optical phase increments accumulated in $E(\mathbf{r}_a, t)$, and $I(\mathbf{r}_b, \hat{\mathbf{\Omega}}, t, \tau)$ is independent of time t. The phase term $\Delta\varphi = \varphi_{a,b}(t+\tau) - \varphi_{a,b}(t)$ is given by

$$\begin{aligned} \Delta\varphi &= 2\Lambda \sin\left(\frac{1}{2}\omega_a \tau\right) \sin\left(\mathbf{k}_a \cdot \frac{\mathbf{r}_b - \mathbf{r}_a}{2}\right) \\ &\times \left[S_a \hat{\mathbf{\Omega}} \cdot \hat{\mathbf{\Omega}}_a \sin\left(\omega_a t + \frac{1}{2}\omega_a \tau - \mathbf{k}_a \cdot \frac{\mathbf{r}_a + \mathbf{r}_b}{2} + \phi - \phi_a\right) \right. \\ &\left. - \frac{\eta}{\hat{\mathbf{\Omega}} \cdot \hat{\mathbf{\Omega}}_a} \sin\left(\omega_a t + \frac{1}{2}\omega_a \tau - \mathbf{k}_a \cdot \frac{\mathbf{r}_a + \mathbf{r}_b}{2} + \phi\right) \right], \end{aligned} \tag{6.2}$$

where $\Lambda = 2k_0 n_0 P_0/(k_a \rho v_a^2)$. For $l_{tr} \approx 1$ mm and $P_0 < 10^5$ Pa, the phase term $\Delta\varphi$ satisfies $\Delta\varphi \ll 1$, and we approximate $\exp(i\Delta\varphi)$ with $1 - |\mathbf{r}_b - \mathbf{r}_a| l_{tr}^{-1} \langle \Delta\varphi^2 \rangle_{l_{tr}}/2$. For isotropic scattering, $l_{tr}^{-1} = \mu_t$ and $\mu_t = \mu_s + \mu_a$, where μ_t, μ_s, and μ_a are the optical extinction, scattering, and absorption coefficients, respectively. $\langle \Delta\varphi^2 \rangle_{l_{tr}}$ is the average value of $\Delta\varphi^2$ in volume $V_0 \sim l_{tr}^3$ per mean optical free path. The average of $\Delta\varphi^2$ over the center-of-gravity coordinate $(\mathbf{r}_a + \mathbf{r}_b)/2$ in volume V_0 is given by

$$\begin{aligned} \langle \Delta\varphi^2 \rangle_{V_0} &= 2\Lambda^2 \sin^2\left(\frac{1}{2}\omega_a \tau\right) \sin^2\left(\mathbf{k}_a \cdot \frac{\mathbf{r}_b - \mathbf{r}_a}{2}\right) \\ &\times \left[S_a^2 \left(\hat{\mathbf{\Omega}} \cdot \hat{\mathbf{\Omega}}_a\right)^2 + \frac{\eta^2}{\left(\hat{\mathbf{\Omega}} \cdot \hat{\mathbf{\Omega}}_a\right)^2} - 2 S_a \eta \cos(\phi_a) \right], \end{aligned} \tag{6.3}$$

and from the probability density of the free path l, which is $l_{tr}^{-1} \exp[-l/l_{tr}]$, we obtain

$$\begin{aligned} \langle \Delta\varphi^2 \rangle_{l_{tr}} &= \Lambda^2 \sin^2\left(\frac{1}{2}\omega_a \tau\right) \frac{(l_{tr} \mathbf{k}_a \cdot \hat{\mathbf{\Omega}})^2}{1 + (l_{tr} \mathbf{k}_a \cdot \hat{\mathbf{\Omega}})^2} \\ &\times \left[S_a^2 (\hat{\mathbf{\Omega}} \cdot \hat{\mathbf{\Omega}}_a)^2 + \frac{\eta^2}{(\hat{\mathbf{\Omega}} \cdot \hat{\mathbf{\Omega}}_a)^2} - 2\eta S_a \cos(\phi_a) \right]. \end{aligned} \tag{6.4}$$

where $\Lambda = 2k_0 n_0 P_0/(k_a \rho v_a^2)$. The three terms in square brackets in Eq. (6.4) are related to the two mechanisms of modulation and the correlation between the

phase increments produced by these mechanisms along the same free path, respectively.[45] The increment of the intensity $I(\mathbf{r}_b, \hat{\mathbf{\Omega}}, \tau)$ that is due to the contribution of $I(\mathbf{r}_a, \hat{\mathbf{\Omega}}', \tau)$, which is scattered at $\mathbf{r}_a$ into direction $\hat{\mathbf{\Omega}}$, is equal to $\Delta I = I(\mathbf{r}_a, \hat{\mathbf{\Omega}}', \tau) \exp(-\mu_t |\mathbf{r}_b - \mathbf{r}_a|)[1 - |\mathbf{r}_b - \mathbf{r}_a| \mu_t \langle \Delta\varphi^2 \rangle_{l_{tr}}/2]$. By accumulating all of the increments along the $\hat{\mathbf{\Omega}}$ direction starting from some distant $\mathbf{r}_0$, we have

$$I(\mathbf{r}_b,\hat{\mathbf{\Omega}},\tau) = I_0(\mathbf{r}_b,\hat{\mathbf{\Omega}},\tau) + \int_{\mathbf{r}_0}^{\mathbf{r}_b} \int_{4\pi} \mu_s p(\hat{\mathbf{\Omega}},\hat{\mathbf{\Omega}}') \Delta I d|\mathbf{r}_b - \mathbf{r}_a| d\hat{\mathbf{\Omega}}', \tag{6.5}$$

where $I_0(\mathbf{r}_b, \hat{\mathbf{\Omega}}, \tau)$ is due to the unscattered field.[27] After applying $\hat{\mathbf{\Omega}} \cdot \nabla$ to Eq. (6.5), we obtain the CTE as

$$\begin{aligned} \hat{\mathbf{\Omega}} \cdot \nabla I(\mathbf{r}, \hat{\mathbf{\Omega}}, \tau) &= -(\mu_a + \mu_s) I(\mathbf{r}, \hat{\mathbf{\Omega}}, \tau) + S(\mathbf{r}, \hat{\mathbf{\Omega}}) \\ &\quad + \mu_s \int_{4\pi} p(\hat{\mathbf{\Omega}}, \hat{\mathbf{\Omega}}') [1 - \frac{1}{2} \langle \Delta\varphi^2 \rangle_{l_{tr}}] I(\mathbf{r}, \hat{\mathbf{\Omega}}', \tau) d\Omega'. \end{aligned} \tag{6.6}$$

In Eq. (6.6), $p(\hat{\mathbf{\Omega}}, \hat{\mathbf{\Omega}}') = 1/(4\pi)$ is the isotropic scattering phase function, and $S(\mathbf{r}, \hat{\mathbf{\Omega}})$ is the monochromatic source term. Like in the case of Brownian motion,[55] this equation can be obtained by pre-averaging the phase increments in a more rigorously derived CTE.[63]

To obtain the CDE, we apply the standard approximation $I(\mathbf{r}, \hat{\mathbf{\Omega}}, \tau) \approx [\Phi(\mathbf{r}, \tau) + 3\hat{\mathbf{\Omega}} \cdot \mathbf{J}(\mathbf{r}, \tau)]/(4\pi)$ in Eq. (6.6). $\Phi(\mathbf{r}, \tau)$ is actually the temporal field autocorrelation function related to the optical intensity spectrum by the temporal Fourier transform. The CDE is

$$\nabla \cdot [D \nabla \Phi(\mathbf{r}, \tau)] - [\mu_a + \mu_s \hat{\varphi}(\tau)] \Phi(\mathbf{r}, \tau) + S_0(\mathbf{r}) = 0. \tag{6.7}$$

In Eq. (6.7), $D = (3\mu_s)^{-1}$, and $\hat{\varphi}(\tau)$ is given by

$$\hat{\varphi}(\tau) = \frac{1}{2} \Lambda^2 \sin^2 \left(\frac{1}{2} \omega_a \tau \right) \left[\eta^2 (k_a l_{tr}) \tan^{-1}(k_a l_{tr}) + \frac{1}{3} S_a^2 - 2\eta S_a \cos(\phi_a) \right]. \tag{6.8}$$

Brownian motion could also be considered by including $2D_B k_0^2 \mu_s \tau$ in addition to $\mu_s \hat{\varphi}(\tau)$ in Eq. (6.7), where D_B is an appropriate diffusion constant.[64]

3. Results

In infinite media, the solution of Eq. (6.7) for monochromatic point source S_0 at the origin is

$$\Phi(\mathbf{r},\tau) = S_0 (4\pi D)^{-1} \exp(-r\sqrt{[\mu_a + \mu_s \hat{\varphi}(\tau)]/D})/r, \tag{6.9}$$

and it can be used to analytically study various configurations of ultrasound within the scattering media. In finite media the boundary conditions are identical to those in the diffusion equation used in radiative transfer.[65] For matched optical properties, continuity requires that $\Phi(\mathbf{r},\tau)$ and $D\partial\Phi(\mathbf{r},\tau)/\partial n$ are constant across the boundary, where $\hat{\mathbf{n}}$ is a unit vector perpendicular to the boundary. For a scattering half space ($z > 0$) filled with ultrasound and irradiated by a pencil source from the free space, the boundary condition is $\Phi(\mathbf{r},\tau) = 2D\partial\Phi(\mathbf{r},\tau)/\partial z$, which leads to the extrapolated zero boundary position at $z = -2D$.

Eq. (6.7) can be solved analogously to the diffusion equation of fluence rate[26] for $\Phi(\tau)$, which is $\Phi(\mathbf{r},\tau)$ integrated over the whole transmission surface of the scattering slab of thickness L filled with ultrasound and irradiated with the pencil monochromatic source S_0

$$\Phi(\tau) = \frac{3S_0}{4\pi} \frac{\sinh[(z_0 + 2D)\sqrt{(\mu_a + \mu_s \hat{\varphi}(\tau))/D}]}{\sinh[(L + 4D)\sqrt{(\mu_a + \mu_s \hat{\varphi}(\tau))/D}]}. \tag{6.10}$$

In Eq. (6.10), $z_0 = 1/\mu_s$ is the depth of the converted isotropic source and the solution is, up to the normalization constant, identical to the one obtained earlier.[18,20,45]

Next, we consider an infinitely wide scattering slab, with surface planes at $x = 0$

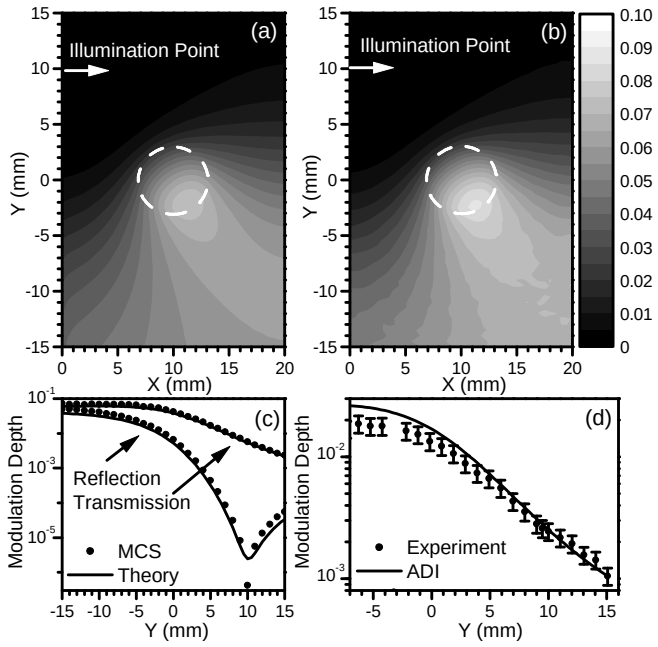

Fig. 6.1. Modulation depth (MD) of the ultrasound-modulated light for an ultrasound cylinder in a scattering slab. (a) and (b) MD obtained analytically and with MCS, respectively, at $z = 0$ mm. The white circles mark the ultrasound cross section. (c) MD obtained analytically and with MCS for $z = 0$ mm at the transmission ($x = 20$ mm) and reflection ($x = 0$ mm) planes. (d) MD measured experimentally and calculated using the ADI for $z = 0$ mm at the transmission plane.

mm and $x = 20$ mm. We assume $v_a = 1480$ m/s, $\rho = 10^3$ kg/m^3, $\eta = 0.32$, $\mu_a = 0.1$ cm^{-1}, isotropic scattering with $\mu_s = 10$ cm^{-1}, $n_0 = 1.33$ in whole space, $S_a = 1$, and $\phi_a = 0$, as typical values for soft biological tissues and visible and near-infrared light.[45] A cylinder of radius $a = 3.175$ mm, infinitely long in the Z direction, with an axis at $(x, y) = (10\text{ mm}, 0\text{ mm})$ is filled with a 5 MHz ultrasound of pressure amplitude $P_0 = 10^5$ Pa traveling in the Z direction. A pencil light source S_0 of wavelength $\lambda_0 = 532$ nm irradiates the slab along the X direction at $(x, y, z) = (0\text{ mm}, 10\text{ mm}, 0\text{ mm})$. Eq. (6.7) has solutions $\Phi_{inc}(\mathbf{r}_d, \tau)$, $\Phi_{sc}(\mathbf{r}_d, \tau)$, and $\Phi_{in}(\mathbf{r}_d, \tau)$, which are for the autocorrelation functions incident from the source, scattered from the cylinder, and inside the cylinder, respectively.[66] If the cylinder axis is at the origin, then

$$\Phi_{\{..\}}(\mathbf{r}_d, \tau) = \sum_{n=0}^{+\infty} \cos(n\phi_d) \int_0^{+\infty} \cos(pz_d) \Psi_{\{..\}}(p) dp, \tag{6.11}$$

where $\Psi_{inc}(p) = H_n(x_>) I_n(x_<)$, $\Psi_{sc}(p) = B_n(p) K_n(x)$, and $\Psi_{in}(p) = C_n(p) I_n(y)$; $\mathbf{r}_s = (\rho_s, \phi_s, z_s)$ and $\mathbf{r}_d = (\rho_d, \phi_d, z_d)$ are positions of the point source and the detector in the cylindrical coordinates, and I_n and K_n are modified Bessel functions of the first and second kind, respectively; $x_{\lessgtr} = \rho_{\lessgtr}\sqrt{p^2 - k_{out}^2}$; $\rho_{\lessgtr} = \min(\max)[\rho_s, \rho_d]$; $x = \rho_d\sqrt{p^2 - k_{out}^2}$; $y = \rho_d\sqrt{p^2 - k_{in}^2}$; $k_{in}^2 = -[\mu_a + \mu_s\hat{\varphi}(\tau)]/D$; $k_{out}^2 = -\mu_a/D$; B_n and C_n are given by

$$B_n(p) = -H_n(z_b) \frac{x_b I_n'(x_b) I_n(y_b) - y_b I_n'(y_b) I_n(x_b)}{x_b K_n'(x_b) I_n(y_b) - y_b I_n'(y_b) K_n(x_b)}, \tag{6.12a}$$

$$C_n(p) = -H_n(z_b) \frac{x_b I_n'(x_b) K_n(x_b) - x_b K_n'(x_b) I_n(x_b)}{x_b K_n'(x_b) I_n(y_b) - y_b I_n'(y_b) K_n(x_b)}, \tag{6.12b}$$

where $H_n(z_b) = [(\text{sgn}(n) + 1) S_0 K_n(z_b)]/(2\pi^2 D)$, $x_b = a\sqrt{p^2 - k_{out}^2}$, $y_b = a\sqrt{p^2 - k_{in}^2}$, $z_b = \rho_s\sqrt{p^2 - k_{out}^2}$, and $\text{sgn}(n)$ is the sign function. We use Eq. (6.11) to obtain values for the modulation depth (MD), defined as the amplitude ratio of the first to

the zeroth harmonics of the modulated light [Fig. 6.1(a)]. Three pairs of independent cylinder images[26] are used to satisfy the boundary conditions. The analytical solution agrees with the Monte Carlo solution (MCS),[19,20] modified for the cylindrical object [Fig. 6.1(b)]. In Fig. 6.1(c), the two solutions are compared along the Y direction on the slab surfaces. The MD is higher away from the source, in the shadow of the cylinder, due to the counteracting contributions of the modulated and unmodulated light.

In the experiment, we immersed in water a wide, 20 mm thick slab, with $\mu_a = 0.1$ cm^{-1} and reduced scattering coefficient $\mu_s = 10$ cm^{-1}, made of agar, Lyposine 20%, and Trypan Blue dye. A flat ultrasound transducer with a 5-MHz frequency and a 3.175-mm radius was positioned, as in the theoretical model, with a surface at $z = -50$ mm. A 10^5 Pa pressure amplitude was measured at $z = 0$ mm with a needle hydrophone on the acoustic axis. We used a previously described setup[31] to measure the modulation depth at the transmission plane of the slab. The measured data [Fig. 6.1(d)] were in agreement with the numerical calculation, which used an Alternating Direction Implicit algorithm (ADI) adapted for Eq. (6.7). For the ADI, the nonuniform ultrasound field was calculated using the program FieldII,[62] where transducer apodization and amplitude were adjusted to match the parameters of the real transducer measured by the hydrophone. The cell size was set to 1/3 mm in order to appropriately model the boundary conditions.

4. Conclusion

In conclusion, we derived the CTE and the CDE for ultrasound-modulated light which is valid for optical and ultrasound spatial inhomogeneities on the order of

l_{tr}, for moderate ultrasound pressures and frequencies satisfying $k_a l_{tr} \gg 1$. CDE could be of use for the estimation of sensitivity and signal-to-noise ratios in UOT, where both heterogeneous ultrasound fields and optical parameters are encountered. It can be solved analytically or numerically by the many methods developed for the diffusion equation. This permitted us to obtain agreement, for the first time, between the theoretical model and the experimental measurement of the modulation depth of ultrasound-modulated light in strongly scattering media. More challenging setups with highly focused ultrasound and with very high ultrasound pressure should be the subject of further theoretical development.

CHAPTER VII
CONCLUSION

In this dissertation, ultrasound-modulated optical tomography was studied both experimentally and theoretically.

The experimental study has demonstrated the feasibility of high-resolution ultrasound-modulated optical tomography in biological tissue with an imaging depth of several millimeters. A CFPI was shown to be able to isolate ultrasonically modulated light from the background efficiently in real time. The resolution can be further improved by use of higher ultrasound frequencies. This technology can easily be integrated with conventional ultrasound imaging to provide complementary information.

In theoretical part we have extended the existing analytical model based on the diffusing-wave spectroscopy (DWS), and we have also developed the correlation transfer equation (CTE) and the correlation diffusion equation (CDE) for ultrasound-modulated multiply scattered light.

We have presented an extension of the DWS-based theory of ultrasound modulation of multiply scattered diffused light for anisotropic optical scattering. We have first developed an analytical solution for the autocorrelation function of an ultrasound-modulated electric field along a path with N scatterers when scattering is anisotropic. A further analytical solution was found for the light transmitted through a scattering slab using a plane source and a point detector. Using a Monte Carlo simulation, we verified the accuracy of the analytical solution. We also tested the similarity relation and showed that it can be used as a good approximation in the calculation of the autocorrelation function. Finally, we presented the dependence of

the maximum variation of the autocorrelation function on different ultrasonic and optical parameters. In general, increasing ultrasonic amplitude and increasing the scattering coefficient leads us to a larger maximum variation while increasing the absorption coefficient or ultrasonic frequency leads us to a smaller maximum variation. Our analytical solution is valid under the following conditions: diffusion regime transport, a small ultrasonic modulation, and when the value of $k_a l$ is not too small.

We have also presented an extension of the DWS-based theory of ultrasound modulation of multiply scattered diffused light toward the small $k_a l$ values, where a strong correlation exists between the ultrasound induced optical phase increments associated with different components of the optical path. It is shown that an approximate similarity relation is valid for this extended range of $k_a l$ values. For large $k_a l$ values, an inverse linear dependence of the modulated signal on the ultrasound frequency is a consequence of the dominating effect of the ultrasound-induced changes of the optical index of refraction, while in the low $k_a l$ range, depending on the particular values of the average number of scattering events along the pathlength, the signal has a tendency to be even inversely proportional to the square of the ultrasound frequency. The theory is also extended to account for complex scatterer movement in respect to surrounding fluid displacement. It is expected that in cases involving the commonly used ultrasound pressures in medicine, the movement of the optical scatterers in soft biological tissues should not differ significantly from the movement of the surrounding tissue. In this situation, even for large values of the $k_a l$ product, a significant correlation between the contributions of mechanism 1 and 2 exists. Finally, we derived an analytical solution for ultrasound modulation of light when the train of the ultrasound pulses traverses the scattering media. Examples of two characteristic pulse shapes with zero and nonzero central frequencies are presented in the transmission and reflection geometries. It is shown that the ultrasound frequency

dependence of the optical phase variations due to mechanisms 1 and 2 produces a nonuniform deviation of the pulse spectra, as well as decay of the modulated light power in the higher ultrasound frequency ranges.

Based on the ladder approximation of the Bethe-Salpeter equation, we have developed integral and differential forms of the CTE for ultrasound-modulated light in optically turbid medium. We have also developed a Monte Carlo algorithm which can be used to calculate the power spectrum of the ultrasound-modulated optical intensity in optically turbid media, with heterogeneous distributions of optical parameters and focused ultrasound fields. The derivations are valid within the weak scattering approximation, the medical ultrasound frequency range and moderate ultrasound pressures. We expect that the CTE will help to better model UOT experiments for estimations of sensitivity, resolution, and signal-to-noise ratios. Further development of the theory is necessary to address tightly focused ultrasound fields with very high ultrasound pressures.

We have also formally derived the CTE and the CDE for ultrasound-modulated light which is valid for optical and ultrasound spatial inhomogeneities on the order of l_{tr}, for moderate ultrasound pressures and frequencies satisfying $k_a l_{tr} \gg 1$. The CDE could be of use for the estimation of sensitivity and signal-to-noise ratios in UOT, where both heterogeneous ultrasound fields and optical parameters are encountered. It can be solved analytically or numerically by the many methods developed for the diffusion equation. This permitted us to obtain agreement, for the first time, between the theoretical model and the experimental measurement of the modulation depth of ultrasound-modulated light in strongly scattering media.

REFERENCES

1. L. V. Wang, "Ultrasound-mediated biophotonic imaging: A review of acousto-optical tomography and photo-acoustic tomography," *Dis. Markers* **19**, 123–138 (2004).

2. F. A. Marks, H. W. Tomlinson, and G. W. Brooksby, "A comprehensive approach to breast cancer detection using light: Photon localization by ultrasound modulation and tissue characterization by spectral discrimination," *Proc. SPIE* **1888**, 500–510 (1993).

3. L. V. Wang, S. L. Jacques, and X. Zhao, "Continuous-wave ultrasonic modulation of scattered laser light to image objects in turbid media," *Opt. Lett.* **20**, 629–631 (1995).

4. W. Leutz and G. Maret, "Ultrasonic modulation of multiply scattered-light," *Physica B* **204**, 14–19 (1995).

5. G. Maret and P. E. Wolf, "Multiple light-scattering from disordered media - the effect of brownian-motion of scatterers," *Z. Phys. B* **65**, 409–413 (1987).

6. D. J. Pine, D. A. Weitz, P. M. Chaikin, and E. Herbolzheimer, "Diffusing-wave spectroscopy," *Phys. Rev. Lett.* **60**, 1134–1137 (1988).

7. M. Kempe, M. Larionov, D. Zaslavsky, and A. Z. Genack, "Acousto-optic tomography with multiply scattered light," *J. Opt. Soc. Am. A* **14**, 1151–1158 (1997).

8. S. Leveque, A. C. Boccara, M. Lebec, and H. Saint-Jalmes, "Ultrasonic tagging of photon paths in scattering media: Parallel speckle modulation processing," *Opt. Lett.* **24**, 181–183 (1999).

9. J. Li and L. V. Wang, "Methods for parallel-detection-based ultrasound-modulated optical tomography," *Appl. Opt.* **41**, 2079–2084 (2002).

10. J. Li, G. Ku, and L. V. Wang, "Ultrasound-modulated optical tomography of biological tissue by use of contrast of laser speckles," *Appl. Opt.* **41**, 6030–6035 (2002).

11. L. V. Wang and G. Ku, "Frequency-swept ultrasound-modulated optical tomography of scattering media," *Opt. Lett.* **23**, 975–977 (1998).

12. G. Yao, S.-L. Jiao, and L. V. Wang, "Frequency-swept ultrasound-modulated optical tomography in biological tissue by use of parallel detection," *Opt. Lett.* **25**, 734–736 (2000).

13. A. Lev, Z. Kotler, and B. G. Sfez, "Ultrasound tagged light imaging in turbid media in a reflectance geometry," *Opt. Lett.* **25**, 378–380 (2000).

14. J. Li and L. V. Wang, "Ultrasound-modulated optical computed tomography of biological tissues," *Appl. Phys. Lett.* **84**, 1597–1599 (2004).

15. T. W. Murray, L. Sui, G. Maguluri, R. A. Roy, A. Nieva, F. Blonigen, and C. A. DiMarzio, "Detection of ultrasound modulated photons in diffuse media using the photorefractive effect," *Opt. Lett.* **29**, 2509–2511 (2004).

16. E. Granot, A. Lev, Z. Kotler, B. G. Sfez, and H. Taitelbaum, "Detection of inhomogeneities with ultrasound tagging of light," *J. Opt. Soc. Am. A* **18**, 1962–1967 (2001).

17. G. D. Mahan, W. E. Engler, J. J. Tiemann, and E. G. Uzgiris, "Ultrasonic tagging of light: Theory," *Proc. Natl. Acad. Sci. USA* **95**, 14015–14019 (1998).

18. L. V. Wang, "Mechanisms of ultrasonic modulation of multiply scattered coherent light: An analytic model," *Phys. Rev. Lett.* **87**, 043903–(1–4) (2001).

19. L. V. Wang, "Mechanisms of ultrasonic modulation of multiply scattered coherent light: A Monte Carlo model," *Opt. Lett.* **26**, 1191–1193 (2001).

20. S. Sakadzic and L. V. Wang, "Ultrasonic modulation of multiply scattered coherent light: An analytical model for anisotropically scattering media," *Phys. Rev. E* **66**, 026603–(1–9) (2002).

21. M. Hisaka, T. Sugiura, and S. Kawata, "Optical cross-sectional imaging with pulse ultrasound wave assistance," *J. Opt. Soc. Am. A - Opt. Image Sci. Vis.* **18**, 1531–1534 (2001).

22. A. Lev and B. G. Sfez, "Pulsed ultrasound-modulated light tomography," *Opt. Lett.* **28**, 1549–1551 (2003).

23. M. Gross, P. Goy, and M. Al-Koussa, "Shot-noise detection of ultrasound-tagged photons in ultrasound-modulated optical imaging," *Opt. Lett.* **28**, 2482–2484 (2003).

24. J.-P. Monchalin, "Optical detection of ultrasound at a distance using a confocal Fabry-Perot interferometer," *Appl. Phys. Lett.* **47**, 14–16 (1985).

25. "Mammalian In Vivo Ultrasonic Biological Effects," http://www.aium.org (1992).

26. M. S. Patterson, B. Chance, and B. C. Willson, "Time resolved reflectance and transmittance for the noninvasive measurement of tissue optical-properties," *Appl. Opt.* **28**, 2331–2336 (1989).

27. A. Ishimaru, *Wave Propagation and Scattering in Random Media*, Academic, New York (1978).

28. L. V. Wang, S. L. Jacques, and L.-Q. Zheng, "MCML - Monte Carlo modeling of photon transport in multi-layered tissues," *Comput. Methods Prog. Biomed.* **47**, 131–146 (1995).

29. L. G. Henyey and J. L. Greenstein, "Diffuse radiation in the Galaxy," *Astrophys. J.* **93**, 70–83 (1941).

30. D. R. Wyman, M. S. Patterson, and B. C. Wilson, "Similarity relations for the interaction parameters in radiation transport," *Appl. Opt.* **28**, 5243–5249 (1989).

31. S. Sakadzic and L. V. Wang, "High-resolution ultrasound-modulated optical tomography in biological tissues," *Opt. Lett.* **29**, 2770–2772 (2004).

32. T. W. Murray, L. Sui, G. Maguluri, R. A. Roy, A. Nieva, F. Blonigen, and C. A. DiMarzio, "Detection of ultrasound-modulated photons in diffuse media using the photorefractive effect," *Opt. Lett.* **29**, 2509–2511 (2004).

33. M. R. Maxey and J. J. Riley, "Equation of motion for a small rigid sphere in a nonuniform flow," *Phys. Fluids* **26**, 883–889 (1982).

34. E. E. Michaelidis, "Review - the transient equation of motion for particles, bubbles, and droplets," *J. Fluid. Eng.-T. ASME* **119**, 233–247 (1997).

35. A. T. Hjelmfelt and L. F. Mockros, "Motion of discrete particles in a turbulent fluid," *Appl. Sci. Res.* **16**, 149–161 (1966).

36. D. A. Siegel and A. J. Plueddemann, "The motion of a solid sphere in an oscillating flow: An evaluation of remotely sensed doppler velocity estimates in the sea," *J. Atmos. Ocean. Tech.* **8**, 296–304 (1991).

37. R. N. Zitter, "Ultrasonic diffraction of light by short acoustic pulses," *J. Acoust. Soc. Amer.* **43**, 864–870 (1968).

38. T. H. Neighbors and W. G. Mayer, "Asymmetric light-diffraction by pulsed ultrasonic-waves," *J. Acoust. Soc. Amer.* **74**, 146–152 (1983).

39. J. W. Goodman, *Statistical Optics*, John Wiley, New York (1985).

40. D. J. Pine, D. A. Weitz, G. Maret, P. E. Wolf, E. Herbolzheimer, and P. M. Chakin, *Scattering and localization of classical waves in random media*, World Scientific Publishing Co. Pte. Ltd., Singapore (1990).

41. M. Rosenbluh, M. Hoshen, I. Freund, and M. Kaveh, "Time evolution of universal optical fluctuations," *Phys. Rev. Lett.* **58**, 2754–2757 (1987).

42. B. J. Ackerson, R. L. Dougherty, N. M. Reguigui, and U. Nobbmann, "Correlation transfer: Application of radiative transfer solution methods to photon correlation problems," *J. Thermophys. Heat Tr.* **6**, 577–588 (1992).

43. A. Lev and B. Sfez, "In vivo demonstration of the ultrasound modulated light technique," *J. Opt. Soc. Am. A* **20**, 2347–2354 (2003).

44. A. Korpel, *Acousto-Optics*, Marcel Dekker, Inc., New York (1997).

45. S. Sakadzic and L. V. Wang, "Modulation of multiply scattered coherent light by ultrasonic pulses: An analytical model," *Phys. Rev. E* **72**, 036620–(1–12) (2005).

46. U. Frisch, "Wave propagation in random media", Chap. 2 in *Probabilistic Methods in Applied Mathematics*, A. T. Bharucha-Reid, Ed., pp. 75–198, Academic, New York (1968).

47. Y. N. Barabanenkov, A. G. Vinogradov, Yu. A. Kravtsov, and V. I. Tatarskii, "Application of the theory of multiple scattering of waves to the derivation of the radiation transfer equation for a statistically inhomogeneous medium," *Radiophys. Quantum Electron.* **15**, 1420–1425 (1972).

48. M. C. W. van Rossum and T. M. Nieuwenhuizen, "Multiple scattering of classical waves: Microscopy, mesoscopy, and diffusion," *Rev. Mod. Phys.* **71**, 313–371 (1999).

49. Yu. A. Kravtsov and L. A. Apresyan, "Radiative transfer: New aspects of the old theory", *Progress in Optics* **36**, 179–244 (1996).

50. S. M. Rytov, Yu. A. Kravtsov, and V. I. Tatarskii, *Principles of Statistical Radiophysics 4: Wave Propagation Through Random Media*, Springer Verlag, Berlin (1989).

51. V. L. Kuzmin and V. P. Romanov, "Coherent phenomena in light scattering from disordered systems," *Phys. Usp.* **39**, 231–260 (1996).

52. A. Ishimaru, "Correlation functions of a wave in a random distribution of stationary and moving scatterers," *Radio Sci.* **10**, 45–52 (1975).

53. M. J. Stephen, "Temporal fluctuations in wave propagation in random media," *Phys. Rev. B* **37**, 1–5 (1988).

54. F. C. MacKintosh and J. Sajeev, "Diffusing-wave spectroscopy and multiple scattering of light in random media," *Phys. Rev. B* **40**, 2383–2406 (1989).

55. R. L. Dougherty, B. J. Ackerson, N. M. Reguigui, F. Dorri-Nowkoorani, and U. Nobbmann, "Correlation transfer: Development and application," *J. Quant. Spectrosc. Radiat. Transfer* **52**, 713–727 (1994).

56. F. J. Blonigen, A. Nieva, C. A. DiMarzio, S. Manneville, L. Sui, G. Maguluri, T. W. Murray, and R. A. Roy, "Computations of the acoustically induced phase shifts of optical paths in acoustophotonic imaging with photorefractive-based detection," *Appl. Opt.* **44**, 3735–3746 (2005).

57. Y. N. Barabanenkov, "Application of the smooth-perturbation method to the solution of general equations of multiple wave-scattering theory," *Sov. Phys. JETP* **27**, 954–959 (1968).

58. S. M. Rytov, Yu. A. Kravtsov, and V. I. Tatarskii, *Principles of Statistical Radiophysics 3: Elements of Random Fields*, Springer Verlag, Berlin (1989).

59. S. Sakadzic and L. V. Wang, "Correlation diffusion equation for ultrasound-modulated multiply scattered light," submitted to *Phys. Rev. Lett.*

60. V. L. Kuzmin, I. V. Meglinski, and D. Yu. Churmakov, "Stohastic modeling of coherent phenomena in strongly inhomogeneous media," *Sov. Phys. JETP*, **101** 22–32 (2005).

61. I. V. Meglinski, V. L. Kuzmin, D. Yu. Churmakov, and D. A. Greenhalgh, "Monte Carlo simulation of coherent effects in multiple scattering," *Proc. R. Soc. A*, **461** 43–53 (2005).

62. J. A. Jensen and N. B. Svendsen, "Calculation of pressure fields from arbitrarily shaped, apodized, and excited ultrasound transducers," *IEEE Trans. Ultrason. Ferroelec. Freq. Contr.*, **39** 262–267 (1992).

63. S. Sakadzic and L. V. Wang, "Correlation transfer equation for ultrasound-modulated multiply scattered light," submitted to *Phys. Rev. E.*

64. D. A. Boas, L. E. Campbell, and A. G. Yodh, "Scattering and imaging with diffusing temporal field correlations," *Phys. Rev. Lett.* **75**, 1855–1858 (1995).

65. R. C. Haskell, L. O. Svaasand, T.-T. Tsay, T.-C. Feng, M. S. McAdams, and B. J. Tromberg, "Boundary conditions for the diffusion equation in radiative transfer," *J. Opt. Soc. Am. A* **11**, 2727–2741 (1994).

66. J. D. Jackson, *Classical Electrodynamics*, John Wiley, New York (1998).

67. O. Marichev and M. Trott, The Wolfram Functions Site http://functions.wolfram.com/05.03.06.0022.01 (1998).

APPENDIX A

DERIVATION OF THE AUTOCORRELATION FUNCTION FOR ANISOTROPICALLY SCATTERING MEDIA

The averaging over time of each term on the right side of Eq. (3.7) and over the lengths l_j of all free paths produce:

$$\left\langle \sum_{j=1}^{N} \Delta\phi_{n,j}^2(t,\tau) \right\rangle_{t,\, l_j} = \frac{(k_a l)^2}{8}(4n_0k_0A\eta)^2 \sin^2\left(\frac{1}{2}\omega_a\tau\right) \sum_{j=1}^{N} [T(x_j)+T^*(x_j)], \tag{A.1a}$$

$$\left\langle 2\sum_{j=2}^{N}\sum_{k=1}^{j-1} \Delta\phi_{n,j}\Delta\phi_{n,k} \right\rangle_{t,\, l_j} = \frac{1}{8}(k_a l)^2(4n_0k_0A\eta)^2 \sin^2\left(\frac{1}{2}\omega_a\tau\right) \times \sum_{j=2}^{N}\sum_{k=1}^{j-1} \left(\prod_{m=k}^{j} T(x_m) + \prod_{m=k}^{j} T^*(x_m) \right), \tag{A.1b}$$

$$\left\langle \sum_{j=1}^{N-1} \Delta\phi_{d,j}^2(t,\tau) \right\rangle_{t,\, l_j} = \frac{1}{2}(2n_0k_0A)^2 \sin^2\left(\frac{1}{2}\omega_a\tau\right) \sum_{j=1}^{N-1} (x_{j+1}-x_j)^2, \tag{A.1c}$$

$$\left\langle 2\sum_{j=2}^{N-1}\sum_{k=1}^{j-1} \Delta\phi_{d,j}\Delta\phi_{d,k} \right\rangle_{t,\, l_j} = \frac{1}{2}(2n_0k_0A)^2 \sin^2\left(\frac{1}{2}\omega_a\tau\right) \sum_{j=2}^{N-1}\sum_{k=1}^{j-1} \left\{ [(\hat{\mathbf{e}}_{j+1}-\hat{\mathbf{e}}_j)\cdot\hat{\mathbf{e}}_a] \times [(\hat{\mathbf{e}}_{k+1}-\hat{\mathbf{e}}_k)\cdot\hat{\mathbf{e}}_a] \left(\prod_{m=k+1}^{j} T(x_m) + \prod_{m=k+1}^{j} T^*(x_m) \right) \right\}, \tag{A.1d}$$

$$\left\langle 2\sum_{j=1}^{N}\sum_{k=1}^{N-1} \Delta\phi_{n,j}\Delta\phi_{d,k} \right\rangle_{t,\, l_j} = \frac{1}{2}k_a l(2n_0k_0A)^2\eta \sin^2\left(\frac{1}{2}\omega_a\tau\right) \times \left[\sum_{j=1}^{N-1}\sum_{k=j}^{N-1} (x_{k+1}-x_k) \left(\prod_{m=j}^{k} T(x_m) + \prod_{m=j}^{k} T^*(x_m) \right) + \sum_{j=2}^{N}\sum_{k=1}^{j-1} (x_{k+1}-x_k) \left(\prod_{m=k+1}^{j} T(x_m) + \prod_{m=k+1}^{j} T^*(x_m) \right) \right], \tag{A.1e}$$

where $T(x_m) = 1/(1 - ik_a l x_m)$, $T^*(x_m)$ is its complex conjugate, i is an imaginary unit, and we use a variable x_m to represent $\cos\theta_m$.

In order to provide averaging over all scattering directions, as a first step we expand the phase function for the polar angle $f(\cos\theta)$ over Legendre polynomials,

$$f(\cos\theta) = \sum_{m=0}^{\infty} \frac{2m+1}{2} g_m P_m(\cos\theta) \ , \qquad g_m = \int_0^{\pi} f(\cos\theta) P_m(\cos\theta) \sin\theta d\theta \ , \quad \text{(A.2)}$$

where $\cos\theta$ represents the cosine of the deflection angle.

Notice that in Eq. (A.2) $g_0 = 1$, and g_1 is equal to the scattering anisotropy factor g. In the case of Henyey-Greenstein phase function for the polar angle,[29] the value of each coefficient g_m is the mth power of the scattering anisotropy factor ($g_m = g^m$). Because the azimuth angles are uniformly distributed, the phase function for both the azimuth and polar angles are simply the polar phase function multiplied by a constant factor $(2\pi)^{-1}$.

In our case the argument of the phase function is the cosine of the angle between the incoming and outgoing photon direction $(\hat{\mathbf{e}}_j \cdot \hat{\mathbf{e}}_{j+1})$. The unity vector $\hat{\mathbf{e}}_j$ in a spherical coordinate system has a form $\hat{\mathbf{e}}_j = \cos\theta_j \hat{\mathbf{e}}_a + \sin\theta_j \cos\varphi_j \hat{\mathbf{e}}_x + \sin\theta_j \sin\varphi_j \hat{\mathbf{e}}_y$, and the argument of the phase function in this representation becomes

$$\cos\theta = \cos\theta_j \cos\theta_{j+1} + \sin\theta_j \sin\theta_{j+1} \cos(\varphi_j - \varphi_{j+1}) \ . \quad \text{(A.3)}$$

Using the identity from Ref.,[67]

$$\begin{aligned} P_n\left(xy - \sqrt{1-x^2}\sqrt{1-y^2}\cos(\alpha)\right) &= P_n(x) P_n(y) \quad \text{(A.4)} \\ &\quad + 2\sum_{k=1}^{n} \frac{(-1)^k \cos(k\alpha)(n-k)!}{(k+n)!} P_n^k(x) P_n^k(y) \ , \end{aligned}$$

and representing x, y, and α with $\cos\theta_j$, $\cos\theta_{j+1}$, and $\pi + \varphi_j - \varphi_{j+1}$, we first provide integration over all uniformly distributed azimuth angles in Eqs. (A.1). Because in Eqs. (A.1) nothing depends on the azimuth angle, all terms with associate Legendre polynomials $P_n^k(\,)$ in Eq. (A.4) vanish during the integration. Thus, for the further

integration over the polar angles, the probability density function of the photon to travel along the directions $\hat{\mathbf{e}}_1$,...,$\hat{\mathbf{e}}_N$ reduces to the function $f^{(N)}(\cos\theta_1, ..., \cos\theta_N)$, which depends only on the polar angles along the photon path:

$$f^{(N)}(\cos\theta_1, ..., \cos\theta_N) = \tilde{p}_s(\cos\theta_1) \prod_{j=1}^{N-1} f^{(2)}(\cos\theta_j, \cos\theta_{j+1}) \,, \tag{A.5a}$$

$$f^{(2)}(\cos\theta_j, \cos\theta_{j+1}) = \sum_{m=0}^{\infty} \frac{2m+1}{2} g_m P_m(\cos\theta_j) P_m(\cos\theta_{j+1}) \,, \tag{A.5b}$$

where $\tilde{p}_s(\cos\theta_1)$ is the probability density function of the starting polar angle. For simplicity, we assume $\tilde{p}_s(\cos\theta_1) = 1/2$ (uniform distribution) instead of the actual anisotropic phase function, which was shown not to affect the final result in the diffusion regime.

Using the orthogonality of Legendre polynomials, now it is straightforward to obtain the following equations:

$$\begin{aligned} H_j(x_{j-1}, x_{j+1}) &= \int_{-1}^{1} f^{(2)}(x_{j-1}, x_j) T(x_j) f^{(2)}(x_j, x_{j+1}) dx_j \qquad \text{(A.6a)} \\ &= \sum_{m=0}^{\infty} \sum_{n=0}^{\infty} g_m^{1/2} g_n^{1/2} \sqrt{\frac{2m+1}{2}} \sqrt{\frac{2n+1}{2}} J_{m,n} P_m(x_{j-1}) P_n(x_{j+1}) \,, \\ \langle T(x_j) \rangle_{x_i} &= \int_{-1}^{1} ... \int_{-1}^{1} T(x_j) f^{(N)}(x_1, ..., x_N) dx_1 ... dx_N \qquad \text{(A.6b)} \\ &= \left(\hat{J} \right)_{0,0} \,, \\ \left\langle \prod_{m=k}^{j} T(x_m) \right\rangle_{x_i} &= \int_{-1}^{1} ... \int_{-1}^{1} \left(\prod_{m=k}^{j} T(x_m) \right) f^N(x_1, ..., x_N) dx_1 ... dx_N \qquad \text{(A.6c)} \\ &= \sum_{i(1)=0}^{\infty} ... \sum_{i(j-k)=0}^{\infty} J_{0,\, i(1)} J_{i(1),\, i(2)} ... J_{i(j-k),\, 0} \\ &= \left(\hat{J}^{j-k+1} \right)_{0,0} \,, \end{aligned}$$

where $\hat{J}$ is the matrix defined by

$$J_{m,n} = g_m^{1/2} g_n^{1/2} \sqrt{\frac{2m+1}{2}} \sqrt{\frac{2n+1}{2}} \int_{-1}^{1} T(x) P_m(x) P_n(x) dx \ , \tag{A.7}$$

and the $(\hat{J})_{0,0}$ represents the $(0,0)$ element of the matrix $\hat{J}$.

Thus, the average of the right side of Eq. (A.1a) over all the polar angles becomes

$$\left\langle \sum_{j=1}^{N} \Delta\phi_{n,j}^2(t,\tau) \right\rangle_{t,\, l_j,\, x_i} = N \frac{(k_a l)^2}{8} (4 n_0 k_0 A \eta)^2 \sin^2\left(\frac{1}{2}\omega_a \tau\right) \left[(\hat{J})_{0,0} + (\hat{J}^*)_{0,0} \right] . \tag{A.8}$$

On the other hand, the average of the right side of Eq. (A.1b) has a more complicated form:

$$\begin{aligned} \left\langle 2 \sum_{j=2}^{N} \sum_{k=1}^{j-1} \Delta\phi_{n,j} \Delta\phi_{n,k} \right\rangle_{t,\, l_j,\, x_i} &= \frac{1}{8} (k_a l)^2 (4 n_0 k_0 A \eta)^2 \sin^2\left(\frac{1}{2}\omega_a \tau\right) \\ &\quad \times \sum_{j=2}^{N} \sum_{k=1}^{j-1} \left[(\hat{J}^{j-k+1})_{0,0} + (\hat{J}^{*j-k+1})_{0,0} \right] . \end{aligned} \tag{A.9}$$

If we replace the sums on the right-hand side of Eq. (A.9) with

$$\sum_{j=2}^{N} \sum_{k=1}^{j-1} (\hat{J}^{j-k+1})_{0,0} = \left\{ \hat{J}^2 (\hat{I} - \hat{J})^{-1} \left[(N-1)\hat{I} - \hat{J}(\hat{I} - \hat{J}^{N-1})(\hat{I} - \hat{J})^{-1} \right] \right\}_{0,0} , \tag{A.10}$$

and further keep only the terms that are proportional to a large number N in the above equation, we have

$$\begin{aligned} \left\langle 2 \sum_{j=2}^{N} \sum_{k=1}^{j-1} \Delta\phi_{n,j} \Delta\phi_{n,k} \right\rangle_{t,\, l_j,\, x_i} &\simeq N \frac{1}{8} (k_a l)^2 (4 n_0 k_0 A \eta)^2 \sin^2\left(\frac{1}{2}\omega_a \tau\right) \\ &\quad \times \left[\hat{J}^2 (\hat{I} - \hat{J})^{-1} + \hat{J}^{*2} (\hat{I} - \hat{J}^*)^{-1} \right]_{0,0} . \end{aligned} \tag{A.11}$$

Joining Eqs. (A.8) and (A.11), we finally have

$$\left\langle \sum_{j=1}^{N} \Delta\phi_{n,j}^2(t,\tau) + 2\sum_{j=2}^{N}\sum_{k=1}^{j-1} \Delta\phi_{n,j}\Delta\phi_{n,k} \right\rangle_{t,\, l_j,\, x_i} \simeq N\frac{1}{4}(k_a l)^2 (4n_0 k_0 A\eta)^2 \sin^2\left(\frac{1}{2}\omega_a\tau\right) \times \mathrm{Re}\left[\hat{J}(\hat{I}-\hat{J})^{-1}\right]_{0,\,0} , \qquad \text{(A.12)}$$

where Re is for the *real value*.

The remaining task is to provide the average of the right-hand side of Eqs. (A.1c), (A.1d), and (A.1e), over all polar angles. As a first step, we define the coefficient $\Phi_{m,n}$ for any function $\Phi(x)$, and for each pair of nonnegative integer numbers (m,n):

$$\Phi_{m,n} = \int_{-1}^{1} \sqrt{\frac{2m+1}{2}}\sqrt{\frac{2n+1}{2}} g_m^{1/2} g_n^{1/2} \Phi(x) P_m(x) P_n(x) dx . \qquad \text{(A.13)}$$

Then, according to the definition in Eq. (A.13), it is easy to show that for the functions x, x^2, $T(x)$, and $xT(x)$ we have

$$\begin{aligned} (x)_{0,j} &= \delta_{1,j} g_1^{1/2}/3 , \qquad \text{(A.14)} \\ \left(x^2\right)_{0,0} &= 1/3 , \\ [xT(x)]_{0,j} &= (ik_a l)^{-1} \left(T_{0,j} - \delta_{0,j}\right) , \\ T_{j,\,1} &= (ik_a l)^{-1} \sqrt{3g_1} \left(T_{0,\,j} - \delta_{0,\,j}\right) , \end{aligned}$$

where $\delta_{a,b}$ represents the delta function.

Using the results in Eq. (A.14), the average over all the polar angles of the right-hand side of Eq. (A.1c) is

$$\left\langle \sum_{j=1}^{N-1} \Delta\phi_{d,j}^2(t,\tau) \right\rangle_{t,\, l_j,\, x_i} = (2n_0 k_0 A)^2 \sin^2\left(\frac{1}{2}\omega_a\tau\right) (N-1)\,\frac{1}{3}(1-g_1) . \qquad \text{(A.15)}$$

On the other hand, the average of the right-hand side of Eq. (A.1d) is

$$\left\langle 2\sum_{j=2}^{N-1}\sum_{k=1}^{j-1}\Delta\phi_{d,j}\Delta\phi_{d,k}\right\rangle_{t,\,l_j,\,x_i} = (2n_0k_0A)^2\sin^2\left(\frac{1}{2}\omega_a\tau\right)\frac{(1-g)^2}{(k_al)^2}\mathrm{Re}[\hat{M}]_{0,0}, \quad \text{(A.16)}$$

where $\hat{M}=\hat{J}^{N-2}-\hat{I}$. Since the right-hand side of Eq. (A.16) is not proportional to N, we consider it much smaller than the right-hand side of Eq. (A.15), and we have

$$\left\langle \sum_{j=1}^{N-1}\Delta\phi_{d,j}^2(t,\tau)+2\sum_{j=2}^{N-1}\sum_{k=1}^{j-1}\Delta\phi_{d,j}\Delta\phi_{d,k}\right\rangle_{t,\,l_j,\,x_i} \simeq N(2n_0k_0A)^2\sin^2\left(\frac{1}{2}\omega_a\tau\right)\frac{1-g_1}{3}. \quad \text{(A.17)}$$

In general, the errors of approximation we made in Eqs. (A.12) and (A.17) are small when both k_al and the average N are large. Conversely, the error can be large: for example, if $N=10$, and $k_al=1$, the error is about 50% for isotropic scattering.

Finally, the average over all the polar angles of the right-hand side of Eq. (A.1e) is

$$\left\langle 2\sum_{j=1}^{N}\sum_{k=1}^{N-1}\Delta\phi_{n,j}\Delta\phi_{d,k}\right\rangle_{t,\,l_j,\,x_i} = i(N-1)\frac{1-g_1}{k_al}\left[(\hat{J}^2)_{0,0}-(\hat{J}^{*2})_{0,0}\right], \quad \text{(A.18)}$$

and it is equal to zero because the elements of the symmetric matrix $\hat{J}$ are either real or imaginary numbers.

The expression for the function $F(\tau)$ [Eq. (3.4)] becomes

$$\begin{aligned} F(\tau) \;\simeq\; \Bigg\langle & N\frac{1}{4}(k_al)^2(4n_0k_0A\eta)^2\sin^2\left(\frac{1}{2}\omega_a\tau\right)\mathrm{Re}\left[\hat{J}(\hat{I}-\hat{J})^{-1}\right]_{0,0} \\ & +N\frac{1}{2}(2n_0k_0A)^2\sin^2\left(\frac{1}{2}\omega_a\tau\right)\frac{2}{3}(1-g_1)\Bigg\rangle_N , \end{aligned} \quad \text{(A.19)}$$

where the last average is over all realizations of the number of free paths N in a photon path of length s. Since the average value of N is s/l, we have

$$F(\tau)\simeq\frac{s}{l}(2n_0k_0A)^2\sin^2\left(\frac{1}{2}\omega_a\tau\right)\left\{\eta^2(k_al)^2\,\mathrm{Re}\left[\hat{J}(\hat{I}-\hat{J})^{-1}\right]_{0,0}+\frac{1-g_1}{3}\right\}. \quad \text{(A.20)}$$

APPENDIX B

DERIVATION OF THE MEAN GREEN'S FUNCTION

To solve the Dyson Equation [Eq. (5.6)], we first assume that the mean Green's function $G_s(\mathbf{r}_b, \mathbf{r}_a, t)$ from $\mathbf{r}_a$ to $\mathbf{r}_b$ can be represented as

$$G_s(\mathbf{r}_b, \mathbf{r}_a, t) = G_a(\mathbf{r}_b, \mathbf{r}_a, t)\chi(\mathbf{r}_b, \mathbf{r}_a, t). \tag{B.1}$$

By substituting Eq. (B.1) into Eq. (5.6), we obtain

$$\begin{aligned} G_a(\mathbf{r}_b, \mathbf{r}_a, t)\chi(\mathbf{r}_b, \mathbf{r}_a, t) &= G_a(\mathbf{r}_b, \mathbf{r}_a, t) \\ &\quad - \int \frac{f(\hat{\mathbf{\Omega}}_{sb}, \hat{\mathbf{\Omega}}_{as})\chi(\mathbf{r}_b, \mathbf{r}_s, t)}{4\pi|\mathbf{r}_b - \mathbf{r}_s||\mathbf{r}_s - \mathbf{r}_a|} \exp[ik_0 n_0 F(\mathbf{r}_s)]\rho_s d\mathbf{r}_s, \end{aligned} \tag{B.2}$$

where

$$F(\mathbf{r}_s) = |\mathbf{r}_a - \mathbf{r}_s|[1 + \xi(\mathbf{r}_s, \mathbf{r}_a, t)] + |\mathbf{r}_s - \mathbf{r}_b|[1 + \xi(\mathbf{r}_b, \mathbf{r}_s, t)] + \mathbf{e}_s(t)\cdot(\hat{\mathbf{\Omega}}_{as} - \hat{\mathbf{\Omega}}_{sb}). \tag{B.3}$$

Without loss of generality, we assume that the ultrasound propagates along the Z axis. In order to simplify the appearance of further expressions, the following notation will be used: the distance between two points at $\mathbf{r}_a$ with coordinates $\{x_a, y_a, z_a\}$ and $\mathbf{r}_b$ with coordinates $\{x_b, y_b, z_b\}$ will be written as r_{ab}, where $r_{ab} \equiv |\mathbf{r}_a - \mathbf{r}_b|$; we will denote with $\{x_{ab}, y_{ab}, z_{ab}\}$ coordinates of the vector difference $\mathbf{r}_a - \mathbf{r}_b$; the terms $\xi(\mathbf{r}_a, \mathbf{r}_b, t)$ and $\chi(\mathbf{r}_b, \mathbf{r}_a, t)$ will be written as ξ_{ab} and χ_{ba} respectively; partial derivatives will be written using the appropriate subscripts (for example $F_x(\mathbf{r}_s) \equiv \partial F(\mathbf{r}_s)/\partial x_s$, $F_{xy}(\mathbf{r}_s) \equiv \partial^2 F(\mathbf{r}_s)/\partial x_s \partial y_s$).

We first resolve the following integral

$$I_{xy} = -\iint \frac{f(\hat{\mathbf{\Omega}}_{sb}, \hat{\mathbf{\Omega}}_{as})\chi_{bs}}{4\pi r_{as} r_{sb}} \exp[ik_0 n_0 F(\mathbf{r}_s)]\rho_s dx_s dy_s \tag{B.4}$$

in the $X-Y$ plane from Eq. (B.2). The term $k_0 n_0 F(\mathbf{r}_s)$ in Eq. (B.4) changes much faster than the slow varying part $\rho_s f(\hat{\mathbf{\Omega}}_{sb}, \hat{\mathbf{\Omega}}_{as})\chi_{bs}/(4\pi r_{as} r_{sb})$, so we obtain the approximate value of I_{xy} by using the method of stationary phase. The integral in n-dimensional space ($x \in R^n$) of the form

$$I(\lambda) = \int_D g(x) \exp[i\lambda f(x)] dx, \tag{B.5}$$

where the phase $\lambda f(x)$ oscillates much faster than function $g(x)$ can be approximated as

$$I(\lambda) \approx \frac{g(x_0)}{\sqrt{|D(A)|}} \exp\left(i\lambda f(x_0) + i\pi\frac{\sigma}{4}\right)\left(\frac{2\pi}{\lambda}\right)^{n/2}. \tag{B.6}$$

In Eq. (B.6), x_0 is the single minimum of $f(x)$; A is the Hessian of $f(x)$ given by $A = [\partial^2 f(x)/\partial x_i \partial x_j|_{x=x_0}]$; σ is the signature of A calculated as the difference between the number of positive and negative eigenvalues of A; and condition $D(A) \neq 0$ is satisfied where $D(A)$ is the determinant of A. If there is more than one minimum of $f(x)$, then summation over all minima should be performed.

The functions ξ_{as} and ξ_{sb}, as well as the term $\mathbf{e}_s(t)\cdot(\hat{\mathbf{\Omega}}_{as} - \hat{\mathbf{\Omega}}_{sb})$, are independent from x_s and y_s, and the partial derivatives of $F(\mathbf{r}_s)$ can be calculated as

$$\begin{aligned} F_x(\mathbf{r}_s) &= x_{sa}(1+\xi_{as})/r_{as} + x_{sb}(1+\xi_{sb})/r_{sb}, \\ F_y(\mathbf{r}_s) &= y_{sa}(1+\xi_{as})/r_{as} + y_{sb}(1+\xi_{sb})/r_{sb}. \end{aligned} \tag{B.7}$$

The extrema of $F(\mathbf{r}_s)$ are given by $F_x(\mathbf{r}_s) = 0$ and $F_y(\mathbf{r}_s) = 0$, so we obtain the following relations

$$\begin{aligned} x_{sa}/x_{sb} &= -r_{as}(1+\xi_{sb})/[r_{sb}(1+\xi_{as})], \\ y_{sa}/y_{sb} &= -r_{as}(1+\xi_{sb})/[r_{sb}(1+\xi_{as})]. \end{aligned} \tag{B.8}$$

Since we consider only small ultrasound-induced optical phase perturbations ($|\xi_{sb}| <$

1, $|\xi_{as}| < 1$), from Eq. (B.8) we have $x_{sa}/x_{sb} \leq 0$ and $y_{sa}/y_{sb} \leq 0$.

The second partial derivatives of $F(\mathbf{r}_s)$ are

$$\begin{aligned} F_{xx}(\mathbf{r}_s) &= \frac{(y_{as}^2+z_{as}^2)(1+\xi_{as})}{r_{as}^3}+\frac{(y_{sb}^2+z_{sb}^2)(1+\xi_{sb})}{r_{sb}^3}, \\ F_{yy}(\mathbf{r}_s) &= \frac{(x_{as}^2+z_{as}^2)(1+\xi_{as})}{r_{as}^3}+\frac{(x_{sb}^2+z_{sb}^2)(1+\xi_{sb})}{r_{sb}^3}, \\ F_{xy}(\mathbf{r}_s) &= -\frac{x_{sa}y_{sa}(1+\xi_{as})}{r_{as}^3}-\frac{x_{sb}y_{sb}(1+\xi_{sb})}{r_{sb}^3}, \end{aligned} \tag{B.9}$$

and we can calculate $D(A)$ with the help of Eq. (B.8) as

$$\begin{aligned} D(A) &= z_{as}^2(1+\xi_{as})^2/r_{as}^4 + z_{sb}^2(1+\xi_{sb})^2/r_{sb}^4 \\ &\quad +(1+\xi_{as})(1+\xi_{sb})(z_{sb}^2 r_{as}^2 + z_{as}^2 r_{sb}^2)/(r_{as}r_{sb})^3. \end{aligned} \tag{B.10}$$

Based on Eqs. (B.9) and (B.10), A is positive definite ($D(A) > 0$ and also $F_{xx}(\mathbf{r}_s) + F_{yy}(\mathbf{r}_s) > 0$) and $\sigma = 2$. For any given z_s, we denote with $\{x_s, y_s, z_s\}$ the coordinates of a single minimum point $\mathbf{r}_s$ of $F(\mathbf{r})$. We now apply the approximation from Eq. (B.6) to the integral in Eq. (B.4) and obtain

$$\begin{aligned} I_{xy} &= -\frac{i\rho_s}{2k_0 n_0}\frac{f(\hat{\mathbf{\Omega}}_{as}, \hat{\mathbf{\Omega}}_{sb})\chi_{bs}}{r_{as}r_{sb}\sqrt{D(A)}}\exp[\mathbf{e}_s(t)\cdot(\hat{\mathbf{\Omega}}_{as} - \hat{\mathbf{\Omega}}_{sb})] \\ &\quad \times \exp\{ik_0 n_0[r_{as}(1+\xi_{as}) + r_{sb}(1+\xi_{sb})]\}, \end{aligned} \tag{B.11}$$

where x_s and y_s are obtained by solving the Eq. (B.8). We consider ξ_{sb} and ξ_{as} to be small perturbations of $F(\mathbf{r}_s)$, and we assume that we make only a small error by using the solution of unperturbed $F(\mathbf{r}_s)$ for x_s and y_s. From Eq. (B.8) when $\xi_{sb} = 0$ and $\xi_{as} = 0$, we have $x_{sa}/x_{sb} = -r_{as}/r_{sb}$, $y_{sa}/y_{sb} = -r_{as}/r_{sb}$, and $z_{sa}/z_{sb} = -\gamma r_{as}/r_{sb}$, where $\gamma = 1$ if z_s belongs to the interval bounded by z_a and z_b, and $\gamma = -1$ for all

other values of z_s. We further obtain the relations

$$\begin{aligned} x_s &= \frac{x_a z_{sb} - x_b \gamma z_{sa}}{z_{sb} - \gamma z_{sa}}, \quad & y_s &= \frac{y_a z_{sb} - y_b \gamma z_{sa}}{z_{sb} - \gamma z_{sa}}, \\ x_{sa} &= \frac{\gamma x_{ab} z_{sa}}{z_{sb} - \gamma z_{sa}}, & y_{sa} &= \frac{\gamma y_{ab} z_{sa}}{z_{sb} - \gamma z_{sa}}, \\ x_{sb} &= \frac{x_{ab} z_{sb}}{z_{sb} - \gamma z_{sa}}, & y_{sb} &= \frac{y_{ab} z_{sb}}{z_{sb} - \gamma z_{sa}}, \\ r_{as} &= \frac{|z_{sa}|}{z_{asb}} r_{abs}, & r_{sb} &= \frac{|z_{sb}|}{z_{asb}} r_{abs}, \end{aligned} \tag{B.12}$$

where $z_{asb} = |z_{as}| + |z_{sb}|$, and $r_{asb} = \sqrt{x_{ab}^2 + y_{ab}^2 + z_{asb}^2}$.

By using the expressions from Eq. (B.12), we further obtain $r_{as} r_{sb} \sqrt{D(A)} \approx z_{asb}$, and also

$$\begin{aligned} \exp\{ik_0 n_0 [r_{as}(1+\xi_{as}) + r_{sb}(1+\xi_{sb})]\} \quad &\approx \\ &\exp\{ik_0 n_0 r_{abs}[1 + (|z_{sa}|\xi_{as} + |z_{sb}|\xi_{sb})/z_{asb}]\}. \end{aligned} \tag{B.13}$$

When z_s is inside the interval bounded by z_a and z_b, then $z_{asb} = |z_{ab}|$ and the expression in Eq. (B.13) is further simplified as

$$\exp\{ik_0 n_0 [r_{as}(1+\xi_{as}) + r_{sb}(1+\xi_{sb})]\} \approx \exp[ik_0 n_0 r_{ab}(1+\xi_{ab})]. \tag{B.14}$$

After the substitution of Eq. (B.11) with obtained approximations into Eq. (B.2) and subsequent division by $G_a(\mathbf{r}_b, \mathbf{r}_a, t)$, we have

$$\chi_{ba} = 1 + \frac{i2\pi\rho_s}{k_0 n_0} \int \frac{f(\hat{\mathbf{\Omega}}_{sb}, \hat{\mathbf{\Omega}}_{as}) \chi_{bs}}{(z_{asb}/r_{ab})} \exp\{ik_0 n_0 [V(z_s) + \mathbf{e}_s(t) \cdot (\hat{\mathbf{\Omega}}_{as} - \hat{\mathbf{\Omega}}_{sb})]\} dz_s, \tag{B.15}$$

where

$$V(z_s) = r_{abs}\left(1 + \frac{|z_{as}|}{z_{asb}}\xi_{as} + \frac{|z_{sb}|}{z_{asb}}\xi_{sb}\right) - r_{ab}(1+\xi_{ab}). \tag{B.16}$$

Without loss of generality, we assume at this point that $z_b > z_a$. Since the rapidly

oscillating term in the exponent on the right-hand side of Eq. (B.15) is exactly zero only when $z_s \in (z_a, z_b)$, we assume that the value of the integral for $z_s \notin (z_a, z_b)$ is negligible. When x_s and y_s satisfy the relations in Eqs. (B.12), and $z_s \in (z_a, z_b)$, the vectors $\mathbf{r}_b - \mathbf{r}_s$ and $\mathbf{r}_s - \mathbf{r}_a$ are collinear. Consequently, $f(\hat{\mathbf{\Omega}}_{sb}, \hat{\mathbf{\Omega}}_{as}) = f(\hat{\mathbf{\Omega}}, \hat{\mathbf{\Omega}})$, $\hat{\mathbf{\Omega}}_{as} - \hat{\mathbf{\Omega}}_{sb} = 0$, and Eq. (B.15) is

$$\chi_{ba} = 1 + \frac{i2\pi\rho_s f(\hat{\mathbf{\Omega}}, \hat{\mathbf{\Omega}})}{k_0 n_0 (\hat{\mathbf{\Omega}}_{ab} \cdot \hat{\mathbf{\Omega}}_a)} \int_{z_a}^{z_b} \chi_{bs} dz_s, \tag{B.17}$$

with solution

$$\chi_{ba} = \exp\left(i2\pi\rho_s \frac{f(\hat{\mathbf{\Omega}}, \hat{\mathbf{\Omega}}) r_{ab}}{k_0 n_0} \right). \tag{B.18}$$

By substituting Eq. (B.18) into Eq. (B.1), the mean Green's function is

$$G_s(\mathbf{r}_b, \mathbf{r}_a, t) = \frac{\exp[iK(\mathbf{r}_b, \mathbf{r}_a, t)|\mathbf{r}_b - \mathbf{r}_a|]}{-4\pi|\mathbf{r}_b - \mathbf{r}_a|}, \tag{B.19}$$

where $K(\mathbf{r}_b, \mathbf{r}_a, t)$ is equal to $k_0 n_0 [1 + \xi(\mathbf{r}_b, \mathbf{r}_a, t)] + 2\pi\rho_s f(\hat{\mathbf{\Omega}}, \hat{\mathbf{\Omega}})/(k_0 n_0)$.

VITA

Name: Sava Sakadžić

Address: Department of Biomedical Engineering, Texas A&M University,
College Station, TX 77843 – 3120

Email address: sava@tamu.edu

Education: 1997-B.S. University of Belgrade, Yugoslavia,
Major: Electrical Engineering

2000-M.S. University of Belgrade, Yugoslavia,
Major: Electrical Engineering

2006-Ph.D. Texas A&M University, USA
Major: Biomedical Engineering